HAL
open science

Evaporation in porous media : pore network simulations and continuum modelling

Marouane Talbi

To cite this version:

Marouane Talbi. Evaporation in porous media : pore network simulations and continuum modelling. Reactive fluid environment. Institut National Polytechnique de Toulouse - INPT, 2021. English. NNT : 2021INPT0065 . tel-04171170

HAL Id: tel-04171170

https://theses.hal.science/tel-04171170v1

Submitted on 26 Jul 2023

HAL is a multi-disciplinary open access archive for the deposit and dissemination of scientific research documents, whether they are published or not. The documents may come from teaching and research institutions in France or abroad, or from public or private research centers.

L'archive ouverte pluridisciplinaire **HAL**, est destinée au dépôt et à la diffusion de documents scientifiques de niveau recherche, publiés ou non, émanant des établissements d'enseignement et de recherche français ou étrangers, des laboratoires publics ou privés.

THÈSE

En vue de l'obtention du

DOCTORAT DE L'UNIVERSITÉ DE TOULOUSE

Délivré par :

Institut National Polytechnique de Toulouse (Toulouse INP)

Discipline ou spécialité :

Dynamique des fluides

Présentée et soutenue par :

M. MAROUANE TALBI

le lundi 21 juin 2021

Titre :

Evaporation dans les milieux poreux : simulations sur les réseaux de pores et approche continue

---

Ecole doctorale :

Mécanique, Energétique, Génie civil, Procédés (MEGeP)

Unité de recherche :

Institut de Mécanique des Fluides de Toulouse (IMFT)

Directeur de Thèse :

M. MARC PRAT

Rapporteurs :

M. JEROME VICENTE, AIX-MARSEILLE UNIVERSITE
MME AZITA AHMADI-SENICHAULT, UNIVERSITE DE BORDEAUX

Membres du jury :

M. LOUNÈS TADRIST, AIX-MARSEILLE UNIVERSITE, Président
M. MANUEL MARCOUX, TOULOUSE INP, Membre
M. MARC PRAT, TOULOUSE INP, Membre

Contents

1 Introduction **6**

2 State of the art. Drying Pore network model **10**
2.1 State of art(adapted from ANR/DFG project proposal "DRYCAP") 10
2.2 Drying Pore network model 18
2.3 Computing performance 24
2.4 Macroscopic parameters 25
2.5 Conclusions 27

3 About Schlünder's model: A numerical study of evaporation from partially wet surfaces **34**
3.1 Introduction 34
3.2 Method 37
3.3 Influence of pore shape 38
3.4 A counter – example 40
3.5 Evaporation rate for very low wetted surface fractions 41
3.6 Influence of disorder 43
3.7 Extension of Schlünder formula to heterogeneous surfaces . . . 46
3.8 External mass transfer and PNM 50
3.9 Summary and discussion 52

4 Coupling between internal and external mass transfer during stage 1 evaporation in capillary porous media: interfacial resistance approach **58**
4.1 Introduction 58
4.2 Pore network drying model 61
4.3 Comparison between experimental and PNM results 63
4.4 Saturation profiles 64
4.5 Drying kinetics 70

4.6 NLE effect. Tranfer in the top edge effect region 73
4.7 On the transfer coupling at the porous medium surface 75
4.8 Capillary regime continuum model solution 82
4.9 Discussion 92
4.10 Conclusions 94

5 Percolating and non-percolating liquid phase continuum model of drying in capillary porous media. Application to solute transport in the very low Peclet number limit 100
5.1 Introduction 100
5.2 Continuum models 102
5.2.1 NLE two equation continuum model 102
5.2.2 Three equation continuum model 103
5.3 Pore network model 105
5.4 Pore network simulations 107
5.5 Continuum model solution 113
5.6 Solute concentration evolution in the hyperdiffusive limit . . . 115
5.6.1 PNM computations 116
5.6.2 Continuum approaches 119
5.7 Discussions 121
5.8 Conclusions 125

6 General Conclusion 131

Acknowledgments

I would like to thank mainly my thesis director Mr Marc Prat, CNRS Research Director, for the follow-up during my work, for his advice and especially for all his efforts and his patience.
I would also like to thank all the members of the "milieu poreux" research group within the imft with whom I spent some pleasant moments, and who cheered me up in difficult times.
I dedicate this thesis to my parents Malika and Abdellatif and to my little sisters Rim and Marwa.

baba mama, awalane bgite ngolikoum balli ana tanbgikoum bazzaf, ou matkadroch tssawrou chhal, awal nasse fakarte fihoum kbal man siffate hade rapport houma ntouma, ana daba tan ktabe likoum baal arbiya bache mayfhamna hta wahade, hade thèse tamrrate sinine taa33 tadhiya, tamrate sinine ta33 flousse takhssarate ala wadde kraya, baba bgiite nchoukrak ala ga33 liyame li dawaztha maak bache tachrah liya dourousse, ala ga33 liyam illi kanti kante mna333ni man dkolche l la salle l msslahti, ala ga33 liyam likana tane saliwe laaidde kbire kbal man lokhrine, ala ga33 la33ssa li kinti kate attini fache kante kan khabbi noukatte, ou surtout ala ga33 dak lmarde li darte like fal hikba ta33 al jabr, mama tanti tanbggi nchoukrak ala ga33 dbalajje illi kanti ba33ti bache nakrawe, alla ga33 liyam illi kanti katdini fiha lmadrassa, ana kan chkarkoum kamline, ana daba salite kraya, ou dazzate lhajja okhra, araf illi mazal kate hazzou liya lham, walakin danya hiya haddi, bggite nchkore rim tahiya hiya ou mimi ou ngoulihoum tanbgihoum tahouma, bgiite nachkore mima ou lala illi ti hassou bal fakhre balli andhoum doctore fal famila, bgiite nochkore awtani khalli lay hafdou karim ou bibiche ala pc li kante attatni, jditi tahiya illi salfatna flousse kbal manamchi l franca ou bal mounassaba floussha khdathoum simana li mbaade , ou bgiite nchkour tata fatima ou wladha ou ammi lahsan wakha rajawi, bal mounnasaba tata fatima andi liha htirame kbire, ou fal akhire tanchkore fatima sofi illi rbaatni ou hiya arfa chnou kine, tan chkore kolchi ou samhou liya illi nssite chi wahade, tahya famila talbi famila moussamih ou mousti.

Abstract

Drying of porous media is at the heart of many environmental and industrial processes. In this thesis, we are interested in capillary porous media, a category typically corresponding to pore sizes in the micron range. Modeling of drying is traditionally carried out within the classical framework of the continuum approach to porous media. Although widely used, the corresponding models cannot be considered as fully predictive so that the theory of drying porous media in the continuous framework can be still considered as incomplete. A well-identified difficulty of the continuum approach is the coupling with external transfers. In this thesis, this point is studied from comparisons with simulations on a pore network model by focusing on the regime dominated by capillary effects and the first period of drying during which the surface of the porous medium is partially wetted. This coupling is studied based on the concepts of interfacial resistance and effective surface. The interfacial resistance is characterized in detail from the pore network simulations. In a second part, we focus on another major characteristic of drying: the fact that the liquid phase breaks up into numerous clusters. This leads to the development of a continuum three-equation model in which the liquid phase is decomposed into a percolating liquid phase and a non-percolating liquid phase. Very good agreement between this model and the pore network simulations is obtained. Finally, this three-equation model is extended to the case where a solute is present in the liquid phase. This leads to a continuum model with five equations. Here again, a very good agreement is obtained between the continuum modeling and simulations on a pore network.

Résumé

Le séchage des milieux poreux est au cœur de nombreux processus environnementaux et procédés industriels. Dans cette thèse, on s'intéresse aux milieux poreux capillaires, catégorie correspondant typiquement à des tailles de pores dans la gamme micronique. La modélisation du séchage est traditionnellement effectuée dans le cadre classique de l'approche continue des milieux poreux. Bien que très utilisés, les modèles correspondant ne peuvent pas être considérés comme totalement prédictifs si bien que la théorie du séchage des milieux poreux dans la cadre continu est encore incomplète. Une difficulté bien identifiée de l'approche continue est le couplage avec les transferts externes. Dans cette thèse, ce point est étudié à partir de comparaisons avec des simulations sur réseaux de pores en se focalisant sur le régime dominé par les effets capillaires et la première période du séchage durant laquelle la surface du milieu poreux est partiellement mouillée. Ce couplage est étudié à partir des concepts de résistance interfaciale et de surface effective. La résistance interfaciale est caractérisée de façon détaillée à partir des simulations sur réseau de pores. Dans une deuxième partie, on se concentre sur une autre caractéristique majeure du séchage : le fait que la phase liquide se fragmente en de nombreux amas. Ceci conduit au développement d'un modèle continu à trois équations dans lequel la phase liquide est décomposée en une phase liquide percolante et une phase liquide non-percolante. Un très bon accord entre ce modèle et les simulations sur réseau de pores est obtenu. Enfin ce modèle à trois équations est étendu au cas où un soluté est présent dans la phase liquide. Ceci conduit à un modèle continu à cinq équations. Ici encore, un très bon accord est obtenu entre modélisation continue et simulations sur réseau de pores.

Chapter 1

Introduction

In the natural environment, matter is mostly porous. Few solids are rigorously non-porous. Soils and many rocks are porous, and generally contain water that is rarely pure. A porous medium can be defined as a solid with sufficient open space where one or more fluids can flow. Historically drying has always been considered to be a chemical process and has attracted the attention of human since its existence. During the last century we can notice that a lot of researchers have brought renewed attention to this physical process. It should be remembered that drying is a key natural, but also an indutrial process, especially in porous media. Drying in porous media containing a multicomponent liquid occurs in many industrial fields for example in pharmaceutical production, in soil remediation [Ho and Udell, 1995], in oil recovry, and also in food stuffs and others. In fact we are particulary interested here in two-phase drying problems, where there are only immiscible fluid phases present in the medium. The water will be considered as the wetting phase and the gas (water vapor in air) is considered as the non-wetting phase. Drying phenomena usually involves simultaneous heat and mass transfers. Industrialists have shown that relying solely on experiments while neglecting mathematical models can reduce the quality of the dried product, raising its production cost, and consequently the efficiency of the drying process. Two-phase flows can be studied at different scales and using different techniques. We can recall the direct methods, which consist in solving the Navier-Stokes equations, or approaches of the Lattice Boltzman type. However these techniques are rather expensive in computation time, and remain little used until now. Actually, drying has been approached by two different ways, either by continuum models or by discrete models. In the applications, the continuum approach is by far the most used. The latter is based on a representation of the porous medium as a fictitious continuum [Bear and Bachmat, 2012]. Indeed, despite the fact that numerical computa-

tional tools are progressing, classical continuum theories are still used since solving a continuum model is always faster than discrete large and complex models. The continuum models imply determining effective parameters, over a REV (representative elementary volume). However, truly predicting drying with continuum models is still a challenge. Although discrete approaches cannot be really used in engineering applications, they can be used in order to try to improve the continuum models. This is the main objective of the present thesis. In our case the discrete approach will be based on the pore network model (PNM) technique [Prat, 2002]. The idea is then to partition the porous medium into a system of cavities separated from each other by narrower passages corresponding to the pore space constrictions. The network can then be either structured or not. In the case of a structured network the PNM is seen as a grid (2D square) or cubic (3D), the cavities play the role of pores while the constrictions will be later called throats. There are two intrinsic properties of the network which are respectively the porosity and also the sizes of the pores and throats. The representation of a porous medium as a lattice permits relatively simple computation of the drying process.

Motivation

Thus, in this thesis, the question will not be to put in competition (PNM) and continuum models, but rather to reconcile them, while being interested in the following problems:

-Evaporation from discrete surfaces. The contact surface between the PNM and the external gas is a discrete surface where evaporation takes place from the surface pore entrances only. This type of problem has been studied quite early [Suzuki and Maeda, 1968]. Later, Schlünder [Schlünder, 1988] proposed an analytical formula for parametrizing the evaporation rate from a discrete surface. However, the pore opening at the surface was uniform in Schlünder's work. In this thesis, we explore the more realistic case where the diameter of the surface pores varies over the surface.

- [Le Bray and Prat, 1999] noticed a sharp drop in the saturation profiles in the vicinity of the evaporative surface. In this thesis, this edge effect is studied in details as well as the associated problem of the coupling between the internal and external transfers.

-The commonly used continuum models are local equilibrium (LE) one-equation models due to the fact that they consist of an equation with only

one variable, the saturation or the capillary pressure, as discussed for example in [Attari Moghaddam et al., 2017]. However, PNM simulations [Attari Moghaddam et al., 2017] suggest that it is more consistent to consider non-local equilibrium (NLE) conditions between the vapor and the liquid at the scale of a REV. This leads to the consideration of a two equation NLE continuum model. Furthermore, PNM simulations lead to separate the liquid phase into the percolating liquid phase and the non-percolating liquid phase. In this thesis, we therefore develop NLE continuum models taking into account this feature. We obtain a three equation model taking into account the transfer of mass between the two liquid phases in addition to the mass transfer between the liquid and vapor. This model is extended to the case of the presence of a solute within the liquid phase, leading to a five equation continuum model.

Content outline

The chapters are organized as follows :

Chapter 2 presents a brief survey of literature and the PNM drying algorithm used in our simulations. It also presents the numerical performances of the computational code and information on how macroscopic parameters can be determined from PNM simulations.

Chapter 3 focuses on the Schlünder formula. Numerical simulations are compared with this analytical formula. The influence of the pore shape as well as the impact of the pore size variability are studied. The limits of the formula are also presented and a modified form of Schlünder formula is presented by introducing the notion of influence surface so as to take into account the pore size variability.

Chapter 4 focuses on the edge effect in the so-called capillary regime. It proposes an in-depth study of the interfacial conditions to couple the external and internal transfers by introducing the interfacial resistance approach.

Chapter 5 presents a drying continuum three-equation model. A comparison with PNM numerical simulations and the continuum model is performed. The model is extended to the case where there is a solute present in the liquid phase. A special attention is devoted to the key role of the liquid fragmentation process occurring during drying on the solute dynamics.

Chapter 6 contains a general conclusion and opens up new perspectives.

References

[Attari Moghaddam et al., 2017] Attari Moghaddam, A., Prat, M., Tsotsas, E., and Kharaghani, A. (2017). Evaporation in capillary porous media at the perfect piston-like invasion limit: Evidence of nonlocal equilibrium effects. *Water Resources Research*, 53(12):10433–10449.

[Bear and Bachmat, 2012] Bear, J. and Bachmat, Y. (2012). *Introduction to modeling of transport phenomena in porous media*, volume 4. Springer Science & Business Media.

[Ho and Udell, 1995] Ho, C. K. and Udell, K. S. (1995). Mass transfer limited drying of porous media containing an immobile binary liquid mixture. *International journal of heat and mass transfer*, 38(2):339–350.

[Le Bray and Prat, 1999] Le Bray, Y. and Prat, M. (1999). Three-dimensional pore network simulation of drying in capillary porous media. *International journal of heat and mass transfer*, 42(22):4207–4224.

[Prat, 2002] Prat, M. (2002). Recent advances in pore-scale models for drying of porous media. *Chemical engineering journal*, 86(1-2):153–164.

[Schlünder, 1988] Schlünder, E.-U. (1988). On the mechanism of the constant drying rate period and its relevance to diffusion controlled catalytic gas phase reactions. *Chemical Engineering Science*, 43(10):2685–2688.

[Suzuki and Maeda, 1968] Suzuki, M. and Maeda, S. (1968). On the mechanism of drying of granular beds mass transfer from discontinuous source. *Journal of chemical engineering of Japan*, 1(1):26–31.

Chapter 2

State of the art. Drying Pore network model

2.1 State of art(adapted from ANR/DFG project proposal "DRYCAP")

Drying of porous media is a central process in many environmental and engineering applications. These include the evaporation of water from soils (associated with the hydrological water balance and climatic issues), the drying of foodstuffs and building materials, the recovery of volatile hydrocarbons from underground oil reservoirs or the remediation of polluted soils. Drying steps are common in many manufacturing processes, which make the drying of porous materials to an important unit operation in various industries. Due to the importance of the field, the drying of porous materials has motivated many studies and is a very active research area.
However, not only the importance of the field and the plethora of applications are responsible for the tremendous experimental effort invested in drying investigations and the overwhelming amount of resulting data published every year. The main aspect, which at the same time is the starting point for the present thesis, is that the existing theories of drying are not sufficiently predictive, not even for the simplest type of porous media, as the rigid capillary porous media. Rigid means that the solid matrix does not deform or fracture during the drying process. Capillary porous means that the maximum amount of water that the interior surface can fix by adsorption is negligible compared to the available pore space volume in the medium. This implies that the minimum pore size in this type of porous medium is greater than about 100 nm. The water in such a porous medium is thus spatially fixed by capillarity as a result of direct contact between liquid water and the medium.

Capillary porous media are an important class of porous media, which are encountered in numerous engineering applications and natural situations. Porous stones (sandstones), sandy soils, building materials (fire bricks, tiles, plaster), fibrous materials (such as the ones used for insulation or in the gas diffusion layer of proton exchange membrane fuel cells), porous wicks of many devices (capillary evaporators, vaporisers for volatile perfume or insect repellent liquids in a room, etc.), various processed foods (especially those with instant properties), and many pharmaceutical dosage forms are examples of capillary porous media. An archetypical academic example is a random packing of particles of an average size larger than 1 μm (up to a few hundreds of μm). Rigid capillary porous media represent a class of porous materials which is also of paramount importance in the study of transport phenomena because of its relative simplicity. A view is that we must first be able to develop satisfactory theories for drying of this important class of porous media before hoping to develop satisfactory theories for more complex porous media involving nano-scale pores and/or mechanical deformations or fracturing, for example.

Drying theories traditionally result in continuum models, i.e. they are based on the assumption that drying porous media can be represented by a fictitious continuum, in which the underlying transport phenomena can be described (e.g., Bear and Bachmat [11]). The background of this approach is historical, because discrete representations presuppose the availability of high computational capacity for their implementation. Though such capacity became increasingly available, continuum models will not lose their importance, because solving a continuum model by discretisation will remain very much faster than the solution of a discrete model in the foreseeable future, especially for the large solution domains required in most applications.

In the first works on continuum drying models (e.g. Philip and De Vries [12], Luikov [13]), the coupled heat, mass and momentum transfer equations used to describe the drying process were obtained from purely phenomenological considerations. Later (e.g., Whitaker [14, 15]), these equations were derived more rigorously using up-scaling techniques, such as the volume averaging method (Whitaker [16]). The corresponding equations have been widely used to predict the evolution of the moisture, liquid pressure, gas pressure, and temperature fields. These equations are presented and discussed in many references, e.g., Whitaker [14], Plumb [17], Perré et al. [18], Geoffroy and Prat [19]. They involve classical concepts such as a generalised Darcy's law and the associated concepts of relative permeabilities and retention curve, as well as the concept of local capillary equilibrium (the liquid-gas distribution

at the scale of a representative elementary volume (REV) is controlled by capillarity only). The corresponding set of equations will be referred to as the classical continuum model (CCM).

While classical and extremely useful, and in spite of many studies, the CCM cannot be considered as a successful theory because it is not truly predictive. A major test situation of interest in this context is the slow drying of a capillary porous medium. This is typically the situation encountered when a porous sample containing water dries at room temperature under laboratory conditions. It typically leads to drying with a globally averaged speed of 0.1 to 1 cm of material dried per day. Under these circumstances, temperature variations can be ignored and the drying process is driven by mass transfer. Again, the view is that we must first develop predictive models for this simpler situation before considering the coupling with heat transfer (for this reason the thermal effect is neglected in this thesis).

As first presented by Krischer [20], the slow drying of capillary porous media is classically described in three main periods as follows. During the first period, referred to as the constant rate period (CRP), the evaporation rate is essentially constant and controlled by the external conditions (relative humidity and velocity in the surrounding air). The last period, the receding front period (RFP), is characterised by an internal evaporation front retreating into the porous medium, whereas the intermediate period, the falling rate period (FRP), is a crossover period characterised by a significant drop in the drying rate. Noting that the evaporation rate is not necessarily constant in the "constant" rate period, it is often preferred to classify the drying periods into two main periods stage 1 and stage 2. In this classification, stage 1 corresponds to the CRP whereas stage 2 encompasses the FRP and the RFP. Of paramount importance is the prediction of the duration of stage 1 since this is the period with the highest evaporation rate. The current situation is that the CCM basically fails to predict the stage 1/stage 2 transition. At best, the experimental drying curve (which is a plot of the evaporation rate as a function of the overall liquid saturation in the sample) can be reproduced using fitting parameters such as the mass transfer coefficient at the surface of the porous medium, e.g. Peishi and Pei [21]. The surface of the porous medium is the interface between the porous sample and the external air, whereby it is usually assumed for simplicity that the porous sample is in contact with the external air only on one of its sides, for instance the top side. However, reproducing experimental data by use of fitting parameters is not a prediction. As discussed below, limited predictive capacity is due to at least three fundamental reasons:

i) the assumption of local equilibrium regarding the partial water vapor pressure,

ii) poor modelling of the mass transfer at the interface between the porous medium surface and the bulk air,

iii) the impact of secondary capillary effects (liquid films, liquid bridges, etc.).

The fact that the mass transfer at the porous medium surface was a specific modelling issue has been recognized at least since the sixties with the pioneering work of Suzuki and Maeda [22]. Suzuki and Maeda essentially explained why a partially wet surface could lead to the same evaporation rate as a fully wet surface through compensation mechanisms (the flux from the wet patches is greater than the average flux and compensates the absence of evaporation from the dry solid areas of the surface). This problem was also considered by Schlünder [23] who proposed a simpler analytical model. This model incorporates the vapor transfer in the boundary layer of the gas phase. The thickness of this boundary layer is of major importance for the extent of stage 1. In the limit of a very thin boundary layer, lateral vapor transfer becomes negligible and the drying rate drops from the very beginning of the process. While this has been clearly helpful to better understand the "constant" drying rates during stage 1 for only partially wet porous medium surface, these works are by no means sufficient to solve the surface mass transfer issue in the context of drying continuum modelling, as discussed in more depth in the next chapter.
The fact that the CCM cannot be considered as a truly predictive theory and has major shortcomings is not a novelty. This observation has been actually in the core of the development of alternative approaches for now about twenty years. In particular, it has been a strong motivation for the alternative approach referred to as pore network modelling (PNM). The state of the art regarding drying PNM will be summarised in what follows. Drying PNM have been continuously improved since the first model (Prat [1]) and greatly contributed to a much better understanding of the drying process. The idea with the present thesis is to exploit the results and experiences accumulated over the years using PNM simulations as a guide to develop improved continuum models of drying.

PNM is based on a representation of the void space within a porous medium as a network of pores connected by narrower passages called throats. All relevant transport phenomena are modelled directly at the pore network level using basic physical laws. This is in contrast with continuum models, in which

the physics at the pore scale is more or less "hidden" into the macroscopic parameters. Review articles on drying PNM are available (Prat [2], Metzger et al. [24], Prat [25]), in addition to numerous specific articles (for example, [3, 4, 5, 26]). As schematically illustrated in Figure.2.1a, pore network drying models can be built using regular (or structured) lattices. Generally, this type of PNMs is computationally more efficient and can be quite sufficient to study fundamental issues. However, depending on the objective, structurally more refined PNMs can be developed so as to better represent a given microstructure (starting from binarised X-ray micro-tomography images, for example). They are referred to as unstructured PNMs (Figure.2.1b). For instance, the Voronoi algorithm [27] can be used to construct unstructured pore networks from a packing of spherical particles [6, 7, 28] or obtained from the X-ray images of real glass beads [8].

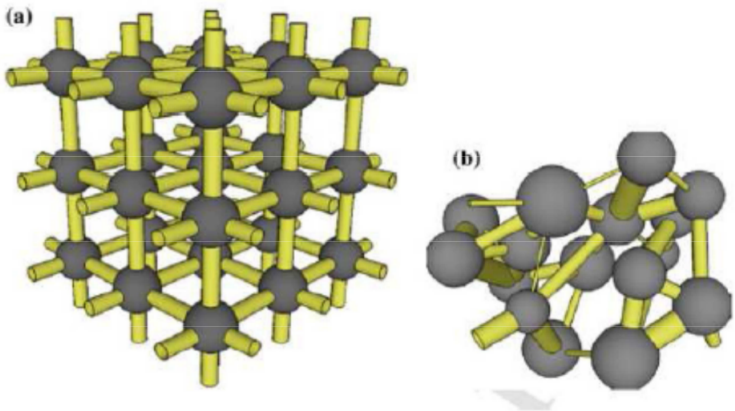

Figure 2.1: Schematic of (a) structured and (b) unstructured pore network. Spheres and cylinders correspond to pores and throats, respectively (Figure. from [19]).

Although PNMs can provide a much more accurate description of the drying process, it should be clear that they cannot be used directly in most applications because the maximum number of pores that can be typically considered with the available drying PNM codes does not exceed 100^3, which is several orders of magnitude smaller than the number of pores typically present in the porous domains considered in many applications. This is why, as already stressed, it is still indispensable to develop predictive continuum models.

Here we recall a few results obtained in previous works, which are of key importance for the present thesis:

1) PNM simulations clearly show the non-local-equilibrium (NLE) effect for vapor, i.e. $<P_v>/P_{vs} < 1$ for S > 0, where S is the local liquid saturation, $<P_v>$ is the spatially averaged local partial vapor pressure and P_{vs} is the saturation vapor pressure. This is illustrated in Figure.2.2. It is important to realize that the fact that $<P_v>/P_{vs} < 1$ for S greater than zero has nothing to do with adsorption phenomena or Kelvin's effect since these effects are not taken into account in the PNM simulations (on the ground that these effects are negligible in capillary porous media). This result is in complete contradiction with the CCM, which is based on the assumption of vapor local equilibrium (LE).

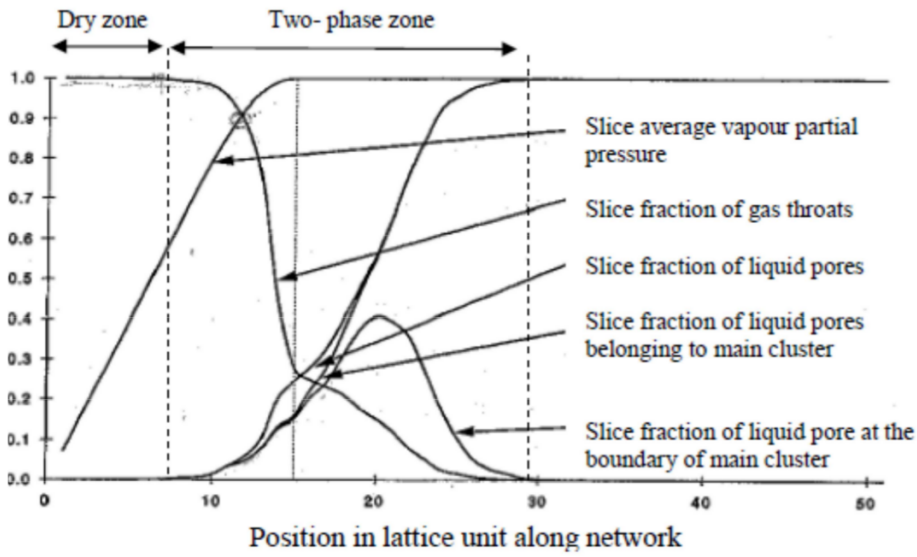

Figure 2.2: Evidence of vapor NLE from drying PN simulations in a 50 x 50 x 50 network. The two-phase zone length is about 20 lattice units in this example (Le Bray and Prat [3]). In this figure, slice fraction of liquid pores corresponds to S and slice average vapor partial pressure to $<P_v>/P_{vs}$

2)PNM simulations provide detailed information on the phase distribution at the porous medium surface. This is illustrated in Figure.2.3. Such information opens the possibility of detailed analysis of the mass transfer between the porous medium and the external air, a key issue in the modelling of the drying process. In contrast with the model by Schlünder [23] or the analysis by Suzuki and Maeda [22], where the surface is simply split into wet spots and dry spots (no evaporation flux), the contribution of empty pores at the

surface of the material (as the result of vapor transfer from menisci located deeper in the interior of the body) can be taken into account all along the drying process. It is also obvious that statistical and topological aspects associated with the evolution of surface clusters (dried or still wet) can be analysed by means of PNM.

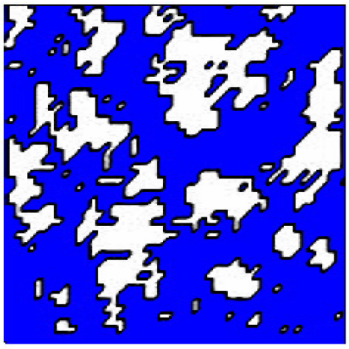

Figure 2.3: PNM computation of phase distribution (liquid phase in blue, gas phase in white) at the surface of drying porous medium (Le Bray and Prat [3]).

3) In general, liquid clusters can form during drying due to random distribution of throat sizes. The ability to describe the formation of liquid clusters is an important feature of PNM, but not explicitly considered in the CCM. Specifically, PNM simulations provide access to all details of the structure of the liquid phase in the body during drying, enabling to distinguish between isolated liquid clusters (which are not connected to each other or to the boundary of the two-phase region with liquid-filled throats) and the percolating liquid cluster (which spans the entire two-phase region of the drying material). On this basis, it is possible to distinguish between total saturation profiles, saturation profiles that refer to the main liquid cluster, and saturation profiles that refer to isolated liquid clusters. An example for this kind of distinction is illustrated in Figure.2.2, where percolating liquid is referred to as the main cluster. The distinction between percolating and non-percolating liquid opened the route for improved continuum modelling of two-phase flows in porous media, as shown by Hilfer [29] and several other authors in the context of problems of, for instance, immiscible displacement in tertiary oil recovery. Therefore, it will be an important aspect in the present thesis (chapter 5).

4)The existence of secondary capillary structures (SCS) in drainage is well known from the works of other groups, e.g. Scheel et al. [30], and can have

significant impact on drying. Secondary capillary structures, with an example of visualisation given in Figure.2.4, can have the form of corner liquid films or capillary ring chains. Corner liquid films appear in the margins of non-circular throats even after the core of such throats has been emptied by evaporation, increasing the hydraulic connectivity and accelerating the drying of porous materials. Such films have been studied experimentally and numerically (Chauvet al. [9]), and their effect has been taken into account in PNM (Yiotis et al. [31, 32], Prat [33]). This led to a quite good agreement between drying experiments with model porous media made using microfluidic techniques and PNM simulations (Prat [33]). The formation of capillary rings was visualized in random packings of particles using X-ray micro-tomography (Wang et al. [8, 34]) and in microfluidic model porous media by optical microscopy (Vorhauer et al. [10]). Structured PNMs that account for liquid rings were developed and respective simulation results were successfully compared with measurements [33, 10]. Liquid rings can accelerate the drying by establishing saturated air conditions in emptied throats even if they are not hydraulically interconnected. All these works clearly show that the impact of SCS must be considered as a specific topic in the modelling of capillary porous media drying. However, this important aspect will not be addressed in the present thesis, which therefore focusses on the simpler situation where the film development is negligible. This corresponds to situation where the liquid is not too wetting and/or corners are not present or do not form an interconnected systems in the pore space.

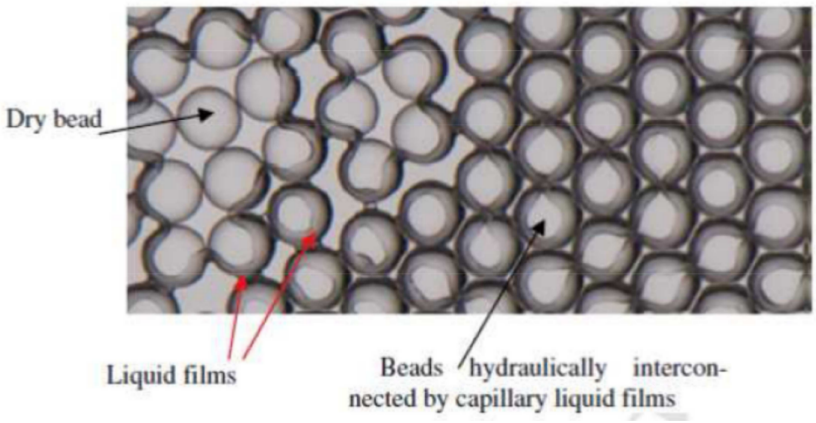

Figure 2.4: Secondary capillary structures forming during drying of a model porous medium made of glass beads. Liquid bridges are clearly visible (IMFT, unpublished).

5) Dissolved species (ions, solute molecules, colloidal particles) can be present in the liquid and deposited in the course of drying. Such deposition is important in many natural or technical processes (for example, salt deposition in soil, impregnation of catalyst carriers with active material), but it can also be visualised and exploited as a means for better understanding the drying process and for still better assessing the quality of a drying model. Salt deposition at the surface or within the material is exemplarily illustrated in Figure.2.5. Predicting correctly the distribution of salt crystallisation spots both at the evaporative surface of a porous medium and within the porous medium is, obviously, a strong test for PN models, since this implies a satisfactory modelling of both the internal and the surface transfer mechanisms. This aspect will be partially addressed in chapter 5 of the present thesis.

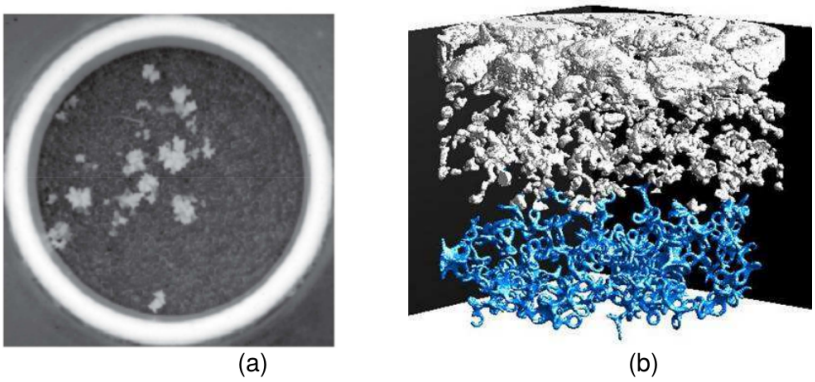

Figure 2.5: (a) Formation of discrete salt crystallisation spots at the evaporative surface of porous medium obtained by using optical camera (doc. IMFT). (b) Three-dimensional visualisation of liquid (in blue) and salt crystals (in grey) distribution in a packed bed of (here not visible) glass beads obtained by using X-ray micro-tomography (Wang et al. [34]).

2.2 Drying Pore network model

The drying PNM used in the present work is sketched in Figure. 2.6. It was introduced by Prat [1] as a modification of the percolation invasion algorithm (IP). As sketched in Figure.2.6, the PNM model is coupled to a boundary layer outside the PNM where a diffusion equation is solved.
This IP rules are used to model the capillary effects within the PNM. Other effects such as gravity or Kelvin effect or viscous effect can also be added, but in our case we will limit ourselves to the capillary regime.

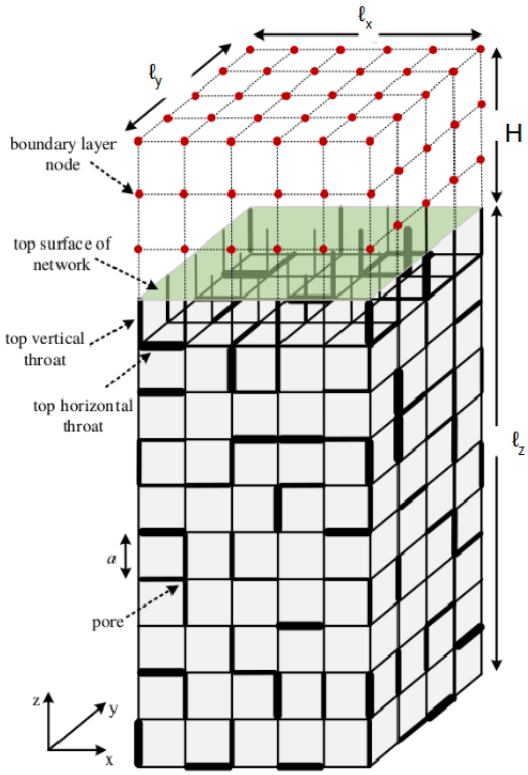

Figure 2.6: Three-dimensional representation of a pore network in addition to a boundary layer in the top. (figure taken from [43])

As in many previous work a structured network is used. Our network is composed of cubic pores, linked together by throats of square cross-section (Figure.2.7).
To each pore we assign a diameter d_p which varies between $[d_{p,min}\ d_{p,max}]$, and to each throat corresponds a diameter d_t which vary between $[d_{t,min}\ d_{t,max}]$. The distance between the center of two neighboring pores is noted a. The distribution of d_p and d_t is random and follows a uniform law of propability. In the drying simulation we will have to study the liquid vapor distribution in our porous medium.

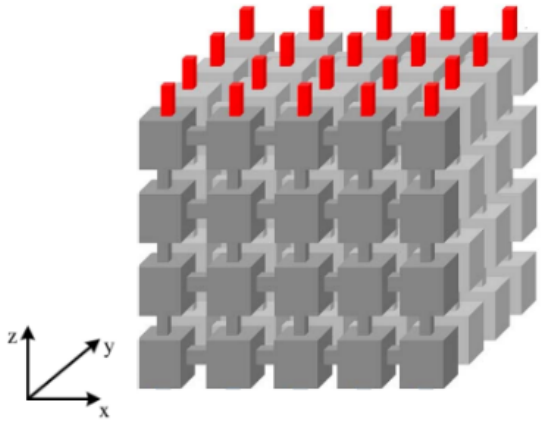

Figure 2.7: 3D structured pore network considered (figure taken from [44])

The pore space volume is distributed between pore and channels (throats), However it should be noted that the throats cannot be occupied by gas and liquid at the same time, unlike the pores. We then have four configurations of pores during the drying process:

- 1- Pore totally saturated with liquid noted "L", where all the bonds adjacent to this pore are liquid.
- 2- Pore partially invaded by gas "PE", where liquid-gas interface is located in the center of this pore, this kind of pore still contains liquid but is connect to a gas throat.
- 3- Pore completely invaded by gas "CE", but still adjacent to at least one liquid throat.
- 4- And finally gaseous pore "G", where all adjacent throats are gaseous.

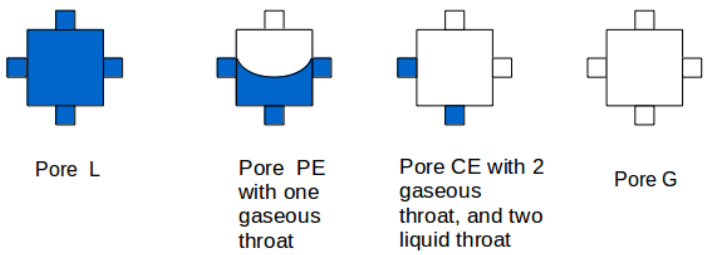

Figure 2.8: Different types of pore encountered during the simulation (figure adapted from [45])

The vapor partial pressure is known in the "L" and "PE" pore and is equal to the saturated vapor pressure $P_{v,sat}$. Unknown vapor pressures are those of the pores "CE" and "G". The mass transfer between two pores "i" and "j" is expressed by Fick's law:

$$J_{i,j} = \frac{D_v M_v}{RT} d_{t,ij}^2 (\frac{P_{vj} - P_{vi}}{l})$$

where D_v is the molecular diffusion coefficient of vapor, P_v the partial vapor pressure, M_v the water molecular weight, T the temperature, R the perfect gas constant. l is a distance. It can take two values "$d_p/2$" or "a" (lattice spacing), depending on the nature of the two pores and the position of the liquid gas interface.
- If pore i is of "G" type and its neighbour j are of "CE" or "G" type , the throat linking them is gaseous so l = a. If j are of "PE" type the throat is still gaseous so l = a, and the vapor partial pressure as said before in j are known and equal to $P_{v,sat}$.
- If pore i is of "CE" type and it's neighbour j are of "PE" type or "L" type we distinguish two cases, either the throat connecting them is gaseous, in this case l = a, or the throat connecting them is liquid and in this case l=$d_p/2$.
The computation nodes are located in the center of the pores. By applying the conservation of mass to each pore "CE" and "G" present in the PNM,

$$\sum_j J_{i,j} = 0 \quad \textbf{j represent the neighbor pores linked with pore i}$$

we obtain a linear system to solve. The open surface is the contact area between the boundary layer and the pore network model (green surface in

Figure.2.6), this surface will be the subject of a particular study in the next chapters. Interfacial computational nodes are added (Figure.2.9) at the contact zone because the computational nodes in the PNM are only located at the pore level. At those interfacial pores we assume that there is no lateral diffusion. When the throat below the interfacial pore is liquid the vapor pressure on the interfacial pore is known and is equal to $P_{v,sat}$.
Computational nodes are located in the boundary layer in order to better compute the evaporation rate from the PNM, and also to compute the vapor partial pressure. A classical finite volume method is used in boundary layer. The equation solved in the boundary layer is

$$\Delta P_v = 0.$$

Wall condition are imposed at the other surface of the PNM. At the top of the boundary layer, a dirichlet condition is imposed.

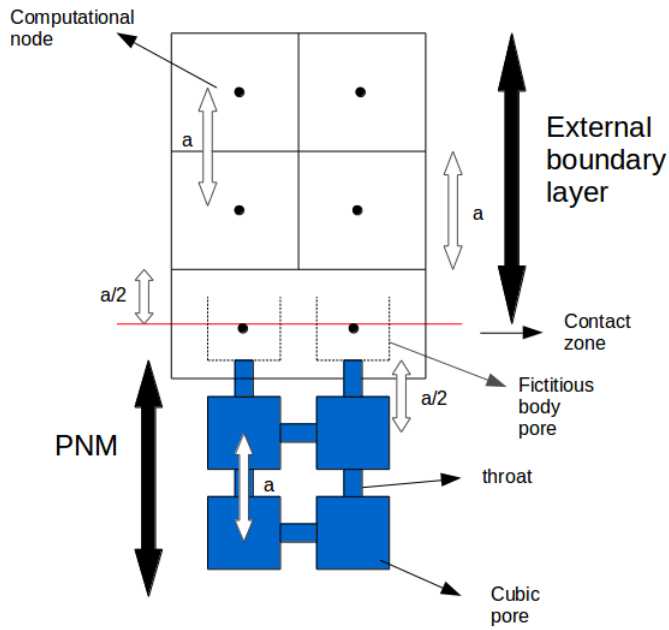

Figure 2.9: Configuration at the contact between the porous medium and the external boundary layer

The lattice spacing in the boundary layer is equal "a" and is the same as inside

the PNM, therefore we solve only one linear system; Here are the main steps of our drying algorithm in the capillary regime :

- (1) The first step is to identify each liquid cluster and give each one a label. A cluster is therefore a set of liquid pores and throats connected that share the same label. for more information see first deep search algorithm [46]

- (2) The second step is to locate all the gas-liquid interfaces in each of those clusters labelised. Those interfaces are at the boundary throats of the clusters. The capillary pressure is the difference of pressure between the gas and the liquid, and it's given by the Laplace formula

  $$p_{cap} = \frac{4\sigma cos(\theta)}{d_t}$$

  σ is the surface tension, and θ the contact angle. It's obvious from the Laplace equation that the throat which will be invaded correspond to the throat with the largest diameter.

- (3) The linear system is solved in order to know the partial vapor pressure field in the gaseous region.

- (4) At the level of each cluster, the evaporation rate is determined which is the sum of evaporation rate at the interfacial throat.

  $F_n = \sum_k J_k$; k runs over all the interfacial throats of the considered cluster.

  n is the cluster index (label)

- (5) The time required to fully invade the adjacent pore of the largest throat determined in step(2) is determined as follows:

  $$t_n^* = \frac{\rho_l V_{p,n}}{F_n}$$

  $V_{p,n}$ corresponds to the volume of the pore , and ρ_l is the liquid density.

- (6) Each cluster has now a candidate throat to be invaded, but also a corresponding time. The pore adjacent with $t_{min}^* = min(t_n^*)$ is fully invaded, while others are partially invaded according to the following formula:

  $$V_{p,n}(t + t_{min}^*) = V_{p,n}(t) - \frac{F_n.t_{min}^*}{\rho_l}$$

- (7) The previous steps are repeated until a desired network saturation is reached .

2.3 Computing performance

Numerical simulations were carried out at the Calmip research center, which is a regional computing center (region of Occitania) located in Toulouse. It includes "Olympe" supercomputer with a power of 1.365 Pflops/s peak. For more information see the following link: **"https://www.calmip.univ-toulouse.fr"**.
It is clear that according to the previous algorithm, steps(1) and (4) are the most demanding in terms of computation. Inded, as our porous medium , is totally saturated with liquid at the beginning of simulation, new clusters appear during the drying process. These new clusters are due to the fragmentation of the main cluster into smaller clusters. We can then distinguish the main or percolating cluster from the non percolating clusters. It should also be noted that, the more the pores of the PNM are invaded, the more the size of the linear system to be solved increases. Figure.(2.10) shows the variation in the number of cluster as a fonction of the saturation of network (porous domain) for different sizes of PNM.

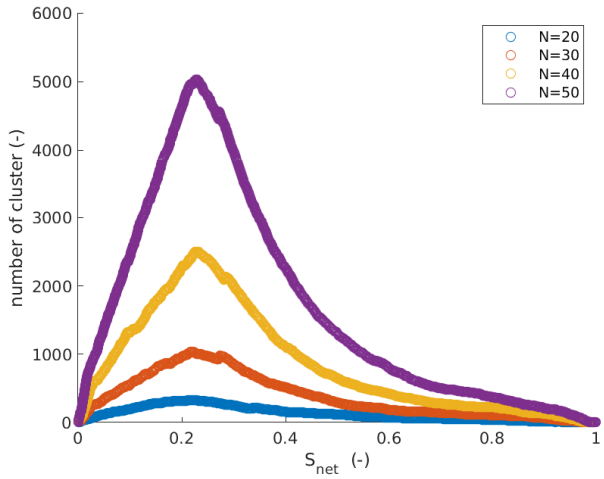

Figure 2.10: Variation of number of clusters with the saturation of the network, with H = 10a, for the four networks.

S_{net} represents the saturation of the porous medium and is given by :

$$S_{net} = \frac{\text{Volume of pores and throats occupied by the liquid}}{\text{Total volume of the pore space}}$$

N represents the number of pores in each direction. In the case of a cubic network $N = N_x = N_y = N_z$. The number of clusters varies exponentially

with N. This leads to a high computational time since step(1) in the drying algorithm is repeated after each saturation drainage.
In the next chapters, we will consider a PNM of size 30. This is explained by the fact several realizations are generated for a given network (Monte Carlo approach). It takes a mouth to simulate the complete drying of a PNM with 50 pores in each of the direction. At Calmip, we are limited to a number of hours allocated for the computation. The more processors we use , the faster is the consumption of our allocated number of hours. As shown in the speed up (Figure. 2.11) one can limit the computation to 20 procs.

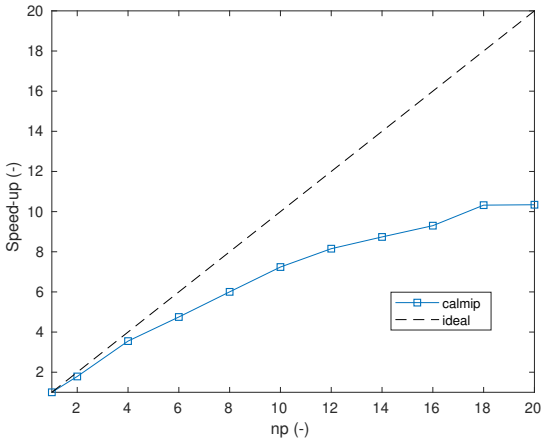

Figure 2.11: Variation of speed up (serial run time/parallel run time) determined from Calmip simulations with np (number of proc). The linear system with 100 000 unknowns is solved thanks to the petsc library.

2.4 Macroscopic parameters

The continuum models involve determining macroscopic parameters. These parameters can be determined from dedicated PNM simulations. This requires to identify a R.E.V. The parameters through which we will determine the REV for our network are :

- The effective diffusion coefficient given by ,

$$\frac{J}{A} = \epsilon.D_{eff}.\frac{M_v}{R.T}\frac{\Delta P_v}{L}.$$

  where "L" is the length of the PNM (L $=l_x$, or l_y or l_z, in our case L $= l_z$), and ΔP_v is the vapor pressure difference between ($L = 0$) and

$(L = l_z)$. A is the cross-section surface area of the network.

- The intrinsic permeability "k" of the medium given by the darcy formula neglecting gravity

$$q = \frac{k.\Delta P}{\mu.L}$$

where q is the flux discharge per unit area (m/s), L is the same as in the effective diffusion coefficient computation, and ΔP is the pressure difference between $(L = 0)$ and $(L = l_z)$, μ is the viscosity of the wetting phase (water).

- and the porosity ϵ

$$\epsilon = \frac{\text{volume of pores and throats of the PNM}}{\ell_x.\ell_y.\ell_z}$$

To calculate the effective diffusion coefficient we have considered a dry zone from the drying PNM simulation far from the liquid clusters. While to calculate the intrinsic permeability, we consider a pore network where the flow rate in the throats is given by Hagen-Poiseuille's law. (Figure 2.12) shows the variation of the three parameters according to N (size of porous medium). One can clearly show that a network of size 10^3 is reasonable for the R.E.V . Althought the computations of macroscopic parameters was originally developped in order to perform comparisons between PNM simulations, it turns out that a simpler approach, not requiring the use of the effective transport parameters has been eventually used in the next chapters.

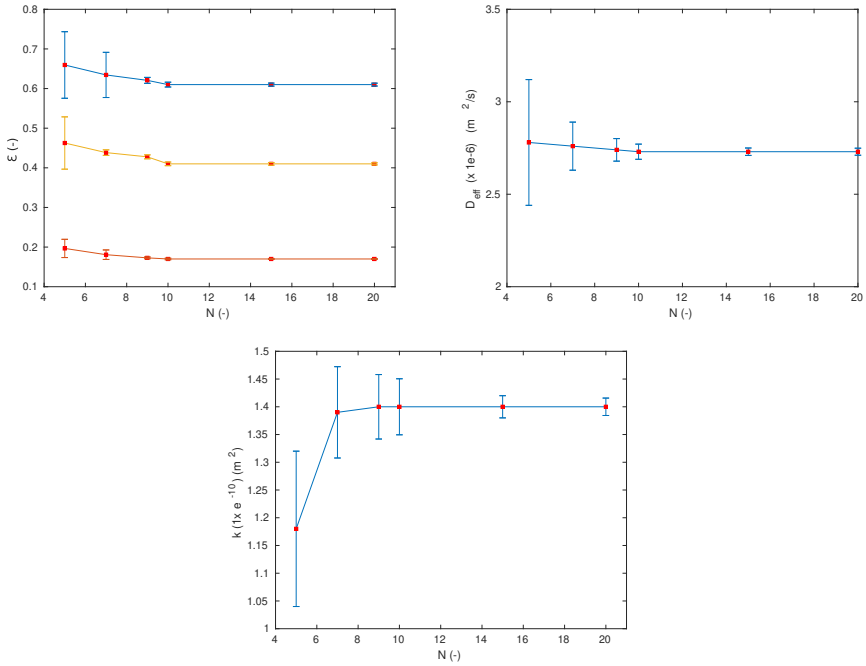

Figure 2.12: from left to right and from top to bottom, respectively, variation of porosity, effective diffusion coefficient, permeability as a function of N. For the porosity figure, these are three different distributions of pores and throats (blue graph: $d_p \in [0.775\ 0.825]$, $d_t \in [0.375\ 0.425]$; yellow graph $d_p \in [0.675\ 0.725]$, $d_t \in [0.275\ 0.325\ ]$; red graph $d_p \in [0.275\ 0.325]$, $d_t \in [0.175\ 0.225]$) , while D_{eff} and k curves are the results of the second configuration of throats and pores, (yellow graph in the porosity figure). For the simulations we took D_v= 1e-5 m^2/s, and μ= 1e-3 Pa.s

2.5 Conclusions

In summary, this overview of previous works indicates a series of major issues in the present state of the art of continuum modelling of drying of capillary porous media. These can be briefly listed as follows:

- There is a complete misunderstanding as regards the use of desorption isotherm in the context of drying capillary porous media. In many cases, the introduction of desorption isotherms has nothing to do with adsorption-desorption phenomena but actually is simply an erroneous

modelling of NLE effects (the average vapor partial pressure is less than the saturation pressure in a representative element volume (REV) when the liquid water saturation is sufficiently low in the REV). It is therefore crucial to fully recognize the possible NLE nature of the drying process in capillary porous media.

- The modelling of the mass transfer at the surface of the porous medium is a major issue still poorly understood (as discussed in the next chapter). This has led many authors to adjust ad-hoc modelling such as a mass transfer coefficient at the surface which is a function of surface saturation, or saturation dependent water vapor pressure at the surface. Actually, this has nothing to do with a predictive theory, resulting, again, from the fact that the NLE fundamental nature of the problem has been ignored so far. This point is addressed in Chapter 4 of the present thesis.

- When drying becomes very slow pore network simulations indicate that the liquid phase can be essentially formed by isolated liquid clusters. This is in strong contrast with the CCM, which does not make any distinction between the percolating liquid phase and the non-percolating clusters. This point is addressed in Chapter 5 of the present thesis.

- Dissolved species can also be transported during drying. This has a strong impact on the distribution of the considered species in the porous medium during drying. This aspect is addressed in Chapter 5.

These various points will be studied in the next chapters from comparisons between PNM simulations and continuum model solutions. The drying PNM has been presented in this chapter. It is based on the now somewhat classical algorithm presented in (Prat [1]).

References

[1] M. Prat, Percolation model of drying under isothermal conditions in porous media, International Journal of Multiphase Flow 19(4), 691-704, 1993.

[2] M. Prat, Recent advances in pore-scale models for drying of porous media, Chemical Engineering Journal 86, 153-164, 2002.

[3] Y. Le Bray, M. Prat, Three dimensional pore network simulation of drying in capillary porous media, International Journal of Heat and Mass Transfer 42,4207-4224,1999.

[4] T. Metzger, A. Irawan, E. Tsotsas, Influence of pore structure on drying kinetics: A pore network study, AIChE Journal 53, 3029-3041, 2007.

[5] N. Vorhauer, Q.T. Tran, T. Metzger, E. Tsotsas, M. Prat, Experimental investigation of drying in a model porous medium: Influence of thermal gradients, Drying Technology 31(8), 920-929, 2013.

[6] A. Kharaghani, T. Metzger, E. Tsotsas, A proposal for discrete modeling of mechanical effects during drying, combining pore networks with DEM, AIChE Journal, 57(4), 872-885, 2011.

[7] A. Kharaghani, T. Metzger, E. Tsotsas, An irregular pore network model for convective drying and resulting damage of particle aggregates, Chemical Engineering Science 75, 267-278, 2012.

[8] Y.J. Wang, A. Kharaghani, T. Metzger, E. Tsotsas, Pore network drying model for particle aggregates: Assessment by X-ray microtomography, Drying Technology 30, 1800-1809, 2012.

[9] F. Chauvet, P. Duru, S. Geoffroy, M. Prat, Three periods of drying of a single square capillary tube, Physical Review Letters 103, 124502, 2009.

[10] N. Vorhauer, Y. Wang, A. Kharaghani, E. Tsotsas, M. Prat, Drying with formation of capillary rings in a model porous medium, Transport in Porous Media 110(2), 197-223, 2015

[11] J. Bear, Y. Bachmat, Introduction to modeling of transport phenomena in porous media, Springer, 1990.

[12] J. Philip, D. De Vries, Moisture movement in porous materials under temperature gradients, Transactions of American Geophysical Union 38, 222-232, 1957.

[13] A.V. Luikov, Heat and mass transfer in capillary-porous bodies, 1st English ed., Oxford: Pergamon,1966.

[14] S. Whitaker, Simultaneous heat, mass, and momentum transfer in porous media: A theory of drying, Advances in Heat Transfer 13, 119-203, 1977.

[15] S. Whitaker, Coupled transport in multiphase systems: A theory of drying, Advances in Heat Transfer 31, 1-103, 1998.

[16] S. Whitaker, The method of volume averaging, Springer, 1999.

[17] O.A. Plumb, Transport phenomena in porous media: Modeling the drying process, Handbook of Porous Media, ed. K. Vafai, New York: M. Dekker, 2000.

[18] P. Perré, R. Rémond, I.W. Turner, Comprehensive drying models based on volume averaging: Background, application and perspective, Modern Drying Technology. Volume 1: Computational tools at different scales, eds. A.S. Mujumdar, E. Tsotsas, Weinheim: Wiley-VCH, 2007.

[19] S. Geoffroy, M. Prat, A review of drying theory and modelling approaches. Chapter 7. Drying and Wetting of Building Materials and Components, Building Pathology and Rehabilitation, ed. J.M.P.Q. Delgado, Springer, 2014.

[20] O. Krischer, Die wissenshaftlichen Grundlagen der Trocknungstechnik, Berlin: Springer, 1963.

[21] C. Peishi, D.C.T. Pei, A mathematical model of drying processes, International Journal of Heat and Mass Transfer 32, 297-310, 1989.

[22] M. Suzuki, S. Maeda, On the mechanism of drying of granular beds, Journal of Chemical Engineering of Japan 1, 26-31, 1968.

[23] E.-U. Schlünder, On the mechanism of the constant drying rate period and its relevance to diffusion controlled catalytic gas phase reactions, Chemical Engineering Science 43, 2685-2688, 1988.

[24] T. Metzger, E. Tsotsas, M. Prat, Pore network models: A powerful tool to study drying at the pore level and understand the influence of structure on drying kinetics, Modern Drying Technology. Volume 1: Computational tools at different scales, eds. A.S. Mujumdar, E. Tsotsas, Weinheim: Wiley-VCH, 2007.

[25] M. Prat, Pore network models of drying, contact angle and films flows, Chemical Engineering Technology 34(7), 1029-1038, 2011.

[26] O. Chapuis, M. Prat, Influence of wettability conditions on slow evaporation in two-dimensional porous media, Physical Review E 75, 046311, 2007.

[27] G. Voronoi, Nouvelles applications des paramètres continus à la théorie des forms quadratiques, Journal für die Reine und Angewandte Mathematik 133, 97-198, 1908.

[28] A. Kharaghani, Irregular pore networks and mechanical effects during drying of porous media, PhD thesis, Otto von Guericke University Magdeburg, 2010.

[29] R. Hilfer, Macroscopic capillarity without a constitutive capillary pressure function, Physica A, 371, 209-225, 2006.

[30] M. Scheel, R. Seemann, M. Brinkmann, M. Di Michiel, A. Sheppard, S. Herminghaus, Liquid distribution and cohesion in wet granular assemblies beyond the capillary bridge regime, Journal of Physics: Condensed Matter 20, 494236, 2008.

[31] A.G. Yiotis, A.G. Boudouvis, A.K. Stubos, I.N. Tsimpanogiannis, Y.C. Yortsos, Effect of liquid films on the isothermal drying of porous media, Physical Review E 68, 037303, 2003.

[32] A.G. Yiotis, D. Salin, E.S. Tajer, Y.C. Yortsos, Drying in porous media with gravity-stabilized fronts: Experimental results, Physical Review E 86, 026310, 2012.

[33] M. Prat, On the influence of pore shape, contact angle and film flows on drying of capillary porous media, International Journal of Heat and Mass Transfer 50, 1455-1468, 2007.

[34] Y.J. Wang, H.T. Mahmood, A. Kharaghani, E. Tsotsas, Visualization and modeling of liquid film rings observed during drying of particle packings, 19th International Drying Symposium, Lyon, France, 2014.

[35] A.A. Moghaddam, A. Kharaghani, M. Prat, E. Tsotsas, Moisture transport coefficients in drying porous media. 7th International Conference on Porous Media & Annual Meeting, Padova, Italy, 2015.

[36] T.H. Vu, Influence of pore size distribution on drying behavior of porous media by a continuous model, PhD thesis, Otto von Guericke University Magdeburg, 2006.

[37] S.X.Q. Lin, X.D. Chen, The reaction engineering approach to modelling the cream and whey protein concentrate droplet drying, Chemical Engineering and Processing 46, 437-443, 2007.

[38] X.D. Chen, A. Putranto, Modelling drying processes: A reaction engineering approach, Cambridge University Press, 2013.

[39] M. Dadkhah, M. Peglow, E. Tsotsas, Characterization of the internal morphology of agglomerates produced in a spray fluidized bed by X-ray tomography, Powder Technology 228, 349-358, 2012.

[40] F. Sondej, A. Bück, K. Koslowski, P. Bachmann, M. Jacob, E. Tsotsas, Investigation of coating layer morphology by micro-computed X-ray tomography, Powder Technology 273, 165-175, 2015.

[41] I.N. Tsimpanogiannis, Y.C. Yortsos, S. Poulou, N. Kanellopoulos, A.K. Stubos, Scaling theory of drying in porous media, Physical Review E, 59, 4353, 1999.

[42] S. Veran-Tissoires, M. Marcoux, M. Prat, Discrete salt crystallization at the surface of a porous medium, Physical Review Letters 108, 054502, 2012.

[43] Attari Moghaddam, A. ; Prat, M. ; Tsotsas, E. ; Kharaghani, A. Evapo- ration in capillary porous media at the perfect piston-like invasion limit: Evidence of nonlocal equilibrium effects. Water Resour. Res., 2017, 53(12), 10433-10449.

[44] Joekar-Niasar, V., Doster, F., Armstrong, R. T., Wildenschild, D., & Celia, M. a. (2013). Trapping and hysteresis in two-phase flow in porous media: A pore-network study. Water Resources Research, 49(7), 4244–4256.

[45] Lefort, Philippe. Etude des déplacements eau-gaz dans les argilites du callovo-oxfordien à l'aide de la théorie de la percolation en gradient. PhD, Institut National Polytechnique de Toulouse, 2014

[46] Babalievski, F., Cluster counting: the Hoshen-Kopelman algorithm versus spanning tree approaches, International Journal of Modern Physics C, Vol 9, No 1, (1998), p. 43-60

Chapter 3

About Schlünder's model: A numerical study of evaporation from partially wet surfaces

3.1 Introduction

One of the most puzzling aspects of drying of porous media is the possible existence of a long constant rate period (CRP), namely a period over which the evaporation rate varies little whereas the water content varies appreciably. Since drying is a phenomenon coupling internal transfers, that is, inside the porous media, and external transfers, that is, in the gas phase at the evaporative surface of the porous medium, both types of transfer should play a role in the existence and duration of the CRP. Qualitatively, the CRP is "explained" from an internal transfer standpoint by the fact that capillary effects can maintain the surface sufficiently wet. This can also be viewed as a consequence of the capillary pumping effect (see below). It is now well known that drying of porous media can be analyzed within the realm of two-phase flow theory in porous media [1] as an invasion percolation process.[2, 4] This means that the bigger pores are first invaded whereas smaller pores stay wet at the surface. For a meniscus to stay at the entrance of a smaller pore at the surface, a liquid flow in this pore should equilibrate the evaporation rate from this pore. This is the capillary pumping effect, that is, a net flow from the inside of the medium toward the smaller pores at the surface. However, since bigger pores are invaded, the density of wet pores (fraction of the pores at the surface with a pinned meniscus) decreases during the CRP. In other terms, the surface is less and less wet but this does not change appreciably the evaporation rate, at least as long the surface wet fraction is high enough.

Then we have to explain why the evaporation rate from a partially wet surface can remain approximately unchanged whereas the surface becomes less and less wet. This is essentially the point studied by Schlünder.[5, 6] Extending the work of Suzuki and Maeda,[7] Schlünder essentially showed that the evaporation rate from a surface covered by discrete wet spots is essentially the same as the evaporation rate from the same surface totally wet provided that the wet spots are evenly distributed over the surface and their diameter is small compared to the typical thickness of the external mass transfer layer. This result was obtained assuming that the external mass transfer is governed by diffusion, at least in a small layer adjacent to the surface (the viscous sub-layer in the analysis of Schlünder), for example, Haghighi et al.[8] The analytical relationship proposed by Schlünder reads

$$\frac{J}{J_{ref}} = \frac{1}{1 + \frac{2}{\pi}\frac{r_p}{H}\sqrt{\frac{\pi}{4\theta}}\left[\sqrt{\frac{\pi}{4\theta}} - 1\right]} \tag{3.1}$$

where J is the evaporation rate, H is the tickness of the diffusive layer adjacent to the surface, r_p is the radius of the wet spots (pores) at the surface. $\theta = \frac{\pi r_p^2}{a^2}$ is the wetted fraction of the surface where a is the size of a square unit cell with a circular pore opening in its center (see Figure 3.1(a)).

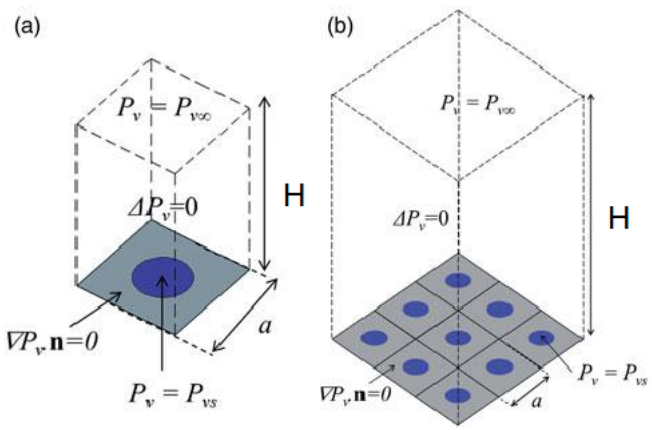

Figure 3.1: Computional domains: (a) single unit cell and (b) 3 x 3 square arrangement of wet surface pores.

The length a can also be interpreted as the mean distance between the pores at the surface. In Equation (3.1), J_{ref} is the evaporation rate when the surface is entirely covered by liquid,

$$J_{ref} = \frac{M_v}{RT} D a^2 \frac{(P_{vs} - P_{v\infty})}{H} \tag{3.2}$$

where M_v, R, and T are the water molecular weight, the universal gas constant, and the temperature. D is the molecular diffusion coefficient of vapor in the binary mixture formed by air and the vapor. P_{vs} and $P_{v\infty}$ are the vapor pressure at the pore surface (saturated vapor pressure) and in the external gas at the distance H from the porous surface, respectively.

Hence Equation (3.1) provides an explicit relationship between the evaporation rate and the degree of occupancy of the porous surface by the liquid.

Schlünder's relationship thus analyzes the CRP from a pure external mass transfer standpoint. However, as discussed in Moghaddam et al. and Lehmann and Or, [9, 10] drying is less simple than considered in Schlünder's analysis. For instance, the pore sizes are not uniform at the surface and vary from one pore to another. The impact of this variability must be assessed. Nevertheless, Schlünder's relationship is still today the only analytical expression linking the evaporation rate to the degree of occupancy of the surface by the liquid. Since the evaporation rate decreases according to Equation (3.1) when θ is sufficiently small, Equation (3.1) was also used later by Schlünder [11] to explain the end of the CRP and thus the transition toward the falling rate period (FRP), another key issue in the drying theory.

Since drying is essentially a coupled problem between the transfer inside the porous medium and in the external gas domain with which the porous medium is in contact on one or several sides, the correct modeling of the coupling is crucial. In the simpler approach, the mass transfer at the surface is modeled using a mass transfer coefficient, for example, Chen and Pei.[12] Thus in the case, the equations governing the mass transfer in the external gas are not solved explicitly all along the drying process. The problem with this approach is that the variation of the mass transfer coefficient during the drying process is not known. Therefore this approach is rarely truly predictive. A more satisfactory approach consists in solving together the equations governing the transfer in the external gas and inside the porous medium. Such an approach when the transfers inside the porous medium are modeled using the continuum approach to porous media can be found, for example, in the references.[12, 17] A somewhat similar coupling strategy has also been developed in relation with the pore network modeling (PNM) of drying, for example, Xu and Pillai.[18] Although the general approach involving to solve the Navier–Stokes equations together with the vapor transport equation is certainly the most versatile in relation with drying problems, simplified versions can also be useful, for instance in order to perform comparisons with laboratory experiments, for example, Veran and Prat.[19] Such a simple case is when the external mass transfer is essentially driven by diffusion, a situation thus similar to the situation considered by Schlünder. One can thus wonder whether Schlünder's formula or a variant of Schlünder's formula could

be useful in relation with the PNM of drying. In this respect, it should be noted that the results presented in Moghaddam et al.[9] as well as in previous works using a pore network model, for example, Yiotis et al.,[20] were based on simulations using a quite coarse grid in the external mass transfer boundary layer. Clearly, this aspect of PNM needs improvement.

To sum up, the objectives of the present paper are triple: (1) assessing Schlünder's relationship for a greater variety of wet pore shapes than in previous works, (2) looking at the asymptotic case where the wet spots are far apart from each other, and (3) adapting Schlünder's formula to the case of heterogeneous surface for application to the PNM simulations of drying.

3.2 Method

The study is based on numerical solutions of the diffusion equation governing the vapor concentration in the external mass transfer boundary layer. As depicted in Figure 3.1, the computational domain Ω is a parallelepiped domain with the partially wet surface localized at its bottom. Using the vapor partial pressure P_v as main variable, the problem to be solved in Ω reads

$$\Delta P_v = 0 \tag{3.3}$$

where Δ is here the Laplacian (Laplace operator). Equation (3.3) thus corresponds to the steady-state diffusion equation when the temperature variations can be ignored and the diffusion coefficient is constant. On the lateral boundaries, a zero flux condition is imposed ($\nabla P_v.\mathbf{n} = 0$, where $\mathbf{n}$ is the unit normal vector at the considered surface). On the top surface, the vapor partial pressure is known,

$$P_v = P_{v\infty} \ \ \textbf{at } z = H \tag{3.4}$$

On the partially wet surface $\partial\Omega_b$ (bottom surface at $z = 0$), the vapor partial pressure is known on the wet regions, that is

$$P_v = P_{vs} \ \ \textbf{at } z = 0 \textbf{ on } \partial\Omega_{bw} \tag{3.5}$$

where P_{vs} is the saturated vapor pressure at the considered temperature (the temperature is uniform all over the computational domain). On the solid part of $\partial\Omega_b$, a zero flux condition is imposed

$$\nabla P_v.\mathbf{n} = 0 \ \ \textbf{at } z = 0 \textbf{ on } \partial\Omega_{bs} \tag{3.6}$$

Equations (3.3)–(3.6) are solved using the simulation software COMSOL Multiphysics. Once the vapor pressure field has been computed the evaporation rate is computed as

$$J = \int_{\Omega_{bw}} \left(-D \frac{M_v}{RT} \nabla P_v . \mathbf{n} \right) \, \mathrm{d}\Omega \ \textbf{at} \ z = 0 \tag{3.7}$$

In typical drying experiments, H is on the order of 1 mm while a typical mean distance between pores is of the order of 100 µm or less. Thus, unless otherwise mentioned, all the simulations presented in what follows have been performed for H = 1 mm and a = 100 µm. However, it can be noted that what matters is actually the ratio H/a. Thus, the presented results directly apply to other values of a or H as long as H/a = 10.

3.3 Influence of pore shape

To derive his formula, Schlünder has actually considered a system of hemi-spherical droplets. Assuming a square arrangement of the droplets, he actually considered a single unit cell of parallelepiped shape with a droplet lying in the middle of the bottom surface of the parallelepiped domain. Since pores are not hemi-spherical droplets, it is interesting to examine the impact of the pore shape. Circular pores are obvious candidates but it is clear that the pore shape is often quite different from a circular tube. For this reason, we have also tested other elementary shapes such as square, triangle, and star shapes.

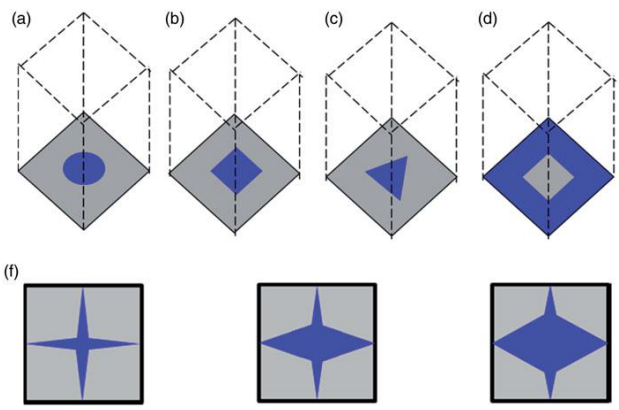

Figure 3.2: Various surface elementary pore shapes (wet zone in blue, solid surface in grey): (a) circular, (b) square, (c) triangle, (d) square complement, and (e) Star shapes corresponding to $\theta = 0.1$, $\theta = 0.2$, and $\theta = 0.3$, respectively.

The various tested shapes are depicted in Figure 3.2 while a comparison between the results obtained using Schlünder's relationship and the results obtained numerically for the different shapes is presented in Figure 3.3.

To perform this comparison we keep H = 1 mm and a = 100 µm and vary the wet surface area S_w for the various shapes. Thus, $\theta = \frac{S_w}{a^2}$. To use Equation 3.1, we also need to specify the pore radius r_p.

For shapes different from the circular shape, we define r_p as the circular pore radius having the same wetted area as the considered shape. Hence r_p is determined from the relationship $\pi r_p^2 \approx S_w$.

As can be seen from Figure 3.3, the variation of the evaporation rate with θ is sensitive to the pore shape.

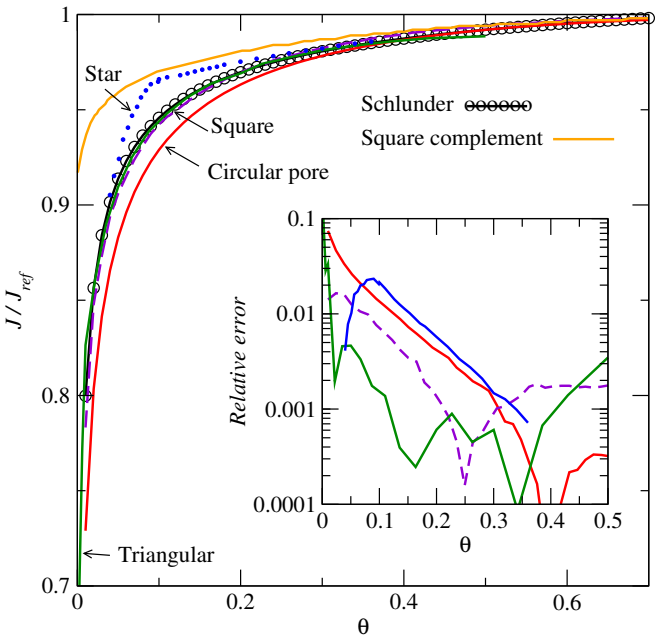

Figure 3.3: Test of Schlünder's relationship (Eq. (3.1)) for the various pore shapes. H = 1 mm, a = 0.1 mm (the dashed purple line corresponds to the square shape and the green solid line to the triangular shape). The inset shows the relative error between the numerical results and Schlünder's formula (same color code as for the main plot, the error for the square complement is not plotted).

Somewhat surprisingly in view of the analytical method used by Schlünder to derive his formula, the numerical results for the circular pore lead to lower evaporation rates compared to the estimate with Schlünder's formula.
It is important to mention here that very refined meshes were used to obtain the results shown in Figure 3.3. So the discrepancy cannot be attributed to a lack of mesh refinement. It is attributed to the approximation made by

Schlünder in deriving his formula. However, the agreement with Schlünder's formula is excellent for the square and triangle pore shapes. The star shape leads to a greater discrepancy, at least for θ around 0.1. Note that the star shape is anisotropic (see Figure 3.2(f)) and it is the shape which is obviously the less closer to a circular shape among the considered shapes. As shown in the inset in Figure 3.3, the relative error $\mid J_{num} - J_{Schl} \mid / J_{Schl}$, is, however, reasonably low for all shapes, that is, less than 10% and actually on the order of a few percent only, except with the circular and triangle shapes for $\theta < 0.05$. The case of the very low θ is examined in more details after the next section, which briefly presents the results obtained for the case of the square complement (Figure 3.2(d).)

3.4 A counter – example

Since Schlünder's formula was derived considering a spatially periodic square arrangement of droplets, it can be expected that it leads to much less good results when the distribution of the liquid at the surface is markedly different from an even distribution of isolated wet spots.
Consider, for example, the situation where the central region of the unit cell corresponds to a solid surface (no flux) whereas the complementary surface is wet (the case of square unit cell is illustrated in Figure 3.2(d)). The comparison between the simulations and the predictions using Schlünder's formula for this case is depicted in Figure 3.3 (compare the orange line with the black line with empty circles). As can be seen, using Schlünder's formula is not a good idea for this case.
In summary, as illustrated with this example as well as with the star shape if the wet region shape in the unit cell is too different from a circular pore, Schlünder's formula is not reliable. Of course, it can be noted that this essentially holds when Schlünder's formula indicates a noticeable impact of θ on the evaporation rate, that is, when θ is sufficiently low ($\theta < 0.3$ in Figure 3.3).

3.5 Evaporation rate for very low wetted surface fractions

The motivation for studying the evaporation rate when the wetted surface fraction is very low comes from the study of saline evaporation from porous media, for example, Eloukabi et al.[21] When a salt crust forms at the surface, it is often observed that the evaporation rate is severely reduced compared to the situation for pure water. The evaporation rate can be reduced by at least one order of magnitude. One simple option to explain this very low evaporation rate is to consider that the crust is still wet but with a quite low density of active pores at its surface (due to pore clogging by the precipitation of the salt). Active pores mean wet pores where evaporation takes place. Thus, we are interested here in Schlünder's relationship when θ « 1. In this limit, Equation (3.1) can be written as

$$\frac{J}{J_{ref}} = \frac{1}{1 + 0.5\frac{r_p}{\theta H}} \approx \frac{2\theta H}{r_p} \approx 2\sqrt{\pi\theta}\frac{H}{a} \approx 2\pi\frac{r_p H}{a^2} \tag{3.8}$$

Thus Schlünder's relationship suggests that the evaporation rate should vary with the square root of wetted surface fraction θ when θ « 1.

Using Equation (3.2), the evaporation rate from a surface element of size a is given in this very low wetted surface fraction limit by

$$J =\approx \frac{2\theta}{r_p}\frac{M_v}{RT}Da^2\left(P_{vs} - P_{v\infty}\right) = 2\pi r_p\frac{M_v}{RT}D\left(P_{vs} - P_{v\infty}\right) \tag{3.9}$$

As it could be expected, Equation (3.9) is almost identical to the expression giving the evaporation rate of a single flat droplet (a disk) on a flat plate in an infinite half-space, for example, Picknett and Bexon [22] and Hu and Larson. [23] The difference only lies in the numerical factor 2π in Equation (3.9) versus 4 for the isolated droplet expression.[22, 23] As indicated by Equation (3.9), a key characteristic of diffusive evaporation is that the evaporation rate is proportional to the perimeter of the droplet and not to its surface area. The difference in the prefactor is not surprising since the conditions considered by the different authors to derive their analytical expression are different. Whereas Schlünder considered the evaporation from a half sphere in a spatially periodic system, Picknett and Bexon [22] and Hu and Larson [23] considered the somewhat simpler case of a single droplet in an infinite half-space. In order to evaluate the applicability of Equation (3.8), we have computed the evaporation rate for the situation depicted in Figure 3.1(a) for θ varying in the range [10^{-6}- 10^{-3}] (which corresponds to

r_p/a varying between 5.64 x10^{-4} and 0.0178 for a circular pore). The results are shown in Figure 3.4.

As can be seen, the overall tendency between the results from Schlünder's formula and the numerical simulations are similar. As shown in the inset in Figure 3.4, the relative error is greater for this range of very low wetted surface fractions (except, however, for the circular pore when $\theta < 10^{-5}$) compared with the results shown in Figure 3.3 for greater θ. The agreement with the formula for an isolated droplet leads as expected to similar results as Schlünder's formula for sufficiently low θ (with the discrepancy due to the numerical prefactor 2π versus 4). The comparison with the numerical simulations suggests that Schlünder's formula is more appropriate. However, as shown in Figure 3.4, the relative error between the numerical simulations and Equation (3.9) can be relatively high.

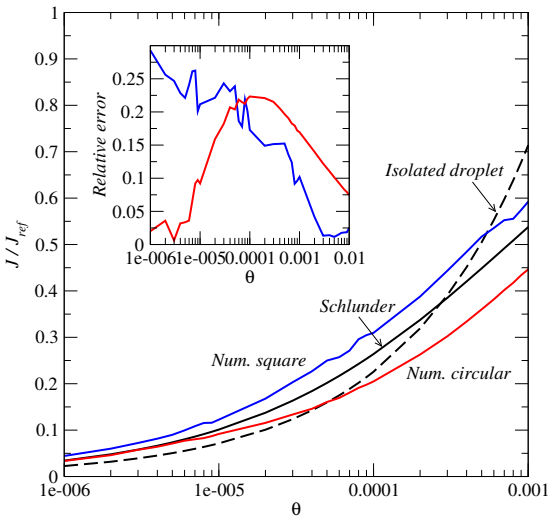

Figure 3.4: Test of Schlünder's relationship in the limit of very low wetted surface fractions as given by Eq. (3.8). The inset shows the relative error between the numerical results and Schlünder's formula (same color code as for the main plot).

Further investigations are needed to clarify this point, which might be due in part to a combination of numerical inaccuracies owing to the very small region occupied by the wetted surface in the computational domain and the inaccuracy of the Schlünder's formula in the limit of very small θ. Based on the results shown in Figure 3.4, a very low θ, on the order of 10^{-5}, must be considered here to reduce the evaporation rate by a factor 10 compared to the evaporation rate for a fully wet surface. This corresponds to r_p/a $\approx$ 1.8 x 10^{-3} (corresponding, for example, to pores of 360 nm in diameter 100 µm away from each other). It can be argued, however, that the boundary

layer thickness H is probably affected when the active pores are so sparsely distributed over the surface. Thus, this situation of very low evaporation probably needs further investigation.

3.6 Influence of disorder

Pore sizes are not uniform in a porous medium but vary from one pore to another. Thus, it is interesting to look at the impact of the pore size variability. Here several options are possible. One can play for instance with the distance between two neighbor pores and/or the pore diameters or the pore shapes. Varying the shape, for example, sounds a bit less relevant since the pore shapes should be similar for a given porous medium. So, square pores are considered. For simplicity, we have decided to only vary the pore side length (and thus not the distance between the pore centers).

A square arrangement of pore openings at the surface is considered for a fixed distance between the centers of two neighbor pores. The pore side lengths are selected randomly as follows. Similarly as in Figure 3.1(b), a surface with 3 x 3 pore openings is considered (but the openings are square and their sizes vary). First, we select a range of θ, namely $[\theta_{min}, \theta_{max}]$. Then we select nine values in this range roughly evenly distributed. Then the nine values are randomly located over the nine locations at the surface. The side length d of each pore is then deduced from the definition of θ, $\theta = d^2/a^2$. A surface with nine values of θ so distributed is called a realization of the surface. A total of four realizations of the surface are considered in what follows.

The local wetted surface fraction is defined as

$$\theta_i = \frac{d_i^2}{a^2} \tag{3.10}$$

where i is the pore index. Thus i varies between 1 and 9 since there are 9 pores at the surface.

The global wetted surface fraction is defined as

$$\theta = \frac{\sum_{i=1}^{9} d_i^2}{9a^2} = \frac{1}{9}\sum_{i=1}^{9} \theta_i \tag{3.11}$$

The evaporation rate J_i from each pore is determined by solving Equations (3.3–3.6) for each realization.

Figure 3.5 shows the variation of J_i as a function of θ_i with a comparison with the predictions using locally the Schlünder's formula (i.e.,Equation (3.1)

with $\theta = \theta_i$, r_{pi}= $d_i/\sqrt{\pi}$) for values of θ in the range [0.001–0.48]. As can be seen, using locally Schlünder's formula, that is, for each cell at the surface, leads to poor results.The evaporation rate is underestimated for θ_i approximately greater than 0.15 and overestimated for lower θ_i . The variability of the local evaporation rate is quite high (between about 10% of J_{ref} and 150% of J_{ref}).

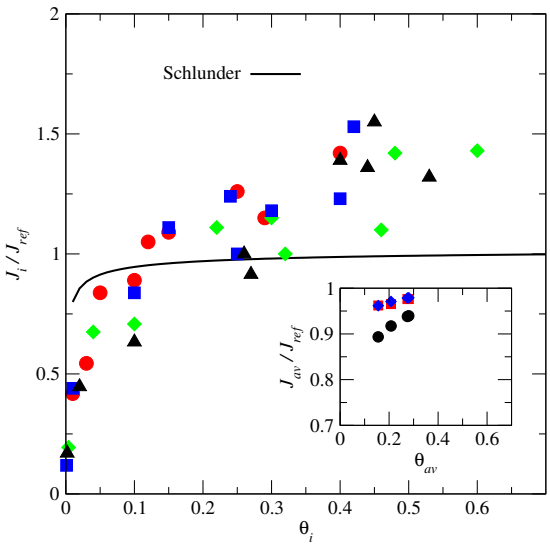

Figure 3.5: Variation of J_i/J_{ref} with θ_i where J_{ref} is given by Eq.(2), H = 10 mm, a = 1 mm. Each type of symbol (filled circles,square, diamond, and triangle) corresponds to one realization of the 3 x 3 surface. The inset shows the variation of the average evaporation rate with average θ (black symbols: Schlünder's formula option #1 (i.e., Eq. (3.1) with Eq. (3.12)), blue symbols: Schlünder's formula option #2 (i.e., Eq. (3.1) with Eqs.(3.13–3.14)), red symbols: average values from the numerical simulation over the four realizations of the 3x3 surface).

Thus the evaporation rate can be locally 50% greater than the evaporation rate corresponding to a fully wet cell. This is explained by the impact of neighbor pores. It is expected that the evaporation rate from a given pore is greater when the neighbor pores are small on average than when the neighbor pores are greater. This is illustrated in Figure 3.6 for a special 3 x 3 surface with only two sizes of pore. The pore in the middle of size d_{mi} (corresponding to θ_{mi}) and the eight neighbor pores of size d_{ne} (corresponding to θ_{ne}). Figure 3.6 shows the variation of the evaporation rate from the middle cell for two different wet surface fraction θ_{mi} as a function of neighbor cell wet surface fraction θ_{ne}.

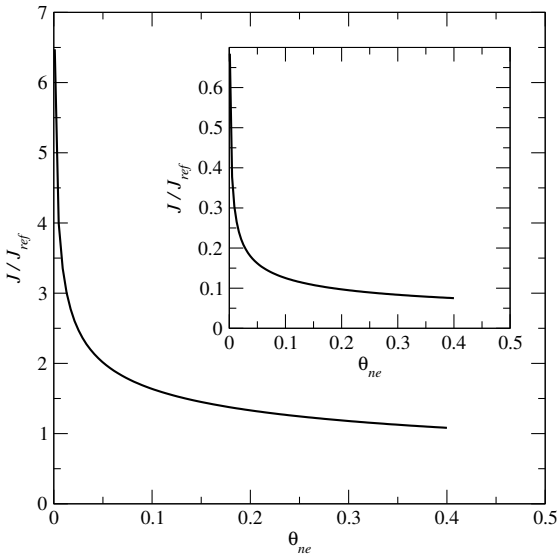

Figure 3.6: 3 x 3 surface with two pore scales. Variation of the evaporation rate from the middle cell for two different wet surface fraction θ_{mi} as a function of neighbor cell wet surface fraction θ_{ne} . Main plot $\theta_{mi} = 0.4$; inset $\theta_{mi} = 0.001$.

As depicted in Figure 3.6, the greater are the neighbor pores, the lower the evaporation rate from the middle pores. Also, consistently with the results shown in Figure 3.5, the dimensionless evaporation rate is greater than one when the middle poresize is greater than the neighbor pore size.

Conversely, the dimensionless evaporation rate is lower than one when the middle pore is smaller than the neighbor pores. Whereas it is clear from Figure 3.5 that the simple application of Schlünder's formula to each cell does not lead to good results, one can wonder whether Schlünder's formula can still be used to predict the overall evaporation rate. To this end, two options are considered. Option 1 consists in using the radius corresponding to the whole wet surface area as equivalent pore radius,

$$r_{popt1} = \sqrt{\frac{\sum_{i=1}^{9} \theta_i a^2}{\pi}} \tag{3.12}$$

and for θ,

$$\theta_{popt1} = \frac{\sum_{i=1}^{9} \theta_i a^2}{9a^2} = \frac{1}{9} \sum_{i=1}^{9} \theta_i \tag{3.13}$$

The second option consists in using the average equivalent pore radius, that

is

$$r_{popt2} = \frac{1}{9}\sum_{i=1}^{9}\sqrt{\frac{\theta_i a^2}{\pi}} \tag{3.14}$$

with θ_{popt2} =θ_{popt1}. Thus the difference between the two options lies in the definition of the equivalent pore radius. The equivalent pore radius corresponds to the whole wet surface with option 1 and to the average equivalent pore radius with option 2. As can be seen from the inset in Figure 3.5, option 2 leads to a good agreement with the numerical values. In other terms, replacing the heterogeneous surface by a homogenous surface of nine identical pores having the same size as the average pore size of the heterogeneous surface leads to the same evaporation rate as for the heterogeneous surface.

3.7 Extension of Schlünder formula to heterogeneous surfaces

Since the size of neighbor pores has an impact, a simple idea is to associate an influence surface A_i with each pore at the surface. How A_i can be determined is explained below. Then the evaporation rate from pore i can be estimated using Equation (3.1) as

$$\frac{J_i}{J_{refi}} = \frac{1}{1 + \frac{2}{\pi}\frac{r_{pi}}{H}\sqrt{\frac{\pi}{4\theta_i}}\left[\sqrt{\frac{\pi}{4\theta_i}} - 1\right]} \tag{3.15}$$

with $J_{refi} = \frac{M_v}{RT} D A_i \frac{(P_{vs} - P_{v\infty})}{H}$, $\theta_i = \frac{d_i^2}{A_i}$, $r_{pi} = \frac{d_i}{\sqrt{\pi}}$. Under these circumstances, the evaporation rate from pore #i is given by

$$\frac{J_i}{J_{refi}} = \frac{(A_i/a^2)}{1 + \frac{2}{\pi}\frac{r_{pi}}{H}\sqrt{\frac{\pi}{4\theta_i}}\left[\sqrt{\frac{\pi}{4\theta_i}} - 1\right]} \tag{3.16}$$

where a^2 is the surface area of a cell at the surface and J_{ref} is given by Equation (3.2).

In addition to Equation (3.16), we have also tested a formula in which the impact of the influence surface is taken into account with a power of 2, namely

$$\frac{J_i}{J_{refi}} = \frac{(A_i/a^2)^2}{1 + \frac{2}{\pi}\frac{r_{pi}}{H}\sqrt{\frac{\pi}{4\theta_i}}\left[\sqrt{\frac{\pi}{4\theta_i}} - 1\right]} \tag{3.17}$$

For using Equations (3.16) or (3.17), we have to determine the influence surface area A_i for each pore i.

The idea is simple and consists in making a tessellation of the surface as illustrated for realization #1 in Figure 3.7. The influence surface area of a pore is the set of points of the surface which are closer to this pore than to any other pore. To determine the influence surface we use a discrete method based on the pixelization of the surface and determine the number of pixels corresponding to each influence surface.

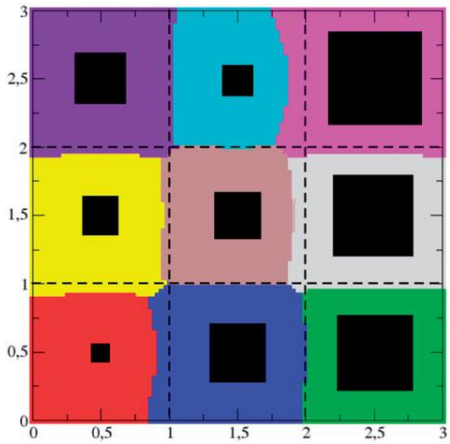

Figure 3.7: Illustration of the influence surfaces (colored areas) associated with each pore (black filled square) at the surface. The dashed lines delineate the boundary of each cell at the surface. The influence surface area of a pore is the surface area of the pore together with the area of the colored surface surrounding the pore. The stairs at the boundary between two influence surfaces are due to the discrete method used to determine the boundary.

To obtain the tessellation shown in Figure 3.7, the whole surface was tiled by 100 x 100 square pixels of size 3a/100. Application of Equations (3.16) and (3.17) then leads to the results shown in Figures 3.8 and 3.9. As can be seen, the use of Equations (3.16) or(3.17) significantly improves the prediction from simple formula of Schlünder type. This is better seen in Figure 3.9, which clearly shows that Equation (3.17) is the best option. Although the overall trend in Figure 3.9 is quite good, the scattering for some points in Figure 3.8 is noticeable.

Also, it can be noted that the discrepancy between the simulations and the prediction from Equation (3.17) is greater for the smaller pores, which correspond to pores where the evaporation rate rapidly varies with θ_i.

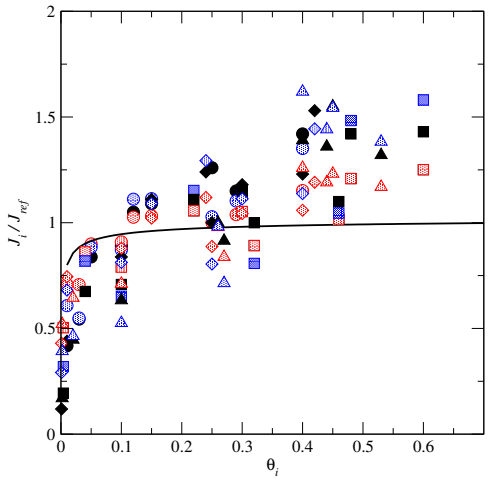

Figure 3.8: Variation of pore evaporation rate J_i as a function of the corresponding surface cell wetted surface fraction θ_i $(= d_i^2/\ a^2)$. The black solid line corresponds to standard Schlünder's formula Eq. (3.1). The black symbols correspond to the numerical simulations for the four realizations (each type of symbol, circle, square, diamond, triangle, corresponds to one realization). The blue symbols correspond to Eq. (3.16) and the red ones to Eq. (3.17).

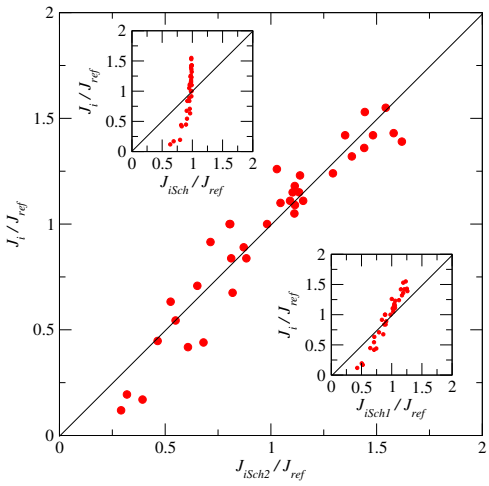

Figure 3.9: Comparison between the evaporation rate from each pore computed numerically and the predictions from the various variants of Schlünder's formula for the 3x3 surface. The main plot is the comparison with Eq. (3.17). The inset on the top left shows the comparison with the standard Schlünder's formula (Eq. (3.1)). The inset on the bottom right shows the comparison with Eq. (3.16).

Another idea is to consider the evaporation rate variable. In this sense, the streamline comsol method was used. The surface of influence is then the set of points of the upper surface connected to the pore considered by evaporation rate streamline, (Figure 3.10)

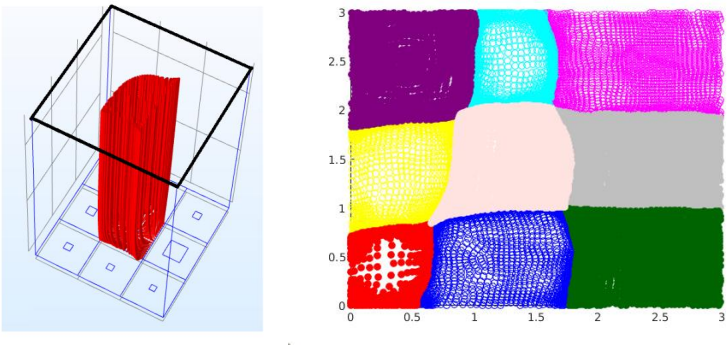

Figure 3.10: Illustration of the influence surfaces (right figure) associated with each pore (square at the left figure) at the top of the parallelepiped using streamline method from comsol.

By applying the two Schlünder formula Equations (3.16) and (3.17) this time, we notice that contrary to the tesselation based on pixelization, an area of influence with an order one is sufficient to compare with the numerical results Figure 3.11.

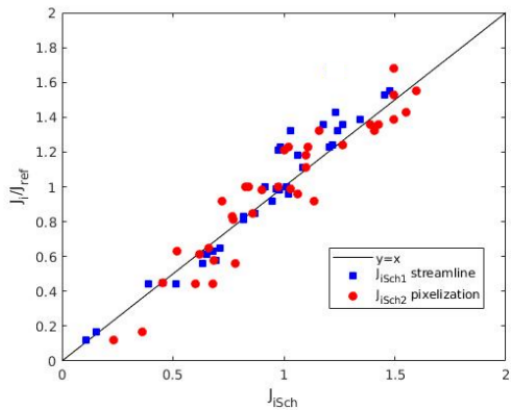

Figure 3.11: Comparison between the evaporation rate from each pore computed numerically and the predictions from the various variants of Schlünder's formula for the 3 x 3 surface. The blue symbol correspond to surface influence from streamline method, the red symbol correspond to surface influence from pixelization method.

Algorithm such as Voronoi tessellation,[24] can also be used to perform the tesselation. Improving the computational efficiency of the tessellation will be important for extending the method to surface containing a large number of pores.

3.8 External mass transfer and PNM

As presented for example in Moghaddam et al.[9] or Metzger et al.,[25] a method for computing the diffusive external mass transfer in the pore network models of drying consists in setting computational nodes in the external layer of size H. However, as illustrated in Figure 3.12, the distance between two computational nodes is generally taken as the distance between two pores in the network (also referred to as the lattice spacing a).

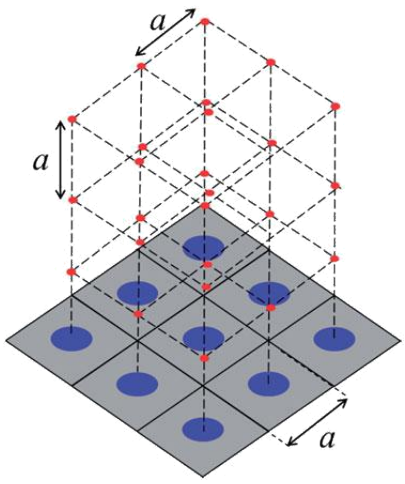

Figure 3.12: Typical distribution of computational nodes (red dots) in the external diffusive mass boundary layer in PNM of drying.

Obviously, this is a quite coarse discretization, sufficient to get qualitative results but questionable if the objective is to quantitatively compute the transfer by diffusion in this layer.[18] In this context, the objective is to assess the impact of this coarse discretization on the mass transfer at the boundary of the network and also to explore whether the use of Equations (3.1) or (3.17) could be a better option.
Consider the case when the pore size does not vary over the surface. Thus, we can consider only a unit cell as depicted in Figure 3.1(a). The finite volume discretization of the diffusive mass transfer using the coarse discretization

classically used in PNM leads to compute the evaporation rate as (see Appendix)

$$\frac{J_{PNM}}{J_{ref}} = \frac{2\theta n}{2\theta(n-0.5)+1} \tag{3.18}$$

where n = H/a is the number of finite volumes used in the vertical direction to discretize the boundary layer. A comparison between the results obtained from Equation (3.18) and from Schlünder's formula (Equation (3.1)) is presented in Figure 13 considering again the representative values H = 1 mm, a = 0.1 mm.

We know from previous sections that Schlünder's formula leads to quite accurate results for this case. Thus, it is clear from the comparison shown in Figure 3.13 that the coarse discretization used in several previous works with PNM is not satisfactory.

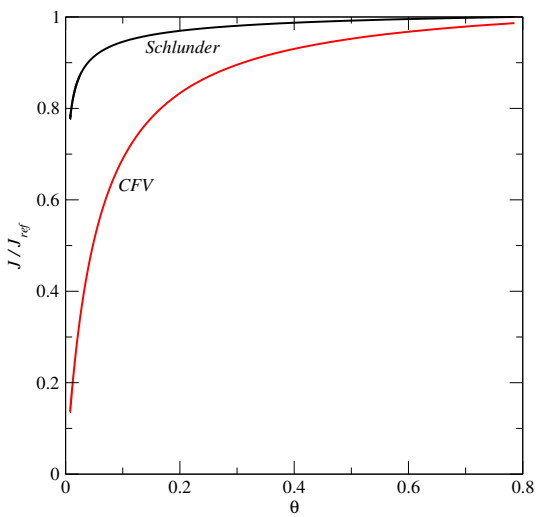

Figure 3.13: Comparison between the results from a coarse finite volume discretization (CFV, Eq. (3.18)) and from Schlünder's formula (Eq. (3.1)). H = 1 mm, a = 0.1 mm.

A finer discretization is necessary for accurate results. Based on the above, a simpler and better option would be to use the modified Schlünder's formula, that is, Equation (3.17), as boundary condition for each cell at the evaporative surface instead of the coarse discretization. This approach does not require setting computational points in the boundary layer and therefore is more computationally efficient than the usual coarse discretization method. It only needs a pre-processing step for determining the influence surface area of each pore at the surface.

3.9 Summary and discussion

The modeling of drying implies to couple the external and internal transfers. The full coupled approach implies to solve the governing equations also in the external gas. This is computationally time consuming. Developing simplified approaches is therefore highly desirable. In fact, this problem is usually circumvented by the use of a mass transfer coefficient at the surface. This is not satisfactory in general because the spatial and temporal variations of this coefficient are generally not known a priori. Actually, this type of coefficient is rather used as a fitting parameter. This can be useful in practice but not satisfactory from a modeling/theoretical standpoint. In this context, Equation (3.1) provides a simple relationship to determine the evaporation rate from a partially wet surface when the external transfer is dominated by diffusion.

In this work, we have explored the value of Schlünder's formula, that is, Equation (3.1), as a possible relationship for computing the evaporation rate from the individual pores of a model porous surface. When the surface is spatially periodic with a uniform pore size, Schlünder's formula provides a quite reasonable estimate of the evaporation rate. However, the quality of the prediction depends on the pore shape, that is, on how the wet fraction is distributed over the surface cells. Also, the estimate is less good for very small wet surface fractions.

The consideration of heterogeneous surfaces characterized by a spatial variability in the pore size leads to interesting results, especially in relation with the PNM of drying. The standard application of Schlünder's formula leads to poor results. The evaporation rate from the bigger pores is significantly underestimated whereas the evaporation rate from the smaller pores is significantly overestimated. This is a consequence of the surface heterogeneity. The evaporation rate from a cell depends on the size of neighbor pores. It is greater when the neighbor pores are smaller and lower when they are larger than the pore of the considered cell.

These results led to introduce the concept of pore influence surface in order to take into account the pore size heterogeneity while still using Schlünder's formula.

The influence surface of a pore was defined as the set of the points of the surface closer to this pore than to any other pores. This leads to the tessellation of the whole surface by the influence surfaces and results in a greater influence surface for a larger pore than for a smaller pore. Using the influence surfaces with Schlünder's formula greatly improves the comparison between the analytical prediction of the evaporation rate from each pore at the surface and the evaporation rate obtained from numerical simulations.

Yet, this was obtained by using a correction factor involving the ratio of the influence surface to the cell surface with an exponent equal to 2. Why this value of the exponent leads to better results than an exponent equal to 1 remains to be justified from a theoretical standpoint.

The use of Schlünder's formula with the influence surfaces provides a simple mean to impose the boundary condition at the surface in the PNM of drying when the external transfer is controlled by diffusion over a layer of given thickness. The relatively classical method consisting in computing the transfer in the diffusive layer with a coarse discretization using a discretization step equal to the spacing of the underlying lattice is clearly just a quite crude and inaccurate method. For accurate computations, a much finer discretization is mandatory. In order to avoid the corresponding high computational cost, it is thus recommended to use Schlünder's formula with the influence surface, that is, Equation (3.17). Although less accurate than a refined computation, this approach is much better than the classical approach using the lattice spacing as discretization step.

However, it should be recalled that this method has only been tested over a small surface with only nine pores and only four realizations. More work is needed to confirm the general validity of the method. Basically, surfaces with more pores, as well as other types of surfaces, for instance surfaces where both the distance between two neighbor pores and the pore size vary, must be tested.

Also, we have considered a surface where the vapor concentration is the same at the surface of each pore. As illustrated for instance in Moghaddam et al.[9] from pore network simulations, the vapor concentration at the surface pore entrances actually varies during drying because of the invasion of an increasing fraction of pores by the gas phase. Both the wet pores and the dry pores at the surface contribute to the evaporation rate since vapor transport can also occur through the dry pores. Thus, the impact of the vapor concentration variability on the results obtained from Schlünder's formula with the influence surfaces seems an attractive approach, but as seen by Lu, Tsotsas, Kharaghani,[27] the study of the Schünder's formula when the vapor concentration at the surface of the drying PNM is heterogeneous, leads to poor results, so this formula will not be used in the following chapters.

Funding

Financial support from joint project "Drycap" funded by GIP ANR (project16-CE92-0030-01) and DFG (project TS28/10-1) is gratefully acknowledged.

References

[1] Lenormand, R.; Touboul, E.; Zarcone, C. Numerical Models and Experiments on Immiscible Displacements in Porous Media. J. Fluid Mech. 1988, 189, 165–187.

[2] Shaw, T. M. Drying as an Immiscible Displacement Process with Fluid Counterflow. Phys. Rev. Lett. 1987, 59, 1671–1674.

[3] Tsimpanogiannis, I. N.; Yortsos, Y.; Poulou, S.; Kanellopoulos, N.; Stubos, A. K. Scaling Theory of Drying in Porous Media. Phys. Rev. E. 1999, 59, 4353–4365.

[4] Prat, M.; Bouleux, F. Drying of Capillary Porous Media with a Stabilized Front in Two Dimensions. Phys. Rev. E. Stat. Phys. Plasmas. Fluids. Relat. Interdiscip. Topics. 1999, 60, 5647–5656

[5] Schlünder, E. U. On the Mechanism of the Constant Drying Rate Period and Its Relevance to Diffusion Controlled Catalytic Gas Phase Reactions. Chem. Eng. Sci. 1988, 43, 2685–2688.

[6] Shahraeeni, E.; Lehmann, P.; Or, D. Coupling of Evaporative Fluxes from Drying Porous Surfaceswith Air Boundary Layer: Characteristics of Evaporation from Discrete Pores. Water Resour. Res. 2012, 48, W09525.

[7] Suzuki, M.; Maeda, S. On the Mechanism of Drying of Granular Beds. J. Chem. Eng. Jpn. 1968, 1, 26–31.

[8] Haghighi, E.; Shahraeeni, E.; Lehmann, P.; Or, D. Evaporation Rates Across a Convective Air Boundary Layer Are Dominated by Diffusion. Water Resour. Res. 2013, 49, 1602–1610.

[9] Moghaddam, A. A.; Kharaghani, A.; Tsotsas, E. Prat M. A Pore Network Study of Evaporation from the Surface of a Drying Non-Hygroscopic Porous Medium. AIChE J. 2018, 64, 1435–1447.

[10] Lehmann, P.; Or, D. Effect of Wetness Patchiness on Evaporation Dynamics from Drying Porous Surfaces. Water Resour. Res. 2013, 49, 8250–8262.

[11] Schlünder, E. U. Drying of Porous Material During the Constant and the Falling Rate Period: A Critical Review of Existing Hypotheses. Drying Technol. 2004, 22, 1517–1532.

[12] Chen, P.; Pei, D. C. T. A Mathematical Model of Drying Processes. Int J. Heat Mass Transfer. 1989, 32, 297–310.

[13] Masmoudi, W.; Prat, M. Heat and Mass Transfer Between a Porous Medium and a Parallel External Flow, Application to Drying of Capillary Porous Materials. Int. J. Heat Mass Trans. 1991, 34, 1975–1989

[14] Erriguible, A.; Bernada, P.; Couture, F.; Roques, M. A. Modeling of Heat and Mass Transfer at the Boundary Between a Porous Medium and Its Surroundings. Drying Technol. 2005, 23, 455–472.

[15] Defraeye, T.; Blocken, B.; Derome, D.; Nicolai, B.; Carmeliet, J. Convective Heat and Mass Transfer Modelling at Air–Porous Material Interfaces: Overview of Existing Methods and Relevance. Chem. Eng. Sci. 2012, 74, 49–58.

[16] Jambhekar, V. A.; Helmig, R.; Schröder, N.; Shokri, N.Free Flow-Porous-Media Coupling for Evaporation-Driven Transport and Precipitation of Salt. Transp. Porous Med. 2015, 110, 251–280.

[17] Masson, R.; Trenty, L.; Zhang, Y. Coupling Compositional Liquid Gas Darcy and Free Gas Flows at Porous and Free-Flow Domains Interface. J. Comput. Phys. 2016, 321, 708–728.

[18] Xu, Z.; Pillai, K. M. Analyzing Slow Drying in a Porous Medium Placed Adjacent to Laminar Airflow Using a Pore-Network Model. Numer. Heat Transf., Part A Appl. 2016, 70, 1213–1231.

[19] Veran-Tissoires, S.; Prat, M. Evaporation of a Sodium Chloride Solution from a Saturated Porous Medium with Efflorescence Formation. J. Fluid Mech. 2014, 749, 701–749.

[20] Yiotis, A. G.; Tsimpanogiannis, I. N.; Stubos, A. K.; Yortsos, Y. Pore-Network Study of the Characteristic Periods in the Drying of Porous Materials. J Colloid Interface Sci. 2006, 297, 738–748.

[21] Eloukabi, H.; Sghaier, N.; Ben Nasrallah, S.; Prat, M. Experimental Study of the Effect of Sodium Chloride on Drying of Porous Media: The Crusty-Patchy Efflorescence Transition. Int. J. Heat Mass Tr. 2013, 56, 80–93.

[22] Picknett, R. G.; Bexon, R. The Evaporation of Sessile or Pendant Drops in Still Air. J. Colloid Interface Sci. 1977, 61, 336–350.

[23] Hu, H.; Larson, R. G. Evaporation of a Sessile Droplet on a Substrate. J. Phys. Chem. B. 2002, 106, 1334–1344.

[24] Atsuyuki, O.; Boots, B.; Sugihara, K.; Chiu, S. N. Spatial Tessellations: Concepts and Applications of Voronoi Diagrams; 2nd ed. John Wiley & Sons: Chichester, 1999.

[25] Metzger, T.; Tsotsas, E.; Prat, M. Pore Network Models: A Powerful Tool to Study Drying at the Pore Level and Uunderstand the Influence of Structure on Drying Kinetics, In Modern Drying Technology, Computational Tools at Different Scales, Vol. 1, Mujumdar, A., and Tsotsas, E.; Wiley: Brisbane, 2007; pp 57–102

[26] Laurindo, J. B.; Prat, M. Numerical and Experimental Network Study of Evaporation in Capillary Porous Media. Drying Rates. Chem. Eng. Sci. 1998, 53, 2257–2269.

[27] X Lu, E Tsotsas, A Kharaghani, Insights into evaporation from the surface of capillary porous media gained by discrete pore network simulations, International Journal of Heat and Mass Transfer, 168, 120877 (2021).

Appendix

Derivation of Equation (18)

Although the derivation is performed for the 3D case, consider for simplicity the 2D mesh illustrated in Figure 3.14 (viewed as a cross-section of the 3D mesh).

The finite volume discretization of the diffusion equation over this mesh leads to

$$\pi r_p^2 \left(\frac{P_{v1} - P_{vs}}{a/2} \right) + a^2 \left(\frac{P_{v1} - P_{v\infty}}{(n-0.5)a} \right) = 0 \tag{A-1}$$

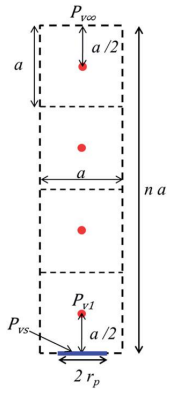

Figure 3.14: Finite volume distribution in the external diffusive mass boundary layer used to obtain Eq. (A-5). The thick blue line materializes the wet pore at the surface. The red dots correspond to the computational points.

Equation (A-1) can be expressed as

$$2\theta(n-0.5)(P_{v1}-P_{vs})+(P_{v1}-P_{v\infty})=0 \tag{A-2}$$

The evaporation rate is expressed as

$$J=\frac{M_v}{RT}D\pi r_p^2\frac{(P_{vs}-P_{v1})}{a/2}. \tag{A-3}$$

Combining Equations (A-3) and (A-2) leads to

$$J=\frac{M_v}{RT}D\frac{2\pi r_p^2}{a}\frac{(P_{vs}-P_{v\infty})}{2\theta(n-0.5)+1} \tag{A-4}$$

Then using Equation (3.2) leads to express J_{ref} here as $J_{ref}=\frac{M_v}{RT}Da^2\frac{(P_{vs}-P_{v\infty})}{na}$. Combining the latter relationship with Equation (A-4) yields

$$\frac{J}{J_{ref}}=\frac{2\theta n}{2\theta(n-0.5)+1} \tag{A-5}$$

which is Equation (3.18) in the main text.

The mesh illustrated in Figure 3.14 is representative of the mesh used for instance in Laurindo and Prat. [26] In other works on drying using PNM, slightly different discretization choices could have been done but most of them use the same discretization step in the external mass transfer layer as in the PNM. Thus, the significant discrepancies between Equations (3.1) and (3.18) in Figure 3.13 are representative of the coarse discretization used in the external mass transfer layer and should be similar whatever the details of the finite difference or finite volume formulation.

Chapter 4

Coupling between internal and external mass transfer during stage 1 evaporation in capillary porous media: interfacial resistance approach

4.1 Introduction

Predicting evaporation from a porous medium is important in many applications such as the evaporation from soils [1] or the drying steps occurring in many industrial processes, e.g [2]. The topic has motivated numerous studies but is still an active research area because predicting the evaporation process is still challenging. The commonly used models actually involve one or more adjustable parameters such as for instance the critical saturation or critical liquid water pressure, a somewhat controversial concept, or the heat and mass transfer coefficients at the porous medium surface [3]. In other words, it has been essentially shown so far that the commonly used models are adjustable. Therefore, they cannot be considered as really predictive. In particular, it is considered that the boundary condition at the evaporative surface is still a somewhat unresolved issue, [3]. By commonly used models, we mean the classical models based on the continuum approach to porous media, [4]. For the simple situation where the temperature variations can be neglected, such a drying model typically takes the form of a non-linear diffusive equation combining the liquid mass balance equation and the vapor mass balance equation in a single equation, [5]. In what follows,

this model is referred to as the local equilibrium (LE) model because it is based on the assumption that the liquid and its vapor are in equilibrium at the scale of the representative elementary volume (REV). However, this widely used model has been criticized [3, 6, 7] and it has been argued that considering a non-local equilibrium (NLE) model was more relevant. The most common approach to evaluate a drying continuum model is through comparisons with experimental data, [3], [8, 9]. However, an alternative is to proceed via comparisons with macroscopic data obtained from pore scale numerical simulations. This latter approach has notably been developed using pore network model (PNM) simulations [7, 10, 13]. Naturally, it is then expected that the PNM simulations are "sufficiently" representative of the drying process for the comparison between the continuum models and the PNM simulations to be also insightful as regards the performance of the continuum models with respect to the experiments. In this respect, it can be noted that the PNM simulations have never been quantitatively compared with experimental data. Naturally, it has been pointed out that the drying PNMs reproduce quite nicely several important experimental features [14, 16] but this remains a qualitative comparison. There are at least two reasons explaining this situation. Most of PNM simulations are performed with structured cubic networks whereas the pore network is unstructured in the experiments. However, a more important problem lies in the size of the networks. Consider for instance the experiments with glass beads reported in [9]. The size of the particles forming the porous medium was on the order of 0.2 mm. The glass bead rectangular container diameter was 15 cm in width and length and 5 cm deep. Thus there was about 250 particles over the container height and 750 over the width or the length. Thus the size of the network should be on the order of 250 x 750 x 750 to be representative of the experiment. The largest network considered so far in drying PNM simulations is 80 x 80 x 80 [15], thus significantly smaller. It must actually be noted that most PNM simulations have been performed with even smaller networks because of computational time and memory size issues. The network should be order of magnitude larger for being representative of many experiments at the laboratory scale, not to mention the field situations. In brief, the networks are much smaller that the size that would be necessary for performing direct comparisons with experimental results. In order to evaluate a continuum model by comparison with PNM simulations, it is thus necessary to evaluate the possible impact of the network size, i.e. the finite size effects, and to develop the comparison so that the latter is not hampered by the finite size effects. This is one of the objectives of the present paper.
Another issue lies in the drying regime and the possible temperature variations for the comparison between experiments, PNM simulations and contin-

uum modelling to be insightful. The regime and the temperate variations, if any, should be comparable. For simplicity, only the situation where the temperature variations are negligible is considered. This situation is referred to as (quasi-) isothermal drying. Various regimes of isothermal drying are identified and discussed in [17] depending on the competition between the capillary forces, the gravity forces and the viscous forces, see also [18]. Although the study of the various regimes is certainly of interest, we focus in the present study on presumably the simpler regime, namely the capillary regime, where the capillary forces are dominant, at least during the first period of drying (referred to as the "constant" rate period (CRP) or stage 1 evaporation). The main features of this regime are presented in section 4.3. Also, the emphasis is on stage 1 because this is a period where the detailed understanding of the coupling between the external transfers and the transfers within the porous media remains challenging.

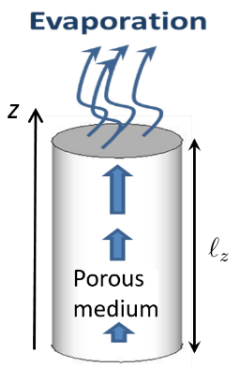

Figure 4.1: Sketch of the archetypical drying situation considered in the study .

As in many previous works, the archetypical drying situation sketched in Figure.4.1 is considered. The porous medium is homogeneous and fully saturated by a volatile liquid initially. Only the top surface of the porous sample is in contact with the ambient air whereas the other limiting surfaces are sealed. This situation is deemed to correspond to a 1D transfer situation as regards the continuum modelling.
As mentioned previously, relying on PNM simulations to analyze the drying process in conjunction or not with continuum models is not a novelty. In [14, 15], the focus was on the analysis of the PNM simulations. No attempt was made to compare the PNM simulations with a continuum model. The focus in [16] was on the impact of liquid films. Here again no comparison with a continuum model was reported. By contrast, we focus in the current paper

on the situation where the effect of the liquid films can be neglected with an emphasis on the continuum modelling of the "PNM drying". Comparisons between a continuum model and PNM simulations are reported in [7] but the emphasis was not on the capillary regime but on the viscous-capillary regime without noticeable stage 1. The parametrization of the mass transfer at the evaporative surface during stage 1 was therefore not addressed. The focus in [10] was on the velocity field induced in the liquid phase by the evaporation and thus different than in the present paper. The special case where the liquid phase is initially distributed in small clusters was considered in [11]. There is no stage 1 in this case either. Comparisons between PNM simulations and a continuum model were presented in [13] but only as regards the saturation profiles. As in [7], the regime was the capillary-viscous regime resulting in a very short stage 1 whereas the focus is on the capillary regime in what follows. Also, the size of the external mass transfer layer was not varied whereas it appears to be an important factor.

The paper is organized as follows: The PNM drying model is summarized in Section 4.2. The main features of the capillary regime are presented in Section 4.3. The saturation profiles are analyzed in Section 4.4. The drying kinetics is discussed in Section 4.5. The non-local equilibrium (NLE) effect is discussed in Section 4.6. The coupling between the internal and external transfers is discussed in Section 4.7. The solution of the continuum model for the considered drying regime is presented in Section 4.8. This is followed by Section 4.9 which proposes a discussion. Section 4.10 consists of the main conclusions of the study.

4.2 Pore network drying model

As in many previous works, e.g. [7, 10, 11, 13, 14, 15, 16], a simple cubic network is considered (Figure.4.2). The distance between two adjacent nodes in the network is the lattice spacing, denoted by a. In this model, the pore bodies located at the nodes of the cubic grid are cubes of size d_p with d_p varying in the range [0.675, 0.725] according to an uniform probability distribution function, noting that the lengths in the PNM are made dimensionless using the lattice spacing a as reference length. The pore throats are channels of square cross section connecting the pore bodies. The throat diameter d_t is distributed in the range [0.075, 0.125] according to an uniform distribution law. The PNM drying algorithm is the one presented in [19]. As discussed in [17], this algorithm applies to the isothermal drying situation where capillary effects are dominant and corner film flows [16, 20] can be neglected.

The interested readers can refer to the afore-mentioned articles for details on the algorithm and additional information on the pore network modelling of the drying process. As sketched in Figure.4.2, the coupling between the internal mass transfer and the external mass transfer is taken into account by setting computational nodes in an external layer of size H. More details on this approach can be found in [19], [15] or [21].

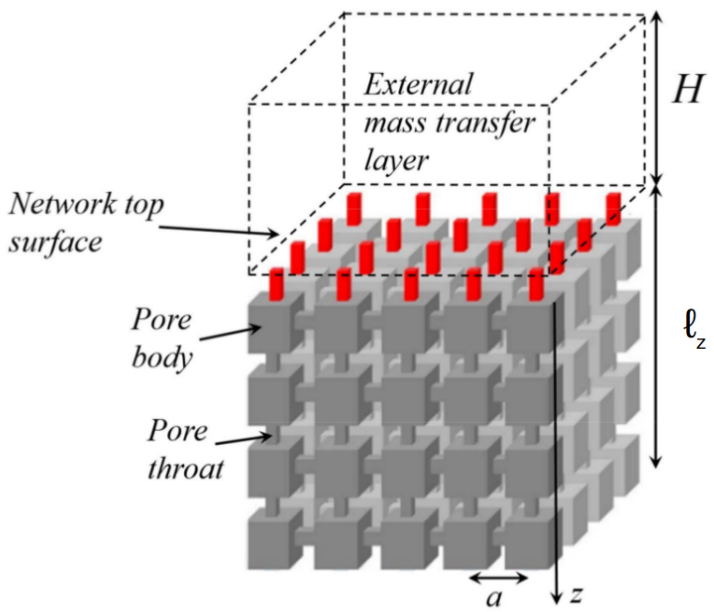

Figure 4.2: Sketch of pore network model with external diffusive layer on top .

As mentioned in the introduction, the capillarity dominant regime is considered, which means that both the effects of gravity and the viscous forces are assumed to be negligible compared to the capillarity. This regime is referred to as the capillary regime. As a matter of fact, the special case when the viscous effects can be neglected compared to the capillary effects even when the main cluster becomes very ramified as the irreducible saturation is approached is considered. For this reason, this regime is referred to as the "asymptotic" capillary regime. Additional details on this regime are given in the next section.

4.3 Comparison between experimental and PNM results

Typical drying experiments aim at measuring i) the cumulative evaporation, i.e. the evaporated mass as a function of time, or equivalently the drying kinetics, i.e. the variation of the evaporation rate as a function of the overall saturation model, ii) the saturation profiles. Figure.4.3 show a few representative results from the literature together with PNM results obtained using the algorithm described in [19]. These results are deemed to be representative of the capillary regime.
As mentioned earlier, several important features are well captured by the PNM approach: drying can be described in two main periods, referred to as stage 1 and stage 2, the saturation profiles are flat during stage 1 whereas a drying zone develops during stage 2 leading to a sharp decrease in the evaporation rate. However, interesting differences are also clearly visible:

1) The experimental saturation profiles are flat in the experiments during stage 1 right from the first measured profiles. Flat profiles are also obtained in the PNM simulations but after a while, i.e. when the overall saturation is significantly lower than in the experiments ($S \sim 0.6 - 0.7$ in Figure.4.3).

2) The PNM profiles are not flat in both edge regions, namely the top and bottom ends of the network. Similar edge effects are not visible in the experimental profiles.

3) During stage 2, the saturation does not decrease in the bottom region in the PNM simulations whereas there is clear decrease in the saturation in the experiment. .

4) The evaporation rate decreases sharply at the beginning of the drying process, i.e. at the beginning of stage 1, in the PNM simulations. This is not seen in the experiments.

The following point can also be noted:

5) The evaporation rate is no necessarily always constant in stage 1 in the experiments. As reported for instance in [9, 23] among others, it can slightly decrease during stage 1.

These various points are discussed in the next sections

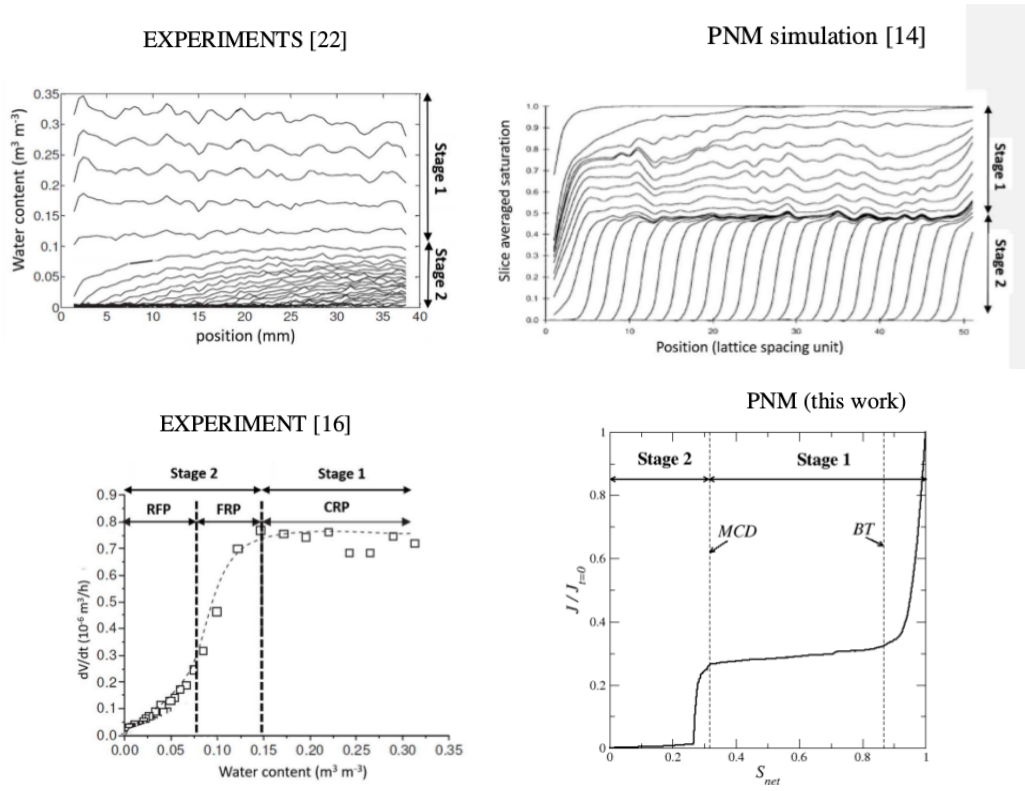

Figure 4.3: Top: comparison between typical experimental and drying PNM saturation profiles in the capillary regime. Bottom: comparison between a typical experimental drying kinetics and a PNM drying kinetics. MCD indicates the main cluster disconnection [14, 15]. BT indicates the breakthrough [14, 15]

4.4 Saturation profiles

The computation of saturation profiles from the PNM simulations requires defining an averaging volume. As in several previous works [7, 11, 13, 14], horizontal slices of thickness a (where a is the lattice spacing) are considered. Each slice contains N x N pore bodies located in a horizontal plane and the half of the vertical throats connecting the pore bodies to the pore bodies in the two adjacent horizontal planes. The thin-slice averaged saturation is thus computed as,

$$S_{thin-slice} = \frac{\sum_{j=1}^{j=n_p} V_{plj} + \sum_{j=1}^{j=n_t} V_{tlj}}{\sum_{j=1}^{j=n_p} V_{pj} + \sum_{j=1}^{j=n_t} V_{tj}} \tag{4.1}$$

where n_p is the number of pores in the slice (n_p = N x N), V_{plj} is the volume of liquid in pore #j, V_{pj} is the volume of pore #j, n_t is the number of throats in the slice, V_{tlj} is the volume of liquid in throat #j within the slice, V_{tj} is the volume of throat #j within the slice.
The thin slice averaged saturation profiles were computed in drying for various size of the external diffusive boundary layer, namely H = 5, 10, 20, 30, 40, 50 (in lattice spacing unit) for a 30 x 30 x 30 network. The profiles were found to be independent of H. On the one hand, this is not surprising since the main cluster invasion is controlled by the distribution of throat sizes (the sequence of throat selection at the boundary of the main cluster is independent of the evaporation rate in the considered capillary regime). On the other hand, it will be seen later in the paper than the smaller the external boundary layer thickness H, the stronger is the NLE effect in the top region of the network. Thus, an impact on the evolution of the isolated clusters forming in this top region could be expected. The simulations thus show that this impact, if any, is indiscernible on the saturation profiles. The thin-slice saturation profiles are depicted in Figure.4.4.
As indicated with point #3, the experimental saturation profiles are flat in the experiments during stage 1 right from the first measured profiles. Flat profiles are also obtained in the PNM simulations but after a while, i.e. when the overall saturation is significantly lower than in the experiments (S $\sim$ 0.6 – 0.7 in Figure.4.4). Physically, non-flat profiles are actually expected in the beginning of drying since the invasion of the porous medium by the gas phase as the result of evaporation starts in the top region of the network. At some point, the gas phase reaches the network bottom. The situation when the gas reaches the bottom for the first time is called the breakthrough (BT). It is well-known from percolation theory [24] and classical works in drainage [25] , that the gas phase cluster at BT is fractal. Therefore, some network size dependence is expected in this initial period and a while after until the saturation becomes uniform over the height of the porous medium. To analyze further this initial period, it can be first noticed that the saturation profiles obtained in drying and in drainage using the classical invasion percolation (IP) algorithm without trapping [26] are very similar. This is illustrated in Figure.4.4 where S_{net} is the overall saturation in the network.

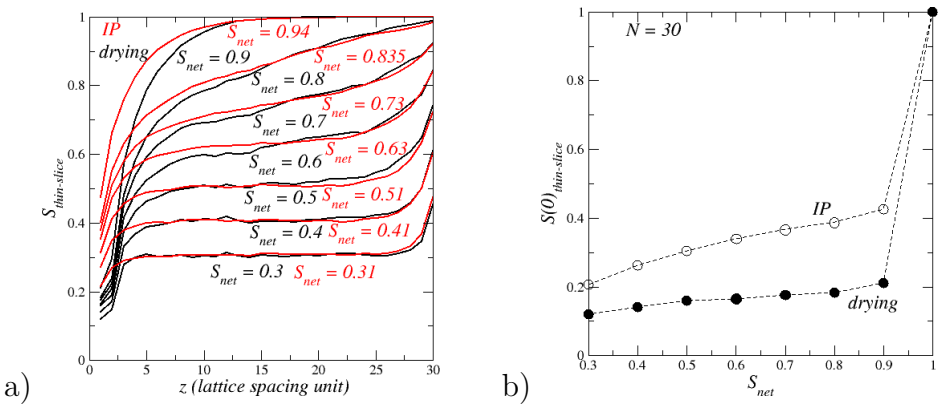

Figure 4.4: a) Saturation profiles in drainage and in drying according to IP algorithm and PNM drying algorithm for a 30 x 30 x 30 network, b) variation of saturation in the top slice in drying and in drainage (IP). S_{net} is the overall saturation in the network.

As the result, the impact of the network size can be more easily studied using the IP algorithm, which is significantly less computationally demanding compared to the drying algorithm. The IP saturation profiles for two network sizes, namely 20 x 20 x 20 and 100 x 100 x 100 are compared in Figure.4.5.

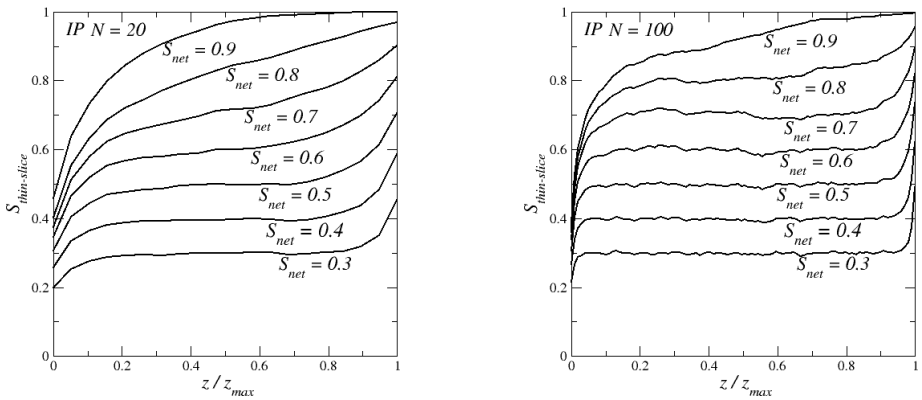

Figure 4.5: IP thin slice averaged saturation profiles for S_{net} = 0.3, 0.4, 05, 0.6, 0.7, 0.8, 0.9 and N = 20 and N = 100.

The comparison between the two network sizes in Figure.4.5 illustrates the network size dependence of the initial period up to BT and a while after. The profile is getting flat (in the bulk) for a greater network saturation in the largest network. The network size dependence at BT is further illustrated in Figure.4.6 with the IP saturation profiles at BT for various network sizes showing that the saturation at BT increases with the network size.

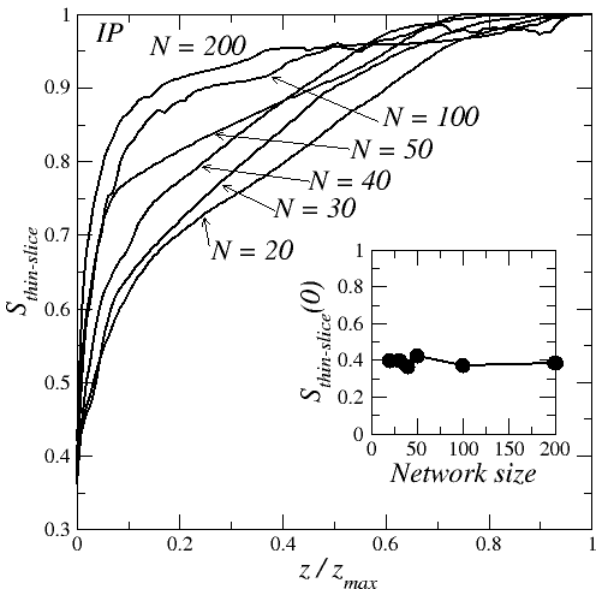

Figure 4.6: IP saturation profiles at breakthrough for various network sizes. The inset shows the saturation at network top in the first slice (z = 0) as a function of network size.

Actually, it is known from percolation theory [24, 26] that the saturation at BT obeys the following scaling law in 3D,

$$1 - S_{BT} \propto N^{-0.48} \tag{4.2}$$

Accordingly, $S_{BT} \sim 1$ for a sufficiently large network. In other words, the initial period around BT cannot be detected in the typical laboratory experiments which correspond to much larger networks than those considered in the simulations because the saturation variation over the BT period is quite small for large networks. This explains why the saturation profiles are typically flat right from the first measured profiles in the experiments (as illustrated in Figure. 4.3). Furthermore, since the commonly used continuum models rely on the concept of length scale separation (a REV can be defined and its size is significantly smaller than the porous medium size, e.g. [4]), the continuum model cannot capture the network size dependence near BT. It follows that the comparison between continuum models and PNM simulations must exclude the initial period around BT. In other words, the comparison should be made for saturations corresponding to a "reasonably" flat profiles in the PNM simulations.

The second striking difference between the experiments and the PNM simulations as regards the saturation profiles lies in the extend of the edge effects. Edge effect refers to the fact that the saturation profiles near the top and

bottom ends of the porous medium during stage 1 are not flat. The saturation is lower than the bulk in the top region whereas this is the opposite in the bottom region where the saturation is greater than in the bulk. In what follows, these edge effects are referred to as the top and bottom edge effects respectively. The edge effects are not really visible in the experimental profiles reported in Figure.4.3 [22] because of significant fluctuations around the mean saturation probably due to porous medium heterogeneities in the sample. The experimental profiles reported in [27] , see Figure.1 in [27] , are much smoother and almost perfectly flat over almost the full sample height. The edge effect on the side of the surface open to ambient air (top edge effect) is quite small, if any. On the side of the closed bottom end, a bottom edge effect is visible in Figure.1 in [27] but the saturation is lower than in the bulk contrary to the PNM simulations. It might be due to some experimental artefact, i.e the fact that the MRI measurements are impacted by the presence of the wall. Another possibility is some looser arrangement of the beads in the vicinity of the bottom wall. Nevertheless, the main observation is that the top edge effect is not visible in the experimental profiles. In other words, the relative extend of the top edge effect region, if any, is less than in the PNM simulations in Figure.4.4. Interestingly both edge effects are also visible in the IP profiles displayed in Figures.4.4 and 4.5 and quite similar to the ones observed in the drying simulations (Figure.4.4). This is an indication that the top edge effect is not primarily due to a stronger evaporation in the network top region in the drying case. Based on the profile evolution displayed in Figure.4.4, the top edge effect can be interpreted as a reminiscence of the very first drying period before and around BT. This initial period is referred to as the BT period. As mentioned before and illustrated in Figure.4.4, there is a preferential invasion of the top region before BT is reached.
Then the question arises as to whether the edge effect is also network size dependent. A first indication is obtained by plotting in the inset in Figure.4.6 the IP slice averaged saturation at the network top at breakthrough as a function of network size. This is the saturation at z = 0 in Figure.4.6. Contrary to the saturation deeper in the network, e.g. at z = 0.2 or z = 0.4 in Figure4.6, this saturation varies very weakly, if any, with the network size. In other words, the top edge effect is present regardless of the network size. A similar conclusion holds as regards the bottom edge effect.
Then, we have plotted in Figure.4.7 the thin slice averaged IP saturation profiles for S_{net} =0.5 for various network sizes.

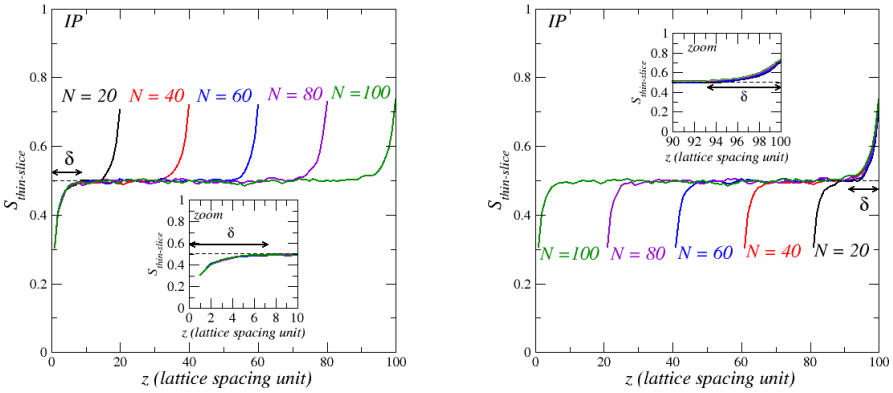

Figure 4.7: Top and bottom edge effect region size. Thin slice averaged IP saturation profile for $S_{net} = 0.5$ for various network size for $S_{net} = 0.5$. The inset in the figure on the left shows a zoom over the top region. The figure on the right shows the overlap of the profiles for the various network sizes in the bottom region. The inset in the figure on the right shows a zoom over the bottom region.

This figure also indicates that the extend of the top and bottom edge effect regions is not network size dependent. An estimate of the extend δ of the edge effect regions can be obtained from the plots in Figure.4.7. As can be seen, $\delta \approx$ 6-7a both at the bottom and at the top. Because of the evaporation at the network top, one can wonder whether this size is also relevant for the drying case. The comparison of the drying and IP saturation profiles in Figure.4.4 does indicate that this is indeed the case. As we shall see, the evaporation is active during stage 1 only in the top edge effect region of size δ. As a result, the saturation is expected to be lower in the drying case in the top edge effect region due to the total or partial evaporation of some isolated clusters in this region but the size of the top edge effect region is actually about the same as in drainage (IP profiles) and in drying.
In summary, the top edge effect, as well as actually the bottom edge effect, is expected to be present regardless of the network size. In the case of our network, its extend is on the order of a few lattice spacing, thus typically smaller than the size of a REV. The top edge effect is a reminiscence of the invasion period before and around BT whereas the bottom edge effect develops after BT until the profiles becomes essentially flat in the bulk. The BT period is indiscernible in most laboratory experiments because of its network size dependence. In a large network, this period actually corresponds to a very small variation of the overall saturation. Although this initial period cannot be detected in most experiments, it does have an impact regardless of the network size. The impact is the formation of transition layer at the very top of the network where the liquid distribution and the transfers (as

we shall see) are different from the bulk. This transition zone is referred to as the top edge effect region in the paper. The extend of this top edge effect region is less than a REV size, on the order of 6-7 lattice spacing in the case of our simulations. The existence of this top edge effect region has been overlooked in the modelling of drying according to the continuum approach to porous media and is, as we shall see, a key element in the analysis of the drying process.
Although the focus in the present paper is on stage 1, it can be noticed in Figure.4.3 that the saturation profiles are different in the experiments and the PNM simulations during stage 2. The saturation does not decrease in the bottom region in the PNM simulations whereas there is clear decrease in the saturation in the experiment. This difference is due to the impact of viscous effects on the pressure field in the liquid, which is completely neglected in the considered PNM drying algorithm (the pressure is spatially uniform in each cluster and dictated by capillary effects only). As the result, the liquid phase is fragmented when stage 2 starts in the PNM simulations, i.e. the saturation is equal to the irreducible saturation. The end of stage 1 then corresponds to the main (or percolating) cluster disconnection (MCD), or more precisely in the case of our PNM simulations to the percolating liquid cluster disappearance. By contrast, the liquid phase still forms a percolating cluster between the sample bottom and the receding front in the experiments but the liquid effective permeability is too low for the liquid to be transported up to the top surface of the sample. As the result, the evaporation front recedes in the sample. One can refer for instance to [23] for a detailed discussion of this mechanism. This effect can be captured by the drying PNM with viscous effects, i.e. [7] and references therein. Since the viscous effects are neglected in the PNM drying considered in the current study, the regime where the liquid phase is completely fragmented (no percolating cluster over the region where the liquid phase is present) is referred to as the "asymptotic" capillary regime. It is expected at very low capillary numbers, that is when the potential evaporation is quite low. Since this asymptotic regime is not typically encountered in the experiments, we focus in what follows on drying up to the end of stage 1. Over this period, the explicit consideration of viscous effects in the PNM is not necessary to develop the comparison between experiments, PNM simulations and continuum modelling in the capillary regime.

4.5 Drying kinetics

The most obvious difference between the drying curve obtained from the PNM simulation and the experimental one in Figure.4.3 lies in the fact that

the evaporation rate decreases sharply at the beginning of the drying process in the PNM simulations. This is not seen in the experiments. In the particular case of the PNM simulation shown in Figure.4.3, it can be seen that the mean evaporation rate in most of stage 1 after the BT period is only about 30% of the potential evaporation, i.e. the evaporation rate when the network is fully saturated at the very beginning of drying. The initial period of sharp decrease in the evaporation rate corresponds to the "breakthrough period" discussed in section 4.4, i.e. the period up to BT and a while after. As discussed in section 4.4, this period is typically not discernable in the commonly performed laboratory experiments since it corresponds to a quite weak mass loss in a large network. However, since it has been argued that a top edge effect region forms on top of the sample during the breakthrough period regardless of the network size, the question arises as to whether the 30% decrease in the evaporation rate compared to the potential evaporation is representative of the experiments. To discuss this point, one starts from some typical values of the evaporation flux in experiments at the beginning of drying. For instance, this evaporation flux is $\sim$ 6.6 x 10^{-4} kg/m^2/s in [22] and $\sim$ 1.4 x 10^{-4} kg/m^2/s in [27] . This flux can be characterized by a diffusion length H from the Fickian relationship,

$$j = D_v \frac{M_v}{RT} \frac{(P_{vs} - P_{v\infty})}{H} \tag{4.3}$$

Where D_v is the vapor molecular diffusion coefficient in air, $P_{v\infty}$ is the vapor partial pressure in the ambience, P_{vs} is the saturated vapor pressure, M_v, R and T represent the molar mass of the volatile species (water typically in many experiments), universal gas constant, and temperature. Applied to the experimental data reported in [22] and [27], one obtains, H $\approx$ 0.7 mm and H $\approx$ 3.3 mm respectively. These values are representative of many other experiments. Hence, H $\sim$ O(1mm). Thus, a first conclusion is that this size is small compared to the size of the sample in the experiments, which is typically on the order of a few cm. On the other hand, the grain / pore size in the experiments is most of the time quite small compared to H. For instance, the mean pore size in [22] is on the order of a few microns. The greater particle size in the experiments reported in [27] is 45 nm. Thus, the experimental situations typically correspond to d « H where d is the pore or particle size. Since the top edge effect region is only a few lattice spacing, i.e. particle sizes, thick, its size δ is typically small compared to the external boundary layer thickness, i.e. δ « H. In the case of the PNM simulation reported in Figure.4.3, the situation is different since H=10a . Thus, H is comparable to the top edge effect region extend $\approx$ 6-7a . In other words, the question arises as to whether the initial sharp drop in the evaporation flux in the PNM

simulation in Figure.4.3 is related to the difference in the ratio H/δ between the experiments, where this ratio is presumably quite large, and the PNM simulation where this ratio is O(1). This question is explored by varying the external mass transfer boundary layer size H in the PNM simulations.

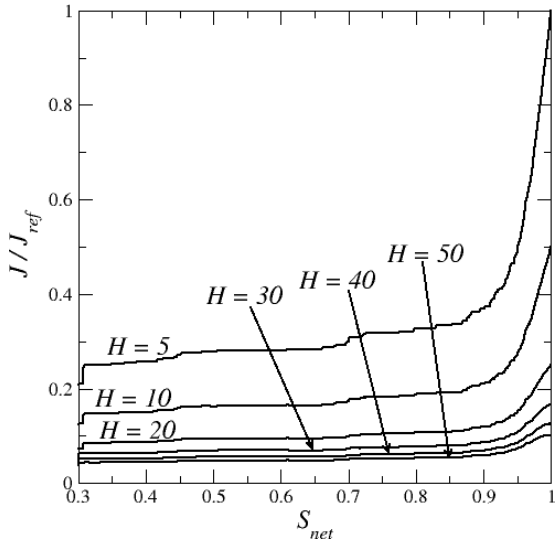

Figure 4.8: PNM simulation drying curve over stage 1 for a 30 x 30 x 30 network for various external mass transfer boundary layer thickness H (measured in lattice spacing unit a). J_{ref} is the evaporation rate at the very beginning of drying for H = 5. S_{net} is the overall saturation in the network.

The results are reported in Figure.4.8. As can be seen, the impact of the initial breakthrough period becomes much less as the external boundary layer thickness is increased. Since H / δ » 1 in the experiments, the results displayed in Figure.4.8 are consistent with the fact that the evaporation flux in stage 1 must be close to the potential evaporation in most experiments. Another interesting feature shown in Figure.4.8 lies in the fact that the evaporation rate is actually not really constant during stage 1 (after the initial BT period). In fact, the evaporation rate decreases smoothly during stage 1. As noted in [15], this is also observed in some experiments, e.g. [9], [23]. The variation of the evaporation rate in stage 1 also depends on the ratio H/d (or equivalently H/δ). The greater this ratio, the smaller is the variation of the evaporation rate during stage 1. As a result, the evaporation rate is practically constant over stage 1 only when H/δ »1, i.e. when the thickness of the external boundary layer is sufficiently large compared to the grain size or the top edge effect region size.

4.6 NLE effect. Tranfer in the top edge effect region

A debated issue, i.e. [3, 6] and references therein, in the drying theory is whether the vapor pressure at the scale of the REV can be considered as sufficiently close to the equilibrium vapor pressure or not. As mentioned in the introduction, the continuum models assuming the local equilibrium at the scale of the REV are referred to as local equilibrium (LE) models whereas the models considering that the vapor pressure at the scale of the REV can be different from the equilibrium vapor pressure are referred to as non - local equilibrium (NLE) models. The most commonly used continuum models, i.e. [4, 8, 9], are LE models.

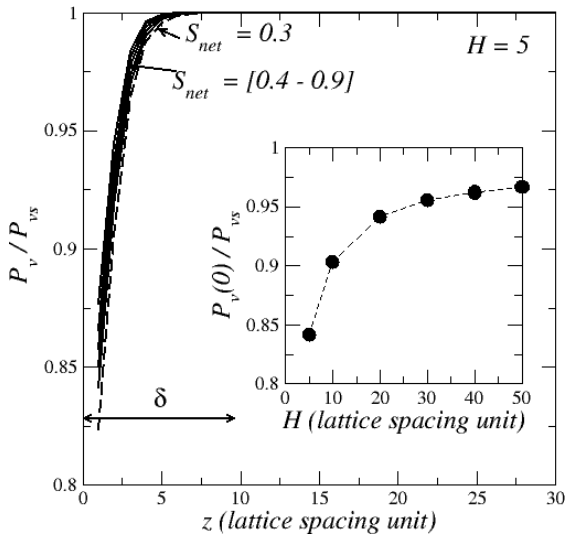

Figure 4.9: thin slice averaged vapor pressure profiles for S_{net} = 0.3, 0.4, 0.5, 0.6, 0.7, 0.8, 0.9 and H = 5. The inset shows the variation of the thin slice averaged vapor pressure on top of network as a function of H for S_{net} = 0.4.

In the LE models, the equilibrium is described via the equilibrium relationships relating the equilibrium vapor pressure and the saturation. The equilibrium vapour pressure is less than the saturated vapor pressure because of a combination of capillary effects (Kelvin effect) and physi-sorption phenomena corresponding to the existence of thin liquid films over the pore wall. The equilibrium relationship is thus generally referred to as the desorption isotherm. However, in the PNM drying, physi-sorption phenomena and the Kelvin effect are not considered on the ground that their impact should be negligible in capillary porous media (an argument is that the drying of a

circular or a square capillary tube can be quite well predicted [29] without considering adsorbed films and/or the Kelvin effect, the latter being non negligible in sub-micronic pores only). In other words, LE equilibrium in the case of the "PNM drying" means that $<P_v> \approx P_{vs}$ if S > 0 where $<P_v>$ is the averaged vapor pressure over a REV. Using as averaging volume the thin slices previously considered, the PNM simulations lead to the slice averaged vapor pressure profiles displayed in Figure.4.9.

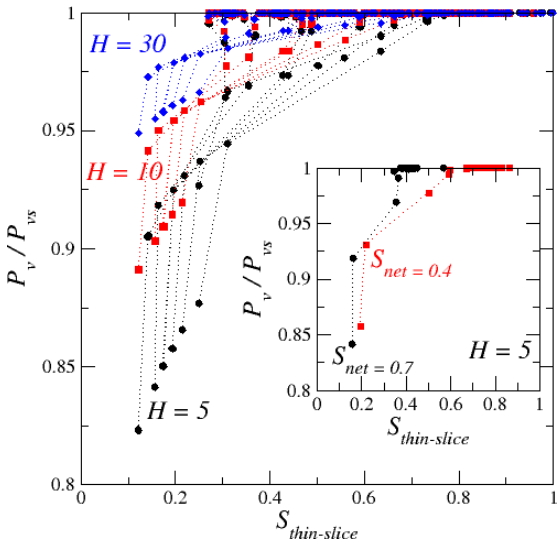

Figure 4.10: NLE signature in the top edge effect region. Variation of the thin slice averaged vapor pressure as a function of the thin slice averaged saturation for various values of S_{net} (in the range 0.3 – 0.7) for various external mass transfer layer thicknesses H. The inset shows the variation of the thin slice averaged vapor pressure as a function of the thin slice averaged saturation for H = 5 and two values of S_{net}.

The figure makes clear that: i) the NLE is noticeable only in the top edge effect region, ii) the greater the external mass transfer layer thickness, the less is the NLE effect in the top edge effect region (as shown in the inset in Figure.4.9). The results shown in Figure.4.9 indicates that the NLE effect in the top edge effect region cannot be represented by a desorption isotherm like relationship. This is better illustrated in Figure.4.10 where the slice averaged vapor pressure is plotted as a function of the corresponding slice averaged saturation for various values of S_{net} and H, i.e. $P_{v-thin-slice}$(z,S_{net},H) as a function of $S_{thin-slice}$(z,S_{net},H) for given values of S_{net} and H.

An obvious consequence of the NLE effect in the network top region is that the average vapor pressure at the network top surface is less than the

saturated vapor pressure during stage 1. However as indicated in Figure.4.9, $P_{v-thin-slice}(0) \rightarrow P_{vs}$ for H » δ. When the interfacial resistance becomes negligible compared to the external mass transfer resistance, then the approximation $P_{v-thin-slice}(0) \approx P_{vs}$ becomes acceptable. These concepts of interfacial and external resistances are discussed in more details in the next section.

4.7 On the transfer coupling at the porous medium surface

Within the framework of the drying models based on the continuum approach to porous, the top boundary condition (TBC) to be imposed is still considered as a somewhat unresolved issue [23]. Three main different approaches to this problem have been considered in the literature. The simpler approach is based on the concept of critical saturation S_{cr} (or equivalently of critical water pressure) [3]. The boundary condition is then expressed as

$$j = j_{pot} \qquad \begin{array}{ll} \text{when} & S(0) > S_{cr} \\ & S(0) = S_{cr} \quad else \end{array} \tag{4.4}$$

Thus, the evaporation flux is equal to the potential evaporation jpot as long as the saturation computed at the surface is greater than S_{cr}. As soon as S(0) = S_{cr}, the boundary condition switches to the constant saturation condition S(0) = S_{cr}. In the case of the PNM simulation, the saturation decreases to zero at the surface during stage 2 (Figure.4.3). Thus, one should take $S_{cr} = 0$. However, the end of stage 1 is observed at a much greater saturation $\sim$ 0.3 and j $\approx j_{pot}$ in stage 1 only when H » δ. Although the critical saturation concept is commonly used, it is also oftentimes debated [3]. In any case, Eq.(4.4) is clearly inappropriate to model the PNM drying. In many studies based on the LE continuum model, e.g. [8, 9] among others, a mass transfer coefficient h_m at the surface is introduced and the boundary condition is typically expressed as

$$j = \frac{h_m M_v}{RT}(P_{vi} - P_{v\infty}) \tag{4.5}$$

where P_{vi} and $P_{v\infty}$ are the vapor pressure at the porous medium surface and in the external gas away from the porous surface, respectively. Expressing the mass transfer coefficient in terms of external flow parameters, such as the Reynolds or Schmidt numbers, is however generally not sufficient to reproduce the experimental data, e.g. [8] . The mass transfer coefficient is actually

fitted assuming that it depends on the saturation at the surface. Actually, since the saturation is the main variable in the LE continuum model, the surface vapor pressure P_{vi} should be also expressed as a function of saturation. The commonly used approach is to assume that the LE relationhip corresponding to the desorption isotherm $\frac{P_v}{P_{vs}} = \phi(S)$ is still valid at the surface. This leads to

$$j = \frac{h_m(S)M_v}{RT}(P_{vs}\phi(S) - P_{v\infty}) \tag{4.6}$$

This boundary is referred to as TBC2. As discussed in previous works [7, 28], this approach is clearly not applicable in the case of the comparison with the PNM simulations since, as discussed before, the fact that the vapor pressure can be lower than the saturated vapor pressure for S > 0 is the signature of a NLE effect and has nothing to do with adsorption phenomena of Kelvin effect. Furthermore, the network top surface is actually the place where the NLE effect is the strongest as illustrated in Figure.4.9. A somewhat naïve idea could be to introduce a pseudo-desorption isotherm or more appropriately a NLE relationship ϕ_{NLE}=$\frac{P_v(S)}{P_{vs}}$ but actually such a simple one to one relationship does not exist since $\frac{P_v(S)}{P_{vs}}$ can take different values for the same value of the local saturation depending on the boundary layer thickness H or the overall saturation as illustrated in Figures.4.9 and 4.10.
An alternative boundary condition (TBC3) used mainly by soil scientists, e.g. [3, 30] and reference therein, consists in expressing the boundary condition at the top surface as

$$j = \frac{M_v}{RT}\frac{(P_{vs} - P_{v\infty})}{r_a + r_{pm}} \tag{4.7}$$

where r_a represents the external boundary layer resistance and r_{pm} is the resistance due to the mass transfer in the porous medium. In this approach, it is assumed that the external boundary layer resistance r_a can be determined only from the consideration of the external transfer at the beginning of the drying process. In other words, this resistance is considered as being independent of the changes occurring in the fluid distribution at the surface during stage 1. By contrast, r_{pm} does depend on the saturation [30] . At first glance, this approach is attractive because of the existence of the top edge effect region in which the NLE effect is present. The mass transfer resistance r_{pm} would be associated with the transfers within the top edge effect region noting furthermore that the vapor partial pressure is indeed very close to P_{vs} at the bottom of the top edge effect region (Figure.4.9). Since the external transfer is purely diffusive in our PNM simulations, r_a can be expressed as

$r_a \approx \frac{H}{D_v}$, where D_v is the molecular diffusion of vapor in the binary mixture (vapor + air). From the PNM simulations, i.e. the computation of the evaporation flux j, r_{pm} can therefore be computed as

$$r_{pm} = \frac{M_v}{RT} \frac{P_{vs} - P_{v\infty}}{j} - r_a \tag{4.8}$$

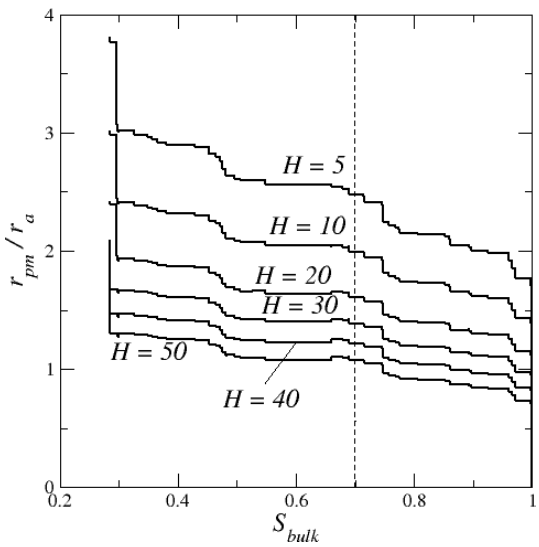

Figure 4.11: Interfacial resistance from Eq.(4.8) as a function of S_{bulk} for various boundary layer thicknesses H.

The variation of r_{pm} over stage 1 for various boundary layer thickness H is depicted in Figure.4.11. The saturation S_{bulk} is representative of the saturation in the bulk of the network away from the edges where the saturation profiles are flat (Figure.4.4). It corresponds to the slice averaged saturation $S_{thin-slice}$ in the middle of the network (at z = 16a).
As can be seen, the interfacial resistance increases along the drying process during stage 1, i.e. increases as the saturation in the medium decreases. This variation is qualitatively in agreement with the parametrization used by soil scientists [30, 31], which reads,

$$r_{pm} = 10e^{0.3563\epsilon(S_r - S_{top})} \tag{4.9}$$

where S_r is the residual saturation and S_{top} is the saturation in the top 1 cm layer of the soil.

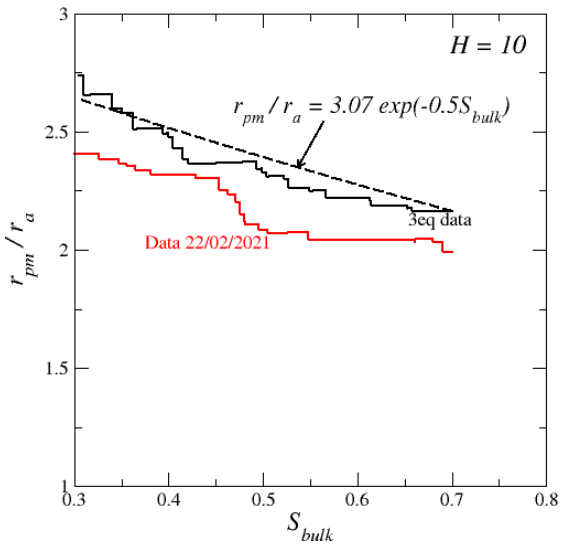

Figure 4.12: Interfacial resistance as a function of S_{bulk}. Test of Eq.(4.9) with modified coefficients. The red curve (data 22/02/2021) corresponds to a single realization whereas the black solid (3eq. data) curve was obtained from data averaged over 15 realizations of the network.

The use of Eq.(4.9) first requires to specify S_r and S_{top}. In the case of our PNM simulations, S_r can either be specified as 0.3 which corresponds to the saturation when the liquid phase ceases to be percolating (MCD) and becomes formed by isolated clusters (this would correspond to the standard definition of the residual saturation) or as 0 since adsorption phenomena are not considered (as exemplified in Figure.4.3, the surface eventually fully dries in the PNM drying).
Both options have been tested. They lead to similar results. Thus, the results obtained considering S_r= 0 are presented in what follows. Then, there is the question of S_{top} . One option could be to consider the average saturation in the top edge effect region, which could play a role similar to the soil top layer. However, the boundary condition expressed by Eq.(4.7) is to be used in conjunction with continuum models. Since the top edge region is quite thin, thinner than the size expected for a REV, we argue that the target of continuum models for the considered capillary regime is to predict the saturation in the bulk and not the rapid saturation variation in the top edge effect region. For this reason, we took $S_{top} = S_{bulk}$. Then the direct application of Eq.(4.9) led to quite poor results. However, if one adjusts the two coefficients in the equation, one obtains the results shown in Figure.4.12, which indicates that the parametrization of the interfacial resistance with an

expression similar to Eq.(4.9) is fair for the considered case, namely H =10,

$$\frac{r_{pm}}{r_a} = 3.07e^{0.5S_{bulk}} \tag{4.10}$$

This is for a given value of the boundary layer thickness. It can be noted that Eq.(4.9) does not depend on the boundary layer thickness H or equivalently on the external mass transfer resistance r_a. This feature is not in agreement with the PNM simulations as illustrated in Figure.4.13a where the computed value of r_{pm} for a given boundary thickness H and a given S_{bulk} are rescaled by the value computed for H = 50 for the same value of S_{bulk}. This figure makes clear that r_{pm} does depend on H. The greater H, the greater is the interfacial resistance. However, as illustrated in Figure.4.11, the relative significance of the interfacial resistance compared to the external mass transfer resistance r_a decreases with an increasing H, consistently with the expected result that the interfacial resistance can be neglected for very large H.

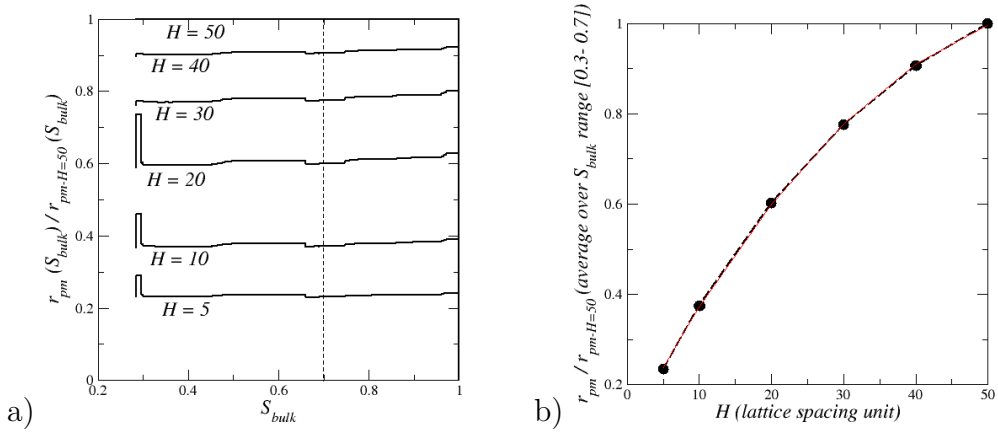

Figure 4.13: a) Interfacial resistance rescaled by its value for H = 50 as a function of S_{bulk}. The vertical dashed line corresponds to the saturation 0.7 below which the saturation profiles are considered as sufficiently flat (see section 4.8); b) Variation of the average value of the interfacial resistance over the bulk saturation range [0.3 – 0.7] as a function of external boundary layer thickness H.

As illustrated in Figure.3.13b, the dependence of r_{pm} with H can be parametrized. Knowing the variation of r_{pm} with S_{bulk} for a given H, i.e. $r_{pm-H_{ref}}$= $r_{a-H_{ref}}$f(S_{bulk}) (Figure.4.12), then $r_{pm(H)}$= $r_{pm-H_{ref}}$g(H). In the example illustrated in Figure.4.13b, g(H) can be represented by a quadratic polynomial. In other words, the interfacial resistance can be expressed according to a relationship based on the separation of the variables H and S_{bulk}. In summary while TBC3 is by far the most satisfactory option, compared

to TBC1 or TBC2, to express the boundary condition for the continuum modelling of the PNM drying, it is not easy to use since it requires a careful characterization of its variation with both the saturation and the external mass transfer resistance. This situation is a consequence of the strong coupling between the transfer in the external boundary layer and in the porous medium top edge effect region.
Although TBC3 appears as the most satisfactory, or perhaps the least bad, approach to model evaporation during stage 1, it can be noted that the interpretation of Eq.(4.7) is not as obvious as it may at first appear. Eq.(4.9) looks like the combination of the steady-state diffusive transfer in the top edge effect region and the external boundary layer. Expressing the evaporation flux as

$$j = D_v \frac{M_v}{RT} \frac{(P_{vi} - P_{v\infty})}{H} \tag{4.11}$$

in the external boundary layer and as

$$j = \epsilon S_{te} D_{eff-te}(S_{te}) \frac{M_v}{RT} \frac{(P_{vs} - P_{vi})}{\delta} \tag{4.12}$$

in the top edge effect region zone (where S_{te} and D_{eff-te} are the average saturation and the effective diffusion coefficient of the vapor in the top edge effect region, respectively) and combining Eq.(4.11) and (4.12) leads to Eq.(4.7) with $r_a \approx \frac{H}{D_v}$ and $r_{pm} \approx \frac{\delta}{\epsilon S_{te} D_{eff-te}}$. This approach to Eq.(4.7) seems in line with the mention that r_{pm} is linked to the transfers within the soil 1 cm top layer in [30, 31]. Then, it would make sense to apply this condition in our case at z = δ (bottom of the top edge effect region) rather than at z = 0. Since very often $\delta \ll \ell_z$ this should actually have no serious significance for the modelling of the numerous situations where the constraint $\delta \ll \ell_z$ is satisfied. However, in the case of the PNM simulations discussed in the current article, the situation is different since $\delta \approx$ 6a is not negligible compared to the height of the network $\ell_z \approx$ 30a. More importantly, there is an inconsistency between the derivation leading to Eq.(4.7) from Eq.(4.11) and (4.12) and the PNM results. The derivation is actually based on the assumption that the evaporation flux j is constant over the top edge effect region. In other words, the evaporation flux at the bottom of the top edge effect region is assumed to be identical to the evaporation flux at the top of the top edge effect region. This is not in agreement with the PNM simulations which shows that the vapor diffusive flux actually vanishes over the top edge effect region, i.e. j_v = 0 at z = δ This is illustrated in Figure.4.14. Therefore, this observation suggests that TBC3 must be applied at z = 0 and not at z = δ.

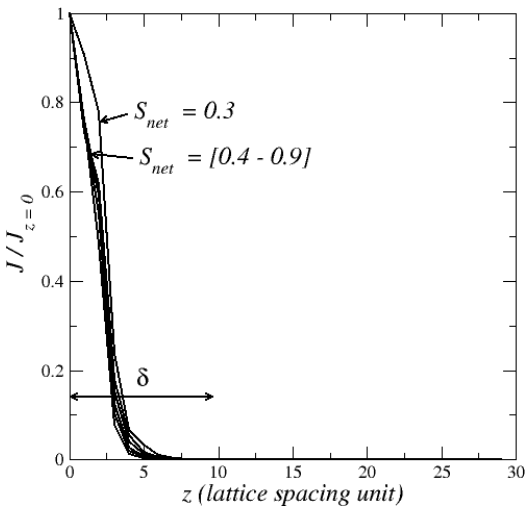

Figure 4.14: Distribution of vapor diffusive flux over the top edge effect region from PNM simulations.

Thus, the interpretation of r_{pm} must be different than simply a vapor diffusion resistance within the top edge effect region. Actually, evaporation takes place within the top edge effect region, i.e. at menisci located within the top edge effect region, as well as at the upper limiting surface of the top edge effect region where a fraction of the pores is filled with the liquid. Thus, the modelling of the evaporation flux with Eq.(4.7) should rather be interpreted as follows in relation with the concept of effective surface, e.g. [32] among others. Within this view of the continuum modelling approach, the layer formed by the top edge effect region is replaced by a fictitious "bulk" layer of same thickness, thus a zone where the internal evaporation is negligible and the saturation is equal to the bulk saturation and thus does not vary spatially over this fictitious layer, at least in the case of the considered capillary regime. The boundary condition TBC3, i.e. Eq.(4.7), is applied on top of the domain formed by the fictitious layer and the remaining porous medium. Thus, in this approach the total height of the porous medium ℓ_z is not modified and is the same as in the experiments (or the pore network in our case). Then, the resistance r_{pm} is interpreted as an interfacial resistance at the porous medium top surface accounting for the complex transfer occurring actually within and at the top of the top edge effect region.
This view of the interfacial resistance r_{pm} is further discussed in the next section.

4.8 Capillary regime continuum model solution

As discussed in previous works, e.g. [11] and references, the NLE continuum model reads (for the 1D situation considered in the current paper),

$$\epsilon\rho_l \frac{\partial S}{\partial t} = \frac{\partial}{\partial z}\left(\rho_l D_l(S)\frac{\partial S}{\partial z}\right) - \dot{m} \tag{4.13}$$

$$\frac{\partial}{\partial z}\left(\epsilon(1-S)D_{eff}\frac{M_v}{RT}\frac{\partial P_v}{\partial z}\right) + \dot{m} = 0 \tag{4.14}$$

Where $D_l(S)$ is the liquid diffusivity, ϵ is the porosity, D_{eff} is the vapor effective diffusivity; $\dot{m}$ is the NLE phase change term, which is expressed as [11],

$$\dot{m} \approx a_{gl}\frac{M_v}{RT}\beta(P_{vs} - P_v) \tag{4.15}$$

where a_{gl} is the specific interfacial area between the liquid and gaseous phases and β is a coefficient, P_{vs} is the saturated vapor pressure.
The saturation is supposed to be spatially uniform initially S = S_0. The boundary conditions at the bottom read

$$-\rho_l D_l(S)\frac{\partial S}{\partial z} = 0 \qquad \text{at} \quad z = \ell_z \tag{4.16}$$

and

$$-\epsilon(1-S)D_{eff}\frac{M_v}{RT}\frac{\partial P_v}{\partial z} = 0 \qquad \text{at} \quad z = \ell_z \tag{4.17}$$

Focusing on stage 1, the boundary condition at the top is expressed using the concept of fictitious effective surface discussed in the previous section by Eq.(4.7), namely,

$$\rho_l D_l(S)\frac{\partial S}{\partial z} = j = \frac{M_v}{RT}\frac{(P_{vs} - P_{v\infty})}{r_a + r_{pm}} \qquad \text{at} \quad z = 0 \tag{4.18}$$

As explained, in the previous section, the NLE effect is confined in the top edge effect region. Elsewhere, $P_v = P_{vs}$. The mass transfer in this region is taken into account via the interfacial resistance r_{pm}. Consistently with the interfacial resistance approach, Eq.(4.17) can be therefore be discarded. The problem to be solved over stage 1 is therefore

$$\epsilon\rho_l \frac{\partial S}{\partial t} = \frac{\partial}{\partial z}\left(\rho_l D_l(S)\frac{\partial S}{\partial z}\right) \tag{4.19}$$

together with Eqs.(4.16) and (4.18). The above problem is expressed in dimensionless form using the height of the sample ℓ_z as characteristic length and the time $\tau = \frac{\ell_z}{j_{i0}/\rho_l}$ as characteristic time, where j_{i0} is the initial evaporation flux (at t = 0 in practice, after the BT period in the case of our PNM simulations). This yields,

$$\epsilon \frac{\partial S}{\partial t^*} = \frac{\tau}{\ell_z^2} \frac{\partial}{\partial z^*} \left(D_l(S) \frac{\partial S}{\partial z^*} \right) \tag{4.20}$$

$$\frac{\partial S}{\partial z^*} = \frac{j \ell_z}{\rho_l} \frac{1}{D_l(S)} \quad \text{at} \quad z^* = 0 \tag{4.21}$$

$$\frac{\partial S}{\partial z^*} = 0 \quad \text{at} \quad z^* = 1 \tag{4.22}$$

First, it can be noted that a solution where the saturation profile is perfectly flat, i.e. $\frac{\partial S}{\partial z^*} = 0$ cannot verify Eqs.(4.20) and (4.21). Thus a solution where $\frac{\partial^2 S}{\partial z^{*2}} = \eta_1$ where η_1 is small, i.e. $\eta_1 \ll 1$, is sought, that is a solution where the saturation profile is almost flat. This gives a saturation profile of the form S= $\frac{1}{2}\eta_1(1 - z^*)^2 + S_0(t)$ since the boundary condition Eq.(4.22) must be satisfied.
Since the spatial variation of is quite weak, Eq.(4.20) can be actually expressed as

$$\epsilon \frac{\partial S}{\partial t^*} = \frac{D_l(S_0(t))}{\ell_z (j_{i0}/\rho_l)} \frac{\partial^2 S}{\partial z^{*2}} \tag{4.23}$$

It can be seen that the expression S= $\frac{1}{2}\eta_1(1-z^*)^2 + S_0(t)$ is indeed a solution to the above considered problem under the approximation $\frac{\partial S_0}{\partial t^*} \gg \frac{1}{2}\ (1 - z^*)^2$ $\frac{\partial \eta_1}{\partial t^*}$. Substituting the proposed solution in Eq.(4.26) yields η_1=-$\frac{j\ell_z}{\rho_l} \frac{1}{D_l(S)}$ Recalling the definition of the liquid diffusivity $D_l(S)$=-$\frac{kk_r}{\mu}\ \frac{dP_c}{dS}$ where k is the permeability, k_r is the liquid phase relative permeability, P_c is the capillary pressure curve and μ is the liquid dynamic viscosity, it can be seen that

$$\eta_1 = \frac{j\ell_z}{\rho_l} \frac{\mu}{kk_r \frac{dP_c}{dS}} \tag{4.24}$$

Introducing a reference capillary pressure P_{cref}=$\frac{2\gamma}{r}$ where r is a representative pore size, Eq.(4.24) is expressed as

$$\eta_1 = \frac{j\ell_z}{\rho_l} \frac{\mu}{P_{cref} kk_r \frac{dP_c^*}{dS}} = \frac{\mu \upsilon_{ev}}{\gamma} \frac{\ell_z r}{2kk_r \frac{dP_c^*}{dS}} = C_a \tag{4.25}$$

Where υ_{ev} is the evaporation velocity (υ_{ev}=j/ρ_l) (Eq.(4.25) makes clear that η_1 is actually a capillary number also taking into account the ratio between

the macroscopic length ℓ_z , which is the relevant length for estimating the viscous pressure drop and the pore size r (it is recalled that k$\propto r^2$,$\frac{r}{k} \propto r^{-1}$) , which is the relevant length for characterizing the capillary pressure. Hence η_1= C_a. This makes clear that the considered solution is valid in the limit of small capillary numbers C_a, that is in the so-called capillary regime. In summary the saturation profile is given by S= $\frac{1}{2}C_a(t)(1-z^*)^2 + S_0(t)$ with $\frac{1}{2}$ C_a $(1-z^*)^2$ « S_0(t) whereas S_0(t) is obtained by solving the equation,

$$\epsilon \frac{\partial S_0(t)}{\partial t^*} = -\frac{j}{j_{i0}} \tag{4.26}$$

Together with the Eq. $j = \frac{M_v}{RT}\frac{(P_{vs}-P_{v\infty})}{r_a+r_{pm}}$ where r_{pm} is a function of S_0(t) . This solution can thus be considered as the asymptotic solution to the continuum model in the limit of sufficiently small capillary numbers (note that C_a varies during stage 1 with the definition of C_a given by Eq.(4.25)).

Futhermore, based on the elements presented in the previous sections, it is first considered that the target of the continuum model must be the period after the BT period for two main reasons: i) the BT period corresponds to the formation of a fractal object, a percolation cluster, which is incompatible with the length scale separation concept underlying the continuum approach to porous media, ii) the BT period is actually indiscernible in most practical situations of interest. Second, since the top edge effect region is expected to be extremely thin compared to the typical total height of porous samples in practice and typically thinner than the size of a REV, the objective of a continuum model should not to capture the rapid saturation variation in the top edge effect region, nor actually in the bottom edge effect region which is also very thin. In other words, the main objective of a continuum model is to predict the (quasi-)uniform distribution of the saturation over the height of the porous sample observed after the very short initial BT period and over most of the sample height in conjunction with the evolution of the evaporation rate. The latter would be obtained from Eq. (4.7) via the adequate parametrization of the interfacial resistance In what follows, we argue that the above continuum model can be tested from comparisons with the PNM simulation results despite the small size of the considered network. To this end, the NLE continuum model, i.e. Eqs.(4.13) and (4.14); is considered also in the edge effect regions (although the model is a priori not really valid ! in these thin region owing to the obvious lack of length scale separation)
Integrating Eq.(4.14) over the top edge effect region leads to,

$$j_v = \int_0^{\delta_t} \dot{m} dz \tag{4.27}$$

Where j_v corresponds to the vapor mass flux from the liquid free pores at the porous medium top surface and δ_t is the size of the top edge effect region. Integrating Eq. (4.13) leads to

$$\epsilon\rho_l \frac{\partial}{\partial t}\left(\int_0^{\delta_t} S dz\right) = -j_l(0) + j_l(\delta_t) - \int_0^{\delta_t} \dot{m} dz \tag{4.28}$$

where $j_l(0)$ is the evaporation flux from the menisci located at the entrance of the liquid filled pores at the porous medium top surface and $j_l(\delta_t)$ is the liquid flow rate per unit surface area in the liquid phase at the bottom of the top edge effect region. Combining Eq.(4.27) and (4.28) and noting that $j_l(0)+ j_v =$ j yield

$$j = j_l(\delta_t) - \epsilon\rho_l \frac{\partial}{\partial t}\left(\int_0^{\delta_t} S dz\right) \tag{4.29}$$

Since evaporation is negligible below the top edge effect region (Figure.4.14), integrating Eq.(4.13) over the "bulk" region and the bottom edge effect region leads to

$$\epsilon\rho_l \frac{\partial}{\partial t}\left(\int_{\delta_t}^{\ell_z-\delta_b} S_{bulk}\ dz\right) + \epsilon\rho_l \frac{\partial}{\partial t}\left(\int_{\ell_z-\delta_b}^{\ell_z} S\ dz\right) = -j_l(\delta_t) \tag{4.30}$$

where δ_b is the size of the bottom edge effect region.
Since S_{bulk} is expected to be spatially uniform in the considered regime, Eq.(4.30) is expressed as

$$\epsilon\rho_l(\ell_z - \delta_t - \delta_b)\frac{\partial S_{bulk}}{\partial t} + \epsilon\rho_l\delta_b \frac{\partial < S >_{bz}}{\partial t} = -j_l(\delta) \tag{4.31}$$

where $< S >_{bz}=\frac{1}{\delta_b}\int_{\ell_l-\delta_b}^{\ell_z} S\ dz$ is the averaged saturation in the bottom edge effect zone.
Eq.(4.29) is then expressed as

$$\epsilon\rho_l\delta_t \frac{\partial < S >_{tz}}{\partial t} = j_l(\delta_t) - j \tag{4.32}$$

where $< S >_{tz}$ is the averaged saturation in the top edge effect zone. Combining Eqs.(4.31) and (4.32) leads to

$$\rho_l\epsilon\left(\ell_z - \delta_t - \delta_b\right)\frac{\partial S_{bulk}}{\partial t} + \epsilon\rho_l\delta_t \frac{\partial < S >_{tz}}{\partial t} + \epsilon\rho_l\delta_b \frac{\partial < S >_{bz}}{\partial t} = -j \tag{4.33}$$

Which is finally expressed as

$$\rho_l \epsilon \left[\ell_z + \delta_t \left(\frac{\partial < S >_{tz}}{\partial S_{bulk}} - 1 \right) + \delta_b \left(\frac{\partial < S >_{bz}}{\partial S_{bulk}} - 1 \right) \right] \frac{\partial S_{bulk}}{\partial t} = -j \quad (4.34)$$

The variations of the mean saturation in the top edge region $< S >_{tz}$ and the mean saturation in the bottom edge effect region $< S >_{bz}$ with S_{bulk} are displayed in Figure.4.15 for the case of the 30 x 30 x 30 network.

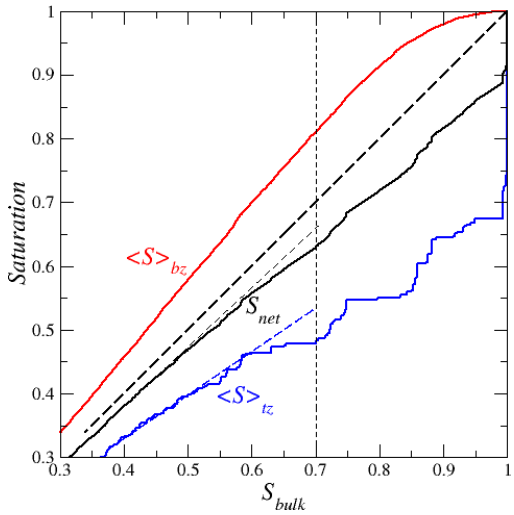

Figure 4.15: Mean saturation $< S >_{tz}$ in the top edge effect region, mean saturation in the bottom edge effect region $< S >_{bz}$ and overall network saturation S_{net} as a function of the saturation in the bulk.

The results for $< S >_{bz}$ has been obtained by IP simulations considering 200 realizations. IP simulations are much faster than drying simulations, which allows obtaining smoother results via the consideration of a greater number of realization. It is recalled that the profiles in drying and in IP are identical in the edge bottom region (Figure.4.4). The results for $< S >_{tz}$ were obtained from drying PNM simulations considering 15 realizations. The focus is on the range of saturations away from the BT period where the saturation profiles are flat in the bulk. We have somewhat approximately considered the bulk saturation range $[0.3 - 0.7]$ although the profile in not yet flat in the bulk for $S_{bulk} \sim 0.7$ so as to consider a not too narrow range of saturations. This corresponds to the range of saturations on the left of the vertical dashed line in Figure.4.15.

As shown in Figure.4.15, $< S >_{tz}$ and $< S >_{bz}$ vary linearly with S_{bulk} in the period of interest with $< S >_{tz} < S_{bulk}$ and $< S >_{bz} > S_{bulk}$. A rough approximation then is to consider that the saturation in excess compared to S_{bulk} in the bottom edge effect compensates the deficit in saturation in the top edge effect region. In other words, referring to Eq. (4.34), this approximation consists in considering that $\delta_t \left(\frac{\partial <S>_{tz}}{\partial S_{bulk}} - 1\right) + \delta_b \left(\frac{\partial <S>_{bz}}{\partial S_{bulk}} - 1\right) \approx 0$. The latter is supported by the fact that S_{net} and S_{bulk} are actually reasonably close over the period of interest as illustrated in Figure.4.15. This finally leads to express Eq.(4.34) as

$$\epsilon \rho_l \ell_z \frac{\partial S_{bulk}}{\partial t} = -j \tag{4.35}$$

which is actually identical to Eq.(4.26), Eq.(4.26) being simply a dimensionless version.
Eq.(4.35) is to be solved in conjunction with Eq.(4.7), namely

$$j = \frac{M_v}{RT} \frac{(P_{vs} - P_{v\infty})}{r_a + r_{pm}} \tag{4.36}$$

With $r_a \approx \frac{H}{D_v}$. Regarding the interfacial resistance r_{pm} two options are compared. The first one consists in using directly the value of r_{pm} (S_{bulk}) deduced from the PNM simulations (black solid line in Figure.3.12) whereas in the second option r_{pm} (S_{bulk}) is computed from the parametrization $r_{pm}(S_{bulk})/r_a$= 3.07 exp(0.5 S_{bulk}) (black dashed line in Figure.4.12). Eq.(4.35) is discretized according to a first order finite difference scheme as S_{bulk}(t+ δ_t) = S_{bulk} - $\frac{j(t)}{\epsilon \rho_l \ell_z}$ where j(t) is computed using Eq.(4.36) where $r_{pm}(S_{bulk})$ is determined as $r_{pm}(S_{bulk}$(t)) using either the parametrization $\frac{r_{pm}(S_{bulk})}{r_a}$= 3.07 exp(0.5.$S_{bulk}$) (option #2) or the value of r_{pm} corresponding to S_{bulk}(t) directly deduced from the PNM simulations (option #1).
As can be seen from Figure.4.16, the agreement between the PNM data and the CM model is quite good. This is not surprising when the interfacial resistance is directly estimated from the PNM data (option #1) because the evaporation flux is of course very well predicted in this case since the interfacial resistance has been determined from the PNM data using Eq.(4.8), i.e. in fact adjusted so that Eq.(4.8) reproduces the evaporation flux. The evaporation flux variation as a function of time is depicted in the inset in Figure.4.16. The result obtained with option #1 is actually indiscernible from the PNM computed evaporation flux (for this reason the latter is not shown in the inset in Figure.4.15). Somewhat surprisingly at first glance since the considered

parametrization seems to be only a crude representation of the interfacial resistance variation in Figure.4.12, using the proposed parametrization of r_{pm}, i.e. option #2, also leads to quite good results as regards the prediction of S_{bulk} as shown in Figure.4.16. The impact of the approximation is clearly more visible on the evaporation flux (inset in Figure.4.16). Nevertheless, it can be considered that these results are quite encouraging. Based on these results, it is tempting to conclude that the interfacial resistance concept, as introduced with Eq.(4.7), is fully adequate to perform the coupling at the surface.

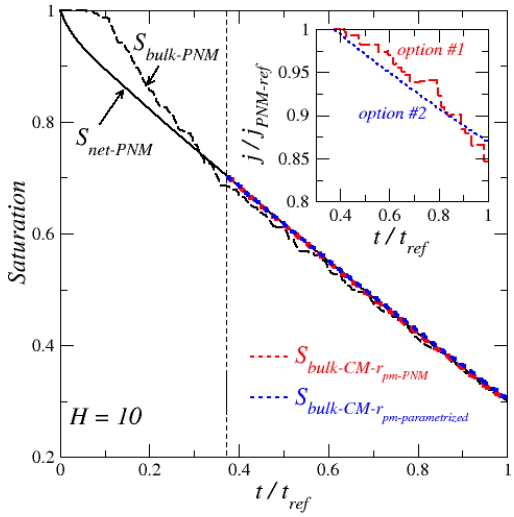

Figure 4.16: Variation of S_{bulk} as a function of time during stage 1. Comparison between the PNM data and the results from the continuum model. The comparison is performed for overal saturations lower than 0.7 (part of the figure on the right side of the vertical dashed line) for the comparison not to be hampered by the initial significant finite size effect associated with the BT period (see text). The reference time is the time at the end of stage 1. The inset shows the variation of the evaporation flux for the two considered options (see text).

However, there is a flaw in the interfacial resistance approach used so far. To be fully consistent, this approach should lead to a fair estimate of the mean vapor pressure at the surface. From Eq.(4.7), the mean vapor pressure at the porous medium could therefore be expected to be given by

$$\frac{P_{vi}}{P_{vs}} = 1 - \frac{j r_{pm}}{P_{vs}} \frac{RT}{M_v} \tag{4.37}$$

The results obtained using Eq.(4.16) are compared in Figure.4.17 with the

spatially averaged vapor partial pressure at the surface computed from the PNM simulations. The latter is computed as

$$< P_{vi} >_{surf} = \frac{\sum_{i=1,n} d_{ti}^2 P_{vi}}{\sum_{i=1,n} d_{ti}^2} \tag{4.38}$$

where n is the total number of pores (opening) at the surface (n = N x N), d_{ti} denotes the size of the interfacial throats connecting the network to the external boundary layer at the network top surface, P_{vi} is the vapor pressure at the entrance of surface throat # i.

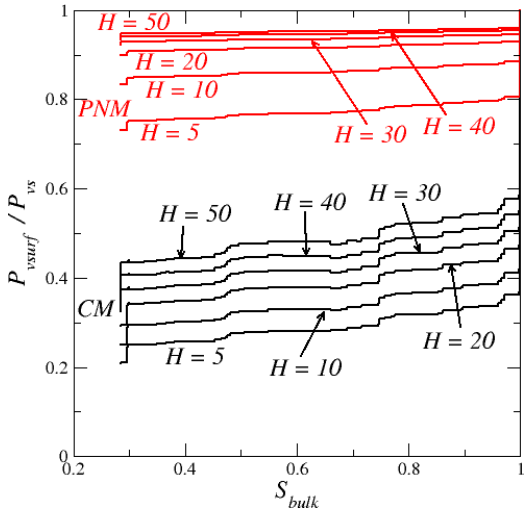

Figure 4.17: Variation of the mean vapor partial pressure at the porous surface P_{vi} as a function of S_{bulk} for various boundary layer thicknesses H with comparison with PNM results. The black curves (CM) are obtained using Eq.(4.37).

As can be seen from Figure.4.17, Eq.(4.37) (which corresponds to the black curves in Figure.4.17) significantly underpredicts the mean vapor pressure at the surface.

The discrepancy is attributed to the fact that the vapor pressure is not spatially uniform at the surface except at the very beginning of the drying process. In other words, P_{vi} in Eq.(4.38) varies from one interfacial throat to the other at the surface with P_{vi}=P_{vs} at the entrance of the interfacial throats filled by liquid and $P_{vi} < P_{vs}$ at the entrance of the gaseous interfacial throats. This spatial variability has been documented in previous works, [14, 28] and is illustrated again in Figure.4.18, which shows the standard deviation of the distribution of P_{vi} at the surface divided by the mean vapour pressure at the surface (Eq.(4.38)), a quantity referred to as the coefficient of variation.

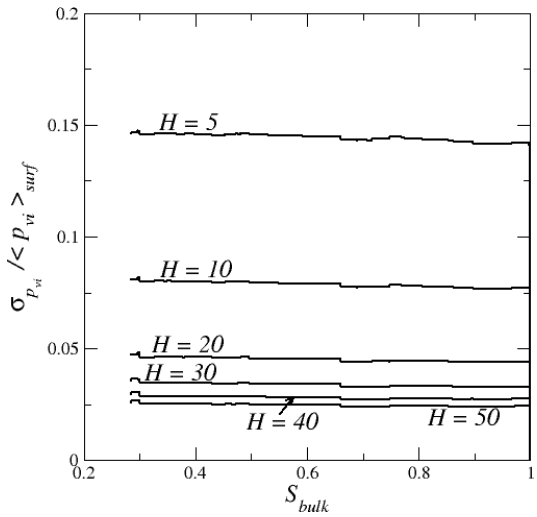

Figure 4.18: Standard deviation of the vapor partial pressure distribution at the surface as a function of S_{bulk} for various mass transfer external layer thicknesses.

As can be seen from Figure.4.18, $\sigma_{P_{vi}}$ first increases rapidly during the BT period (during which $S_{bulk} \sim 1$). Once the top edge effect region is formed, the variation of $\sigma_{P_{vi}}$ is less but it can be seen that $\frac{\sigma_{P_{vi}}}{<P_{vi}>_{surf}}$ increases during stage 1 and can be as high as about 0.15 for the lower mass transfer external layer thickness considered in Figure.4.18. This indicates quite significant variations of P_{vi} over the surface. This necessarily affects the external mass transfer because the structure of the vapor partial pressure field near a surface where the vapor partial pressure is not spatially uniform is different from the structure for a spatially uniform distribution of the vapor pressure at the surface. This means that is erroneous to consider the external mass transfer resistance r_a as constant in Eq.(4.7) for a given H. Thus, we consider Eq.(4.39) where the crucial difference compared to Eq.(4.7) lies in the fact that both r_a and r_{pm} are deemed to depend on S_{bulk} for a given H.

$$j = \frac{M_v}{RT} \frac{(P_{vs} - P_{v\infty})}{r_a + r_{pm}} \tag{4.39}$$

Then, r_a is estimated using the PNM data from the equation,

$$r_a = \frac{M_v}{RT} \frac{(< P_v >_{surf} - P_{v\infty})}{j} \tag{4.40}$$

while r_{pm} is determined from the equation

$$r_{pm} = \frac{M_v}{RT} \frac{(P_{vs} - < P_v >_{surf})}{j} \tag{4.41}$$

This leads to the results reported in Figure.4.19 for both r_a and r_{pm}.

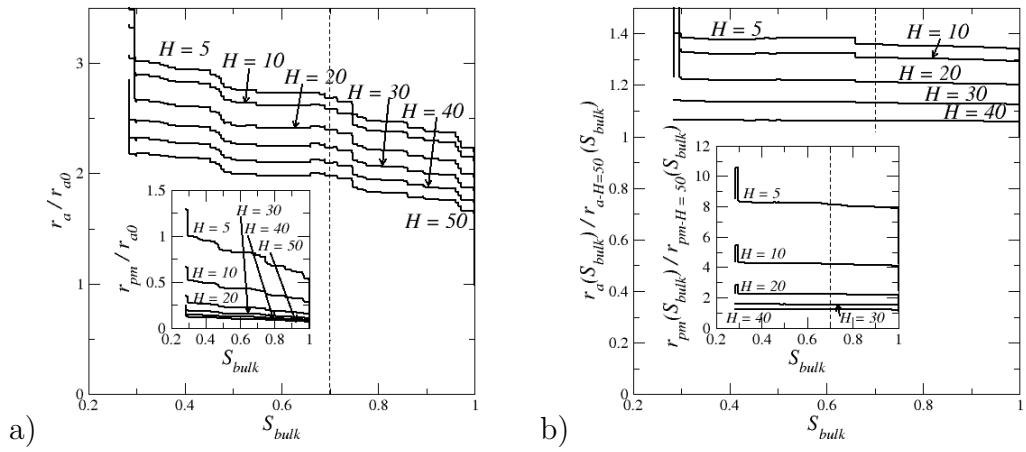

Figure 4.19: a)Variation of the external mass transfer resistance and interfacial resistance (inset) with S_{bulk} for various external mass transfer layer thickness H; r_{a0}= H/D_v is the external mass transfer resistance for the considered value of H at the very beginning of drying when the vapor pressure is spatially uniform at the surface; b) External mass transfer resistance rescaled by its value for H = 50 as a function of Sbulk. The inset shows the interfacial resistance rescaled by its value for H = 50 as a function of Sbulk The vertical dashed lines correspond to $S_{bulk} = 0.7$ considered as the upper bound of the saturation range over which the comparison with the CM should be performed.

As can be seen from Figure.4.19a, both r_a and r_{pm} increases during stage 1. r_{pm} varies roughly linearly with S_{bulk} for a given H (except at the very end of stage 1 when the MCD is approached) whereas expressions such as Eq.(4.10) seems to be reasonable as regards . It can be noted that both r_a and r_{pm} vary with H. Similarly as in section 4.7 (Figure.4.13), the values of r_a and r_{pm} for a given H were divided by the corresponding values for a reference H, here H = 50. The results are depicted in Figure.4.19b. These results suggest a possible variable separation with $r_a(S_{bulk}$,H)= f_{r_a}(H).$r_{a-H_{ref}}(S_{bulk})$ and $r_{pm}(S_{bulk}$,H)= $f_{r_{pm}}$(H).$r_{pm-H_{ref}}(S_{bulk})$, at least over the range of saturation over which the CM can be considered as relevant, i.e. sufficiently away from the BT period.

In summary, the present study suggests that none of the coupling boundary conditions considered in previous works is fully satisfactory. However, the study indicates that expressing the coupling conditions via the concept of interfacial and external resistances can be a satisfactory approach provided that the impact of the evolution of the vapor partial pressure distribution at the surface during stage 1 is adequately taken into account. The most

consistent approach implies to consider that both the interfacial and external resistances vary during stage 1 and not only the interfacial resistance as commonly considered.

4.9 Discussion

Several issues still need clarification as regards the modelling of drying within the framework of the continuum approach to porous media. The present paper proposes a contribution from the consideration of the special case of the PNM drying in the capillary regime. The underlying idea was to test the continuum approach in the case of the drying process obtained via PNM simulations. In the case of the considered PNM drying, the NLE effect, the fact that the vapour pressure in less than the saturated vapor pressure in the presence of liquid, is a major feature, which should not be confused with adsorption or Kelvin effects since these effects are not taken into account in the considered drying PNM. In principle, the consideration of the NLE effects implies to consider a two equation continuum model (CM) as exemplified in [11] for instance. Then the question arises which boundary conditions must be imposed at the porous medium open surface. The boundary condition at the top is indeed presumably much more tricky than for the commonly used one equation model since in principle a boundary condition for each equation, i.e. Eq. (4.18) and (4.19), must be imposed at the medium top surface. If one considers that the evaporation flux at the surface can be separated into a contribution from the dry pores at the surface and a contribution from the wet pores, then the partition of the total evaporation flux into a dry pore contribution and a wet pore contribution should be parametrized [28, 33], noting that information on this partition is typically not available from the usual experimental data. For the particular case considered in the present study, i.e. stage 1 in the capillary regime, this difficulty has been circumvented through the concept of interfacial resistance and the fact that the NLE effect is actually confined in a very thin region on top of the porous medium. In this approach, the two equation CM model reduces to a one equation model. The important difference compared to the commonly used LE CM model is that the remaining equation takes into account the transport in liquid phase only whereas in the usual LE CM model the liquid mass balance equation and the vapor mass balance equation are combined to obtain a single equation. The modelling of transfer in the interfacial region between a porous medium and a free fluid has actually been the subject of many studies, mostly as regards the single phase flow modelling, a problem often referred to as the Beavers and Joseph problem, e.g. [34, 35] and refer-

ences therein. Other transfers have also been studied, e.g. [36, 37] but not, to the best of our knowledge, the drying problem considered in the present paper. Our approach to this problem can be considered as heuristic since we have not mathematically derived Eq.(4.7) but merely postulated it. In this respect, some of the techniques used in the above-mentioned references could help setting Eq.(4.7) on a more firm theoretical basis. Although the concept of interfacial resistance via Eq.(4.7) seems a promising approach as regards the long standing issue of the modelling of the coupling between the transfers in the porous medium and the external transfers in drying, many questions remain open and should be studied further. As noted before, stage 1 ends in practice not primarily because of the fragmentation of the liquid phases in many non-percolating clusters as in our PNM simulations but because of the impact of viscous effects in the liquid phase, thus because of a transition from the capillary regime to the viscous-capillary regime. In this context, it is unclear whether the parametrization of the interfacial resistance r_{pm} and the external resistance r_a determined from the consideration of the capillary regime, i.e. from Eqs.(4.40) and (4.41) in the case of the PNM simulations, still fully applies in the viscous-capillary regime. Also, the modelling of the full drying process is to be clarified, especially at the stage 1 – stage 2 transition. It is tempting to extend the concept of interfacial resistance to the transition zone between the dry zone and the wet zone during the receding front period (RFP) occurring in stage 2 but it can be argued that the size of the NLE zone in the vicinity of the receding front is perhaps not very thin anymore, which could question the applicability of the interfacial resistance concept to the other drying periods. Naturally, it is expected that the consideration of the continuous modelling of the PNM drying is also insightful for the drying process observed in the experiments. In this respect, it has been pointing out that the PNM simulations are consistent with many features observed experimentally. Nevertheless, a recurrent question is the impact of liquid films, [16, 20, 38] that can form during the drying process. The liquid films were not considered in the PNM version used for the present study, which therefore is representative of the situations where the pore geometry and the contact angle are such that liquid films can be ignored. The liquid films can potentially greatly reduce the interfacial resistance if they are present within the top edge effect region since they help maintaining the vapor pressure closer to the saturation vapor pressure in this region compared to the situation in the absence of films [16, 20]. The detailed study of the liquid film impact on the interfacial and external resistances is thus an interesting open question.

4.10 Conclusions

The often debated problem of the modelling of the drying process during the CRP, or stage 1 evaporation drying period, within the framework of the continuum approach to porous media has been studied from comparison with PNM simulations focusing on the (asymptotic) capillary regime in the classical situation of a porous medium column open at the top.

The study first shows that the drying process results in the formation of two edge effect regions, at the top and the bottom. The top edge effect region is of special interest since this region is where the phase change, i.e. the evaporation, takes place. It has been shown that this region is a reminiscence of the breakthrough (BT) period occurring at the very beginning of the drying process. It has been argued that this initial period is very difficult to detect in the experiments because it typically corresponds to a very small mass loss compared to the liquid mass initially present in the porous medium. The size of the edge effect regions has been characterized and has been found to be on the order of a few lattice spacing only, independently of the network size, thus typically less than the size of a REV. Also, it has been shown that the non-local equilibrium (NLE) effect is confined within the top edge effect region.

Since this region is quite thin, it has been argued that the concept of interfacial resistance in which the top edge effect region is represented by a surface of zero thickness (a representation of the interfacial zone referred to as a Gibbs representation) was adapted for describing the coupling between the external mass transfer and the transfer in the porous medium at the top of the porous medium. The interfacial resistance was computed from the PNM simulations and shown to increase along stage 1. For a given external mass transfer resistance, the interfacial resistance can be parametrized using an expression similar to the one used in previous works by soil scientists. However, the numerical factors are different. More importantly, the interfacial resistance was found to depend not only on the saturation but also on the external mass transfer resistance. Also, the interfacial resistance was parametrized using the "bulk" saturation and not the saturation in the top edge effect region on the ground that the continuum model cannot predict the saturation variation in this very thin region. Most importantly, it has been shown that both the interfacial resistance and the external mass transfer resistance must be parametrized as a function of both the bulk saturation and the external boundary layer thickness.

In summary, the main outcome of the present article is to clarify the boundary condition to be specified at the (evaporative) top surface via the concept of effective interfacial resistance. In addition, the present paper clarifies how

to handle the comparison between PNM simulations and continuum models so as to limit the impact on the comparison of the finite size effects inherent in the PNM simulations. In brief, the small size of the networks typically considered in the PNM simulations lead to a BT period much longer than in the experiments. This period cannot be captured by the commonly used continuum models. As a result, the comparison should start a while after the end of the BT period so that the length scale separation concept underlying the continuum approach is verified.

As mentioned before, all this has been developed considering only stage 1 and the so-called asymptotic capillary regime in the absence of noticeable temperature variations. Much work is still needed to explore whether the concept of interfacial resistance is still pertinent beyond the situation considered in the present paper and can be extended to other drying regimes as well as to the modelling of the full drying process.

References

[1] D Or, P Lehmann, E Shahraeeni, N Shokri, Advances in soil evaporation physics—A review, Vadose Zone Journal 12 (4), 1-16 (2013)

[2] A.S.. Mujumdar, Handbook of Industrial Drying (Fourth Edition, CRC Press, 2015).

[3] Z Li, J Vanderborght, KM Smits, Evaluation of model concepts to describe water transport in shallow subsurface soil and across the soil–air interface, Transport in porous media 128 (3), 945-976 (2019)

[4] Whitaker, S., Simultaneous heat, mass, and momentum transfer in porous media: A theory of drying, Adv. Heat Tran., 13, 119-203, (1977)

[5] L.Pel, K.A. Landman and E.F. Kaasschierter, Analytic solution for the non-linear drying problem, Int. J. of Heat and Mass Tr. 45 (15), 3173 (2002)

[6] 6. A. L. Lozano, F. Cherblanc, B. Cousin, J. C. Bénet. Experimental study and modelling of the water phase change kinetics in soils, Eur. J. of Soil Science, 59(5), 939-949 (2008)

[7] Attari Moghaddam, A.; Prat, M.; Tsotsas, E.; Kharaghani, A. Evaporation in capillary porous media at the perfect piston-like invasion limit: Evidence of nonlocal equilibrium effects. Water Resour. Res., 2017, 53 (12), 10433-10449.

[8] Chen P., Pei DCT,A mathematical model of drying processes. International Journal of Heat and Mass Transfer 32, 297-310 (1989).

[9] M. Kaviany, M. Mittal, Funicular state in drying of a porous slab, International Journal of Heat and Mass Transfer, 30 (7), 1407-1418 (1987)

[10] Attari Moghaddam, A.; Kharaghani, A.; Tsotsas, E.; Prat, M. Kinematics in a slowly drying porous medium: Reconciliation of pore network simulations and continuum modeling. Phys. Fluids, 2017, 29 (2), 022102.

[11] F Ahmad, M Talbi, M Prat, E Tsotsas, A Kharaghani, Non-local equilibrium continuum modeling of partially saturated drying porous media: Comparison with pore network simulations, Chemical Engineering Science, 228, 115957 (2020)

[12] F Ahmad, A Rahimi, E Tsotsas, M Prat, A Kharaghani, From microscale to macro-scale modeling of solute transport in drying capillary porous media, International Journal of Heat and Mass Transfer 165, 120722 (2021)

[13] Lu, X.; Kharaghani, A.; Tsotsas, E. Transport parameters of macroscopic continuum model determined from discrete pore network simulations of drying porous media. Chem. Eng. Sci., 2020, 223, 115723.

[14] Le Bray, Y.; Prat, M. Three-dimensional pore network simulation of drying in capillary porous media. Int. J. Heat Mass Transf., 1999, 42 (22), 4207-4224.

[15] AG Yiotis, IN Tsimpanogiannis, AK Stubos, YC Yortsos, Pore-network study of the characteristic periods in the drying of porous materials, Journal of colloid and interface science 297 (2), 738-748 (2006)

[16] AG Yiotis, IN Tsimpanogiannis, AK Stubos, YC Yortsos, Coupling between external and internal mass transfer during drying of a porous medium, Water Resources Research 43, W06403 (2007)

[17] Prat, M. Recent advances in pore-scale models for drying of porous media. Chem. Eng. J., 2002, 86 (1-2), 153-164.,

[18] Lehmann, P., S. Assouline, and D. Or, Characteristic lengths affecting evaporative drying of porous media, Phys. Rev. E, 77, 056309, 2008.

[19] M.Prat. Percolation model of drying under isothermal conditions in porous media. Int. J. of Multiphase Flow. Vol.19,No.4, pp.691-704 (1993)

[20] Prat, M. On the influence of pore shape, contact angle and film flows on drying of capillary porous media, Int. J. Heat Mass Transf., 2007, 50, 1455-1468,

[21] Metzger, T.; Tsotsas, E.; Prat, M. Pore-network models: A powerful tool to study drying at the pore level and understand the influence of structure on drying kinetics. Modern drying

[22] Gupta, S.; Huinink, H. P.; Prat, M.; Pel, L.; Kopinga, K. Paradoxical drying due to salt crystallization, Chem. Eng. Sci., 2014, 109, 204-211

[23] P. Coussot, Scaling approach of the convective drying of a porous medium, Eur. Phys. J. B 15, 557–566 (2000).

[24] D Stauffer, and A. Aharony, Introduction to Percolation Theory, Taylor & Francis, London, (1992).

[25] R Lenormand, C Zarcone, Invasion percolation in an etched network: measurement of a fractal dimension, Phys. Rev. Lett. 54, 2226 (1985)

[26] D. Wilkinson, and J. F. Willemsen, "Invasion percolation: a new form of percolation theory," J. Phys. A: Math. Gen. 16, 3365-3376 (1983).

[27] Thiery, J.; Rodts, S.; Weitz, D. A.; Coussot, P. Drying regimes in homogeneous porous media from macro-to nanoscale. Phys. Rev. Fluids, 2017, 2, 074201.

[28] Attari Moghaddam, A.; Kharaghani, A.; Tsotsas, E.; Prat, M. A pore network study of evaporation from the surface of a drying non-hygroscopic porous medium. AIChE J., 2018, 64 (4), 1435-1447.

[29] F Chauvet, S Cazin, P Duru, M Prat, Use of infrared thermography for the study of evaporation in a square capillary tube, International Journal of Heat and Mass Transfer, 53 (9-10), 1808-1818 (2010)

[30] KM Smits, VV Ngo, A Cihan, T Sakaki, TH Illangasekare, An evaluation of models of bare soil evaporation formulated with different land surface boundary conditions and assumptions, Water Resources Research 48 (12) W12526 (2012)

[31] AA van de Griend, M Owe, Bare soil surface resistance to evaporation by vapor diffusion under semiarid conditions, Water Resources Research, 30 (2), 181-188 (1994)

[32] J.Guo, S.Veran-Tissoires, M.Quintard, Effective surface and boundary conditions for heterogeneous surfaces with mixed boundary conditions, Journal of Computational Physics, 305, 942-963 (2016)

[33] X Lu, E Tsotsas, A Kharaghani, Insights into evaporation from the surface of capillary porous media gained by discrete pore network simulations, International Journal of Heat and Mass Transfer, 168, 120877 (2021).

[34] G.S. Beavers, D.D. Joseph, Boundary conditions at a naturally permeable wall, Journal of Fluid Mechanics, 30(1), 197 - 207 (1967)

[35] M. Chandesris, and D. Jamet, Jump conditions and surface-excess quantities at a fluid/porous interface: a multi-scale approach, Transport Porous Med. 78(3), 419-438 (2009).

[36] F. J.Valdés-Parada, B Goyeau, JA Ochoa-Tapia, Diffusive mass transfer between a microporous medium and an homogeneous fluid: Jump boundary conditions, Chemical Engineering Science, 61(5), 1692-1704 (2006).

[37] JA Ochoa-Tapia, S Whitaker, Heat transfer at the boundary between a porous medium and a homogeneous fluid, International Journal of Heat and Mass Tr., 40(11), 2691-2707 (1997).

[38] A.G. Yiotis, D.Salin, E.S.Tajerand and Y.C. Yortsos, Drying in porous media with gravity-stabilized fronts: Experimental results, Physical Review E 86, 026310 (2012)

Chapter 5

Percolating and non-percolating liquid phase continuum model of drying in capillary porous media. Application to solute transport in the very low Peclet number limit

5.1 Introduction

The drying process in capillary porous media is commonly modelled within the framework of the continuum approach to porous media using a strongly non-linear diffusion equation governing the evolution of the saturation in the medium [1]. As discussed in some details in [2], this conventional approach poses a first problem because it is based on the use of a equilibrium desorption isotherm to relate the vapour pressure and the saturation whereas the impact of adsorption phenomena is presumably negligible in the relatively big pores of capillary porous media (typically defined as porous media with pores greater than about 1 μm in equivalent diameter). As discussed in [2], this questionable aspect can be circumvented by a non local equilibrium (NLE) two equations model whose main variables are the saturation and the vapour pressure. However, this approach, as well as the conventional approach, does not explicitly take into account an important feature

of the drying process, namely the fact that the gradual replacement of the liquid by the gas phase in the pores resulting from the evaporation process leads to the fragmentation of the liquid phase into liquid clusters [3]. As discussed for instance in [3], one can distinguish a first period in the drying process where the liquid phase is distributed between the largest liquid cluster spanning the porous medium and a number of smaller clusters. The largest cluster is referred to as the main cluster whereas the smaller clusters are referred to as the isolated clusters. As shown in [4], this structuration of the liquid phase has an impact on the evolution of the spatial and temporal distribution of a dissolved species during drying. In other words, the question arises as to whether the liquid phase fragmentation process can be taken into account in the continuum approach to porous media so as to develop better models of the transport of a solute during drying. To this end, we present in the current paper a three equation continuum model whose main variables are the vapour pressure, the main cluster saturation and the isolated clusters saturation. Regarding the liquid phase evolution, the three equation continuum model is based on the theory of biphasic flow in porous media presented in [5, 8] proposing to treat microscopically percolating fluid regions differently from microscopically non-percolating regions. With our definitions, the microscopically percolating liquid region corresponds to the main cluster whereas the isolated clusters correspond to the microscopically non-percolating regions. As in a series of previous works [2, 4, 9, 10], the method to discuss the relevance of the continuum model is to proceed via comparisons with simulations with a pore network model (PNM) of drying.
The drying process is commonly described in three main periods [11]: the constant rate period, the falling rate period (FRP) and the receding front period (RFP). As in [4], we mainly focus on the period where the main cluster spans the porous sample, i.e. the CRP. Also, we consider the archetypical macroscopically 1D situation sketched in Figure.5.1 where only the sample top surface is in contact with the external air.
Note that we are interested here in the situations where the evaporation rate is sufficiently low for the temperature variations to be negligible. This situation is frequently encountered in the laboratory experiments with water at the room temperature and referred to as “isothermal” drying.

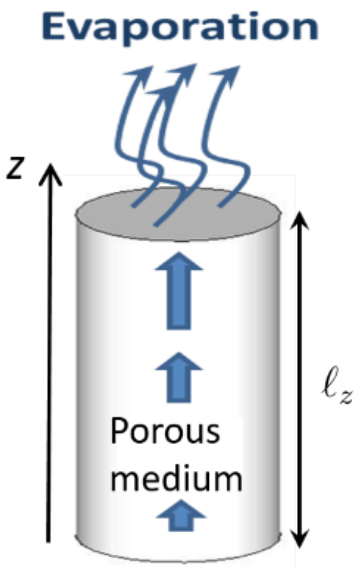

Figure 5.1: Basic drying situation referred to as 1D drying.

The paper is organized as follows: In Section 5.2, the NLE two equation model is briefly recalled and the three equations continuum model is described. The drying PNM is summarized in Section 5.3. Results of PNM simulations are presented in Section 5.4. A comparison between PNM results and the three equation continuum model solution is presented in Section 5.5. The model is extended so as to consider the presence of a solute in Section 5.6 where comparisons between the continuum model and PNM simulations are also presented. This is followed by Section 5.7 which proposes a discussion. Section 5.7 consists of the main conclusions of the study.

5.2 Continuum models

5.2.1 NLE two equation continuum model

The two-equation model is first recalled. As described in [10], the non local equilibrium (NLE) two-equation model can be expressed as

$$\epsilon.\rho\frac{\partial S}{\partial t} + \nabla.(\rho_l \mathbf{U}_l) = -\dot{m} \tag{5.1}$$

$$\nabla.\left(\epsilon.(1-S)D_{eff}\frac{M_v}{R.T}\nabla P_v\right) + \dot{m} = 0 \tag{5.2}$$

where ϵ, t, D_{eff}, S, ρ_l and P_v denote the porosity, time, effective vapor diffusivity, liquid saturation, water density and water vapor partial pressure, respectively. M_v, R and T represent the molar mass of water, universal gas constant, and temperature; $\dot{m}$ is the phase change rate between the liquid and vapor phases. The latter is also referred to as the NLE phase change term. As shown in [10], $\dot{m}$ can be expressed as

$$\dot{m} \approx -a_{gl}\frac{M_v}{R.T}\beta(P_{vs} - P_v) \tag{5.3}$$

where a_{gl} is the specific interfacial area and β is a coefficient, P_{vs} is the saturation vapor pressure since adsorption phenomena are not considered.

5.2.2 Three equation continuum model

The main novelty with the three equation model is to explicitly consider that the liquid phase can be split in the percolating liquid phase, also referred to as the main cluster, and the non-percolating liquid phase. In the three equation model, the liquid saturation is thus expressed as

$$S = S_1 + S_2 \tag{5.4}$$

where subscript 1 is for the percolating liquid phase, i.e. the main cluster, and subscript 2 for the non-percolating liquid phase, i.e. the isolated clusters. Subscript 3 refers to the vapor (the gas phase is a binary gas formed by air and the vapor of the evaporating species). Assuming a homogeneous porous medium, mass balance equations for the percolating and non-percolating liquid phases are expressed as

$$\epsilon\rho\frac{\partial S_1}{\partial t} + \nabla.(\rho_l \mathbf{U}_{l1}) = -\dot{m}_{12} - \dot{m}_{13} \tag{5.5}$$

$$\epsilon\rho_l\frac{\partial S_2}{\partial t} + \nabla(\rho_l.\mathbf{U}_{l2}) = -\dot{m}_{21} - \dot{m}_{23} \tag{5.6}$$

where ϵ is the porous medium porosity, ρ_l is the liquid density, $\mathbf{U}_{l1}$ is the filtration velocity in the percolating liquid phase, $\mathbf{U}_{l2}$ is the filtration velocity in the non-percolating liquid phase, $\dot{m}_{12}$ is the mass transfer rate between phase 1 and phase 2, $\dot{m}_{13}$ is the evaporation rate of phase 1 per unit volume of porous medium, $\dot{m}_{21}$ is the mass transfer rate between phase 2 and phase 1, $\dot{m}_{23}$ is the evaporation rate of phase 2 per unit volume of porous medium. Since a new isolated cluster actually forms as the result of the fragmentation of the main cluster, we also have,

$$\dot{m}_{12} = -\dot{m}_{21} \tag{5.7}$$

It can be noted that in isothermal drying an isolated cluster cannot reconnect to the main cluster, hence $\dot{m}_{12} > 0$. The gas phase forms a single cluster in the drying process. The mass conservation of the vapor is expressed as for the NLE two equation continuum model; i.e. Eq.(5.2),

$$\nabla.\left(\epsilon(1-S)D_{eff}\frac{M_v}{R.T}\nabla P_v\right) + \dot{m} = 0 \tag{5.8}$$

where

$$\dot{m} = \dot{m}_{13} + \dot{m}_{23} \tag{5.9}$$

The phase change rate is expressed as for the NLE two equation continuum model as

$$\dot{m} = a_{lg}\frac{M_v}{R.T}\beta(P_{vs} - P_v) \tag{5.10}$$

with

$$\dot{m}_{13} = a_{l1g}\frac{M_v}{R.T}\beta(P_{vs} - P_v) \tag{5.11}$$

$$\dot{m}_{23} = a_{l2g}\frac{M_v}{R.T}\beta(P_{vs} - P_v) \tag{5.12}$$

Where a_{l1g} (respectively a_{l2g}) is the specific interfacial area between phase 1 (phase 2 respectively) and the gas phase. It can be noted that $a_{lg} = a_{l1g} + a_{l2g}$. Following [8], the mass transfer rate $\dot{m}_{12}$ between the percolating and non-percolating liquid phases is expressed as

$$-\dot{m}_{12} = \eta.\epsilon.\rho_l\left(\frac{S_2 - S_{irr}}{S_{irr} - S}\right)\frac{\partial S}{\partial t} \tag{5.13}$$

where η is a numerical factor. S_{irr} is the irreducible saturation. The above model is simplified by introducing additional assumptions. The flow in the percolating phase is modelled using the generalized Darcy's law,

$$\mathbf{U}_{l1} = -\frac{k.k_{r1}}{\mu}\nabla P_{l1} \tag{5.14}$$

where $\mathbf{U}_{l1}$ is the percolating liquid phase filtration velocity, P_{l1} is the pressure in the percolating liquid phase, k is the medium permeability, k_{r1} is the percolating phase relative permeability, μ is the liquid viscosity. By introducing the capillary pressure curve P_{c1}(S1), where P_{c1}(S1) is the local pressure

difference between the gas phase and the percolating liquid phase, Eq.(5.5) be expressed as

$$\epsilon\rho_l\frac{\partial S_1}{\partial t} + \nabla.\left(\rho_l D_{l1}(S_1)\nabla S_1\right) = -\dot{m}_{12} - \dot{m}_{13} \tag{5.15}$$

where

$$D_{l1}(S_1) = -\frac{k.k_{r1}}{\mu}\frac{dP_{c1}}{dS_1} \tag{5.16}$$

The non-percolating liquid phase is assumed immobile. Eq.(5.6) is thus simplified as

$$\epsilon\rho_l\frac{\partial S_2}{\partial t} = -\dot{m}_{21} - \dot{m}_{23} \tag{5.17}$$

Boundary conditions

For the 1D case sketched in Figure.(5.1), the boundary conditions at the bottom read,

$$-\rho_l.D_{l1}(S_1)\nabla S_1.\mathbf{n} = 0 \tag{5.18}$$

$$-\epsilon(1-S)D_{eff}\frac{M_v}{R.T}\nabla P_v.\mathbf{n} = 0 \tag{5.19}$$

The definition of the boundary conditions at the top surface is still an open question in the drying theory [10, 12, 13]. In other words, the coupling at the surface between the transport phenomena in the porous medium and in the external air in contact with the porous medium surface is still not sufficiently well understood and modelled. In the case of the three equation continuum model, the detailed modelling of the mass transfer at the top surface is particularly challenging since one has to consider that the vapor leaves the porous medium surface from three categories of pores: i) by evaporation from pores belonging to the main cluster (percolating liquid phase), ii) by evaporation from pores belonging to isolated clusters connected to the surface (non-percolating liquid phase), iii) gaseous pores. However, this challenging modelling issue is left for a future work. In the present study, the focus is on the modelling of the liquid phase internal fragmentation. A simplified approach is therefore adopted. As explained in more details later in the paper, this simplified approach essentially consists in assuming that the overall evaporation rate is an input data for the model and not an outcome.

5.3 Pore network model

As in [3], a simple cubic network is considered (Figure 5.2). The distance between two adjacent nodes in the network is the lattice spacing, denoted

by a. In this model, the pore bodies located at the nodes of the cubic grid are cubes of size d_p with d_p varying in the range [0.675, 0.725] according to an uniform probability distribution function, noting that the lengths in the PNM are made dimensionless using the lattice spacing a as reference length.

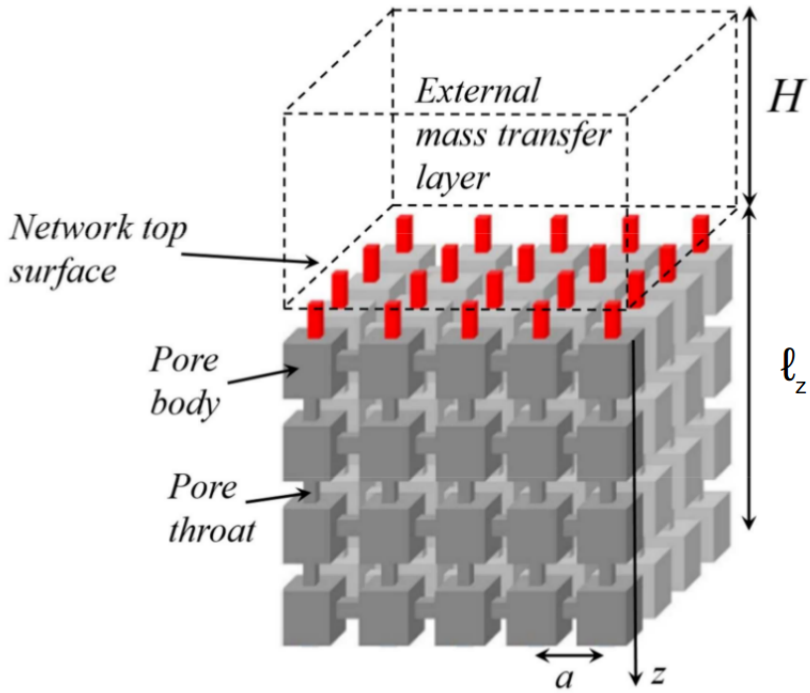

Figure 5.2: Sketch of pore network model with external diffusive layer on top.

The pore throats are square face beams connecting the pore bodies. The throat diameter d_t is distributed in the range [0.075, 0.125] according to an uniform distribution law. The drying algorithm is the one presented in [14]. As discussed in [15, 16] or [17] this algorithm applies to the isothermal drying situation where capillary effects are dominant and corner film flows [18, 19] can be neglected.
The interested readers can refer to the aforementioned articles for details on the algorithm and additional information on the pore network modelling of the drying process. It must be recalled that the viscous effects are not explicitly considered in the liquid phase in the version of the algorithm considered in the present paper. As discussed in [15], various drying regimes can be actually distinguished depending on the competition between the capillary

forces, the gravity and the viscous forces. Here, the capillarity dominant regime is considered since both the effects of gravity and the viscous forces are assumed to be negligible compared to the capillarity.
This regime is referred to as the capillary regime. As a matter of fact, the special case when the viscous effects can be neglected compared to the capillary effects even when the main cluster becomes very ramified as the irreducible saturation is approached is considered.
For this reason, this regime is referred to as the "asymptotic" capillary regime. Additional details on this regime are given later in the paper.

5.4 Pore network simulations

PNM simulations of the drying process were performed with a N x N x N cubic network, where N is the number of nodes in the network along each direction of a 3D Cartesian coordinate system (N = 4 for the network sketched in Figure.5.2). The results presented in what follows were obtained for N = 30. The external boundary layer thickness (Figure.5.2) was 10.

Figure.5.3-a) shows the variation of the computed evaporation rate (normalized by the evaporation rate at t =0) as a function of S_{net}, i.e. the overall network liquid saturation. Note that these data as well as the other PNM data presented in the paper are averages over 15 realizations of the network unless otherwise mentioned.
The classical evolution [11] is retrieved with a relatively long period, for S_{net} varying about between 0.8 and 0.31, where the evaporation rate varies weakly. This period is referred to as the "constant" rate period (CRP). As can be seen in Figure.5.3-a), the CRP ends when S_{net} is about equal to 0.31, which corresponds to the vertical dashed line in Figure.5.3-a) Then the evaporation rate drops.

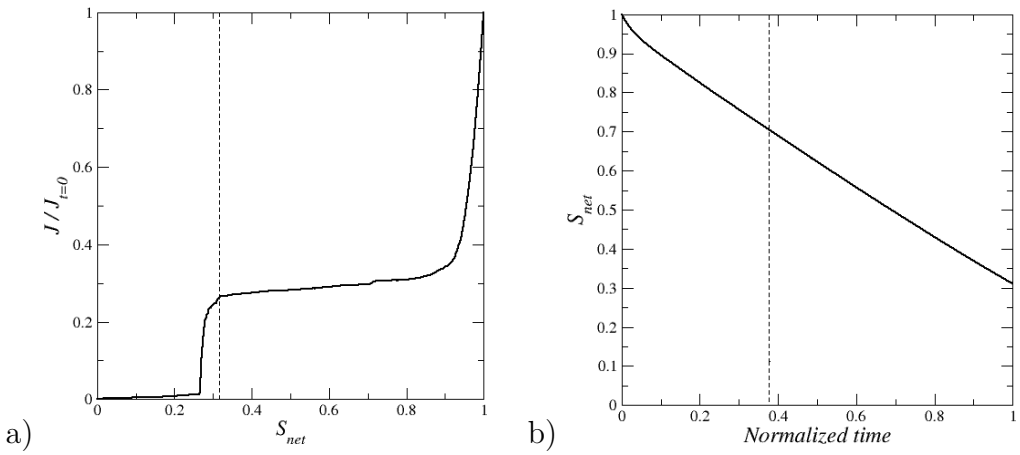

Figure 5.3: Evolution of : a) evaporation rate (drying curve); the vertical dashed line indicates the end of the "CRP", b) the overall network liquid saturation S_{net} in the range [0.31 -1], the reference time is the time when $S_{net} = 0.31$,which about corresponds to the end of the CRP, the vertical line corresponds to $S_{net} = 0.7$, which is the maximum saturation considered for comparison with the continuum model (see text).

This corresponds to the falling rate (FRP) and receding front period (RFP). However, contrary to the classical experimental results [11], an initial period where the evaporation rate drops can be observed before the quasi constant rate period starts (this approximately corresponds to Snet in the range [0.9 – 1] in Figure.5.3-a). This period is discussed below with the results on the saturation profiles. Figure.5.3-b shows the evolution of S_{net} as a function of time. The reference time is the time when $S_{net} = 0.31$ ($t_{ref} = t_{S_{net}=0.31}$). Since the focus in what follows is on the CRP the evolution of S_{net} in Figure.5.3-b) is shown down to $S_{net} = 0.31$, which approximately corresponds to the end of the CRP. Consistently with the variation of the evaporation rate in Figure.5.3-a), the evolution of S_{net} shows a first period where S_{net} decreases faster compared with the longer period that follows where the slope of the curve in Figure.5.3-b) is smaller and varies weakly. Figure.5.4 illustrates the liquid phase fragmentation process occurring during the drying process. As can be seen, the number of liquid clusters increases during the CRP. The liquid phase is actually formed during this period by a main or percolating cluster and an increasing number of isolated or non-percolating clusters.

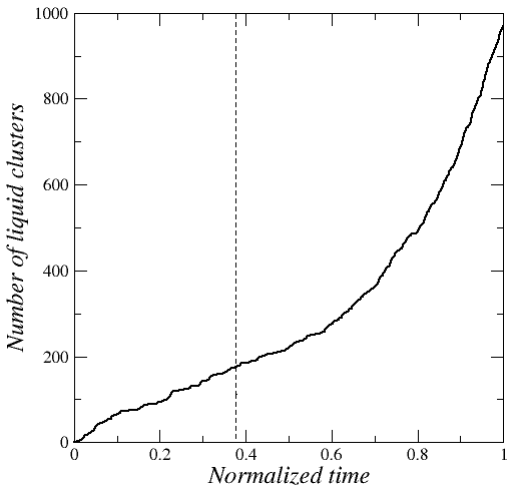

Figure 5.4: Number of liquid clusters in the network as a function of time up to the end of the CRP. The vertical line corresponds to Snet = 0.7.

Saturation profiles during the drying process up to the end of the CRP are depicted in Figure.5.5.
These profiles are horizontal slice averaged profiles according to a procedure similar to the one used in previous works [2, 9, 10]. The slices are 10 lattice spacing thick in the present work. This choice is motivated by the fact that the computations of macroscopic parameters from PNM simulations, such as for instance the local porosity as illustrated in Figure.5.6, indicate that an averaging volume of size 10a can be considered as a reasonable Representative Elementary Volume (REV). Thus a running averaging procedure is used considering slices of size N x N x 10 . The computed values are affected to the center of the slices. It can be also noted that slice saturations are actually typically considered in the experiments [20, 21]. The selected slice thickness explains why the profiles start at z = 5 (in lattice spacing unit) and ends at z = 25 in Figure.5.5. The slice averaged saturations are denoted by S_{sl}, S_{1sl} and S_{2sl} respectively.

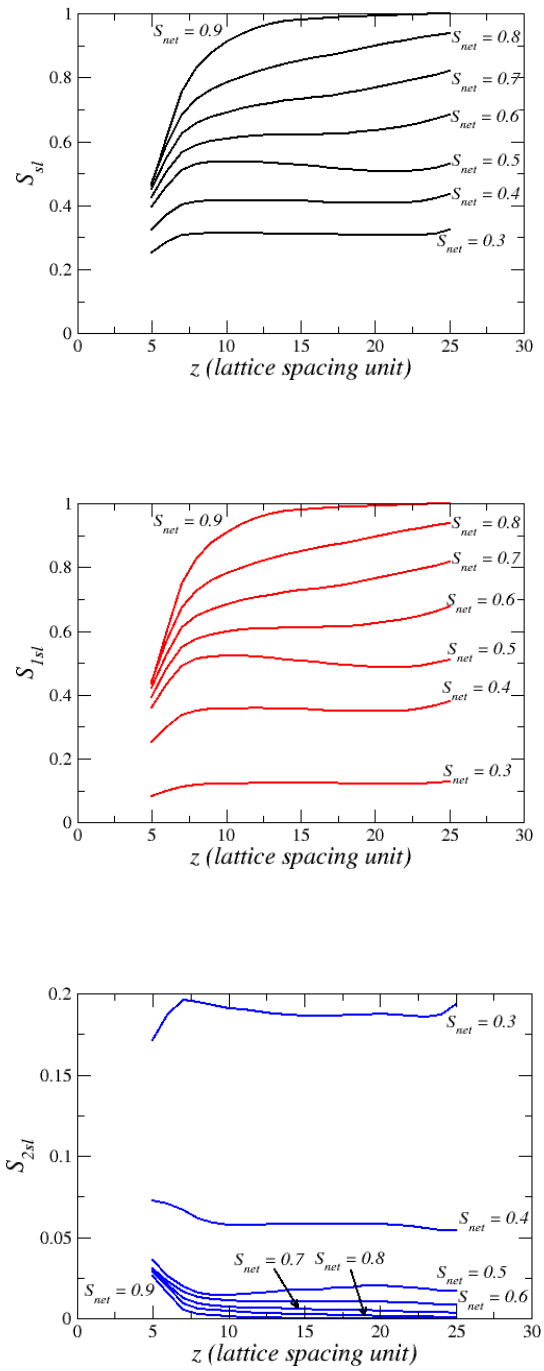

Figure 5.5: Liquid phase saturation profiles (S_{sl}), percolating liquid phase (S_{1sl}) and non-percolating liquid phase (S_{2sl}) saturation profiles (corresponding to S_{net} = 0.9, 0.8, 0.7, 0.6, 0.5, 0.4, 0.3); z = 0 corresponds to the network top surface (Figure.5.2) whereas z = 30 to the network bottom limiting surface

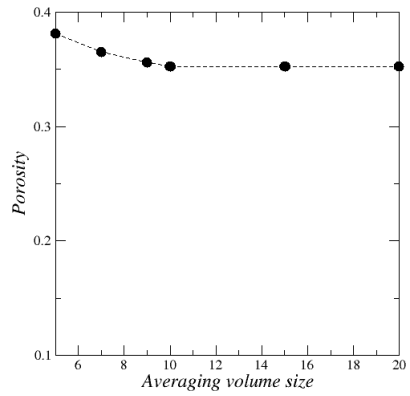

Figure 5.6: Variation of the porosity as a function of averaging volume size obtained by computing the porosity over a cubic volume of increasing size located within the network

The liquid phase saturation profiles in Figure.5.5 present several differences compared to the profiles typically obtained in the experiments. For the capillary regime considered in the present paper, the latter are typically flat, e.g. [20, 21]. By contrast, edge effects are noticeable at both ends of each profile in Figure.5.5. The profiles are flat only in the region away from the edges. Also, they become flat in this region only when S_{net} is sufficiently low, i.e. when $S_{net} \sim 0.6$ - 0.7. These differences with the experimental profiles are discussed in details in [22]. The initial period where the profiles are not flat in the central region is associated with a finite size effect and corresponds to the period where S_{net} varies from 1 to S_{BT}, where S_{BT} is the saturation at breakthrough. Since the saturation at breakthrough, i.e. when the gas phase reaches for the first time the network bottom scales as $1 - N^{\alpha}$ where $\alpha = 0.48$ in 3D according to the percolation theory [23], this initial period becomes negligible for a sufficiently large network, and thus cannot be seen typically in the experiments. By contrast, the edge effect size is found to be independent of the network size and on the order of a few lattice spacing [22]. As a result, the corresponding variations of the saturation in the edge regions is difficult to detect in the experiments since the size of the edge effect regions is typically very small compared to the sample size in the experiments. For these reasons, we believe that the main objective of continuum models as regards the saturation profiles should be to predict the flat profile evolutions since the finite size effect impacted period is negligible in most experiments as well as the extension of the edge effect regions. For the sake of comparison with the continuum model, we therefore consider as main targets S_{bulk}, S_{1bulk} and S_{2bulk} where S_{bulk}, S_{1bulk} and S_{2bulk} are the values of S_{sl}, S_{1sl} and S_{2sl} in the middle of the network, i.e. at z =16 in Figure.5.5. The variations of

S_{bulk}, S_{1bulk} and S_{2bulk} are depicted in Figure.5.7.

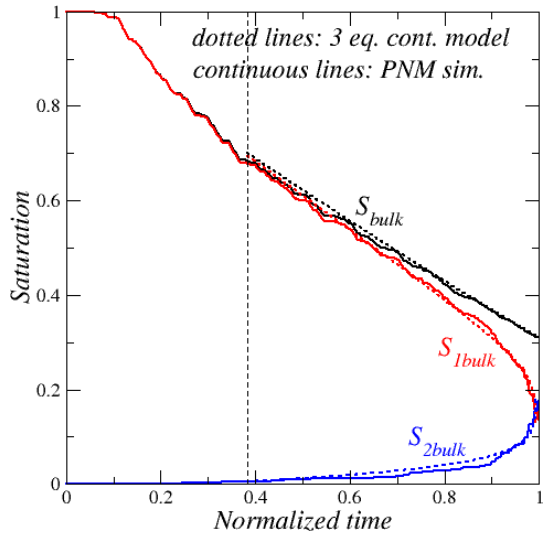

Figure 5.7: Variation of S_{bulk}, S_{1bulk} and S_{2bulk} as a function of time during the CRP. Comparison between the PNM data and the results from the three equation continuum model. The comparison is performed for overall saturations lower than 0.7 for the comparison to be not hampered by the initial significant finite size effect (see text). The overall saturation 0.7 corresponds to the vertical dashed line in the figure.

The variations are shown over the period corresponding to Snet in the range [0.3, 0.7] which is defined as the period of interest. From the above data, the period of interest in what follows is defined as the period of the CRP not affected by the finite size effect. It approximately corresponds to the range of overall saturation [0.3-0.7]. As illustrated in Figure.5.5, the saturation profiles in the bulk are reasonably flat for $S_{net} < 0.7$. As can be seen, the percolating phase saturation decreases over the CRP whereas the non-percolating liquid phase saturation increases. The variations of both saturation is much faster and more important as the end of the CRP is approached. As discussed in [3], the end of the CRP corresponds to the situation when the percolating liquid phase is about to cease percolating. In the considered asymptotic capillary regime, this corresponds to when the irreducible saturation is about to be reached. From Figure.5.3-a), it can therefore be considered that $S_{irr} \approx 0.31$.

5.5 Continuum model solution

In order to solve the three equation continuum model, Eqs.(5.4-5.17), the following parameters must be in principle determined: ϵ, $D_{eff}(S)$, a_{l1g}, a_{l2g}, β, η, S_{irr}, k, k_{r1}, $P_{c1}(S_1)$ nothing that the parameters D_{eff}, a_{l1g}, a_{l2g}, k_{r1}, P_{c1} are non-linear functions of the saturation. As exemplified in [2, 10, 24], these parameters can be determined from PNM simulations. Also, because of the non-linearity, Eqs.(5.4-5.17) must generally be solved using a numerical method. However, it can be observed from Figure.5.5 that the profiles are spatially uniform (when as discussed before the edge effects are not taken into consideration and the initial period affected by the finite size effect is discarded). Under these circumstances, the numerical solution can be greatly simplified and the determination of most of the three equation continuum model parameters from specific PNM numerical simulations can be avoided. Integrating Eq.(5.15) over the porous medium height ℓ_z using the z-coordinate depicted in Figure.5.1 leads to

$$\epsilon\rho_l\ell_z.\frac{\partial S_1}{\partial t} = -j_{per} - \int_0^{\ell z} \dot{m}_{12}\ dz - \int_0^{\ell_z} \dot{m}_{13}\ dz \tag{5.20}$$

Where j_{per} is the evaporation flux of the percolating liquid phase at the porous medium top surface. A further simplification is to neglect the phase change, i.e. the evaporation inside the porous medium in the bulk region. This assumption is supported by the results shown in Figure.5.8 showing that the evaporation essentially takes place in the top region of the network over the considered period.

Then it is argued that the evolution of the main cluster results from the evaporation flux at the surface j_{per} , from the fragmentation in the bulk region but also from the fragmentation occurring in the top region of the network. Then it is assumed that the latter approximately corresponds to the evaporation from the isolated clusters in the top region of the network. This is simply taken into account by considering that the effective evaporation flux of the percolating liquid phase to be considered is j, i.e. to the total evaporation flux, and not j_{per}.

An additional simplification with the consideration of the bulk region only lies in the fact there is no need to consider the vapor mass conservation equation (5.8) because the NLE effect is actually noticeable only in the top region of the network during the CRP [22], which, as illustrated in Figure.5.8, is the evaporation active region.

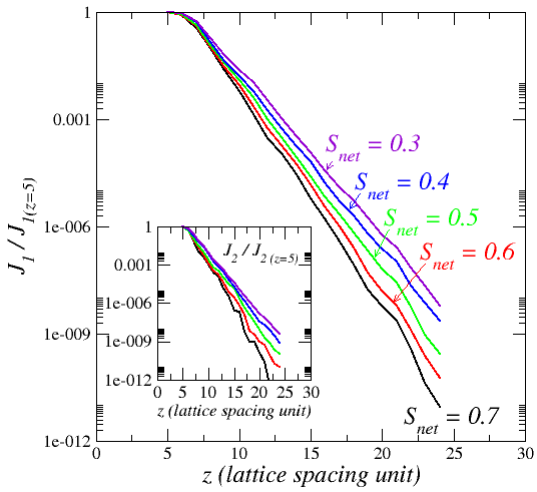

Figure 5.8: Variation of evaporation rate from percolating cluster (J_1) and non-percolating clusters (J_2) in the slices as a function of z for various network saturations (the colours in the inset corresponds to the same overall saturations as in the main figure).

Deeper in the network, and thus in the bulk region, $P_v \approx P_{vs}$. All this finally leads to express Eq.(5.20) as,

$$\epsilon\rho_l\ell_z\frac{\partial S_{1bulk}}{\partial t} \approx -j - \int_0^{\ell_z} \dot{m}_{12}\, dz \tag{5.21}$$

Since S_1 and S_2 are approximately uniform in the bulk, it can be inferred from Eq.(5.13) that $\dot{m}_{12}$ is also uniform in the bulk. Eq.(5.21) is thus expressed as,

$$\epsilon\rho_l\frac{\partial S_{1bulk}}{\partial t} \approx -\frac{j}{\ell_z} - \dot{m}_{12} \tag{5.22}$$

In the bulk, S_2 is also approximately uniform and the internal evaporation is negligible. Thus, Eq.(5.17) is expressed everywhere in the bulk as,

$$\epsilon\rho_l\frac{\partial S_{2bulk}}{\partial t} = -\dot{m}_{21} \tag{5.23}$$

Where, as mentioned before, it is proposed to express $\dot{m}_{12}$ as in [6],

$$-\dot{m}_{12} = \eta\epsilon\rho_l\left(\frac{S_{2bulk} - S_{irr}}{S_{irr} - S_{bulk}}\right)\frac{\partial S_{bulk}}{\partial t} \tag{5.24}$$

We have tested Eqs.(5.22-5.24) from the PNM data. Eqs.(5.22) and (5.23) together with Eq.(5.24) were solved using a first order finite difference scheme

to express the derivatives with respect to time, i.e. expressions of the form $\frac{\partial S_{2bulk}}{\partial t} = \frac{S_{2bulk}(t+\delta t)-S_{2bulk}(t)}{\partial t}$. The method was explicit, i.e. the values of the saturations involved in the expression of the source term $\dot{m}_{12}$ were taken at the previous time step. The saturation S_{bulk} was obtained from $S_{bulk} = S_{1bulk} + S_{2bulk}$. Since the initial period affected by the finite size effect is not considered, the simulations started with the following initial conditions imported from the PNM simulations: S_{bulk}= 0.6833, S_{1bulk}= 0.678, S_{2bulk}= 0.00511. Since the focus is on the evolution of the percolating and non-percolating phases, the evaporation rate was considered as an input data. Thus, the evaporation flux j computed from the PNM simulations was used. This led to the results depicted in Figure.5.7, which were obtained with η =0.1 and S_{irr} =0.3138 . As can be seen, the three equation continuum model leads to a quite reasonable agreement with the PNM data. This is an interesting confirmation in the context of drying of the approach proposed in [8].

5.6 Solute concentration evolution in the hyperdiffusive limit

As pointed out in [4] or in [25], the evolution of the concentration of a solute in a drying porous medium generally results from two main effects: i) the solute convective transport in the percolating liquid phase which leads to the accumulation of solute in the porous medium top surface region (for the configuration depicted in Figure.5.1), ii) the fact that the volume occupied by the liquid phase shrinks during drying whereas the total amount of solute in this volume does not change (precipitation or wall deposit phenomena being assumed negligible). It was shown in [4] that the commonly used continuum model of solute transport [26, 28] did not lead to a good agreement with PNM simulations. This was attributed to the fact that the classical approach does not distinguish between the percolating liquid phase and the non-percolating liquid phase. The objective in what follows is to explore whether the three equation continuum model can help alleviating the discrepancies between the PNM simulations and the continuum approach. To this end, we focus on the second mechanism as regards the variation of the solute concentration. This mechanism is referred to as the liquid phase shrinking effect since the increase in the concentration due to this mechanism results from the decrease in the volume occupied by the liquid phase in the porous medium. We only consider the limiting situation where convective effect on the solute transport can be neglected, i.e. the very low Peclet number case [26]. This corresponds for

instance to a very low evaporation rate. This limiting situation is referred to as the hyperdiffusive limit since the solute concentration is consistently assumed to be spatially uniform in each liquid cluster. The solution is dilute so that impact of the solute on the surface tension, the liquid density or the equilibrium vapour pressure at the menisci can be neglected.

5.6.1 PNM computations

Initially, the concentration is uniform in the liquid phase and denoted by C_0. Then the concentration is updated in each cluster according to the mass conservation equation,

$$C_i(t+\delta t)V_i(t+\delta t) = C_i(t)V_i(t) \tag{5.25}$$

where C_i is the concentration in cluster #i and V_i is the volume of liquid cluster #i. The time step δt in Eq.(5.25) is the time step of the PNM drying algorithm. Eq.(5.25) is for a shrinking cluster. A cluster can also split into two smaller clusters as the result of the invasion of a pore by the gas phase. In this case, the concentration C_{i1}=C_{i2}=$C_{i1/i2}$ in the newly formed cluster i_1 and i_2 is computed from the equation,

$$C_{i_1/i_2}(t+\delta t)(V_{i_1}(t+\delta t) + V_{i_2}(t+\delta t)) = C_i(t)V_i(t) \tag{5.26}$$

Where V_{i1},V_{i2} and V_i are the volumes of cluster # i_1, # i_2 and #i respectively. Then the slice averaged concentrations are computed by volume averaging the concentration in each slice,

$$C_{sl}(t,z) = \frac{\sum_{i=1}^{n} C_i(t).V_{isl}(t)}{\sum_{i=1}^{n} V_{isl}(t)} = \frac{\sum_{i=1}^{n} C_i(t).V_{isl}(t)}{\epsilon.S_{sl}.A.h} \tag{5.27}$$

$$C_{2sl}(t,z) = \frac{\sum_{i=2}^{n} C_{2i}(t).V_{isl}(t)}{\sum_{i=2}^{n} V_{isl}(t)} = \frac{\sum_{i=2}^{n} C_{2i}(t).V_{isl}(t)}{\epsilon.S_{2sl}.A.h} \tag{5.28}$$

where V_{isl} is the volume of cluster #i present in the considered slice, h= 10.a is the slice thickness.
It is recalled that label #1 is for the percolating cluster. The concentration in the later is spatially uniform over the whole network. Since C_1 is uniform of the network, it is obvious the slice averaged concentration C_{1sl} is spatially uniform and equal to C_{1net}.
The evolution of the three slice average concentration profiles, namely C_{sl}, C_{1sl} and C_{2sl}, during the CRP is depicted in Figure.5.9. As expected the concentration increases during the CRP because of the liquid cluster dynamics, i.e. the fact that clusters split and shrink. However, it can be noticed

that the fragmentation process occurs essentially in the main cluster, i.e. the cluster forming the percolating liquid phase, when only the bulk region is considered since the evaporation rate of the isolated clusters located within the bulk region is quite small (Figure.5.8).

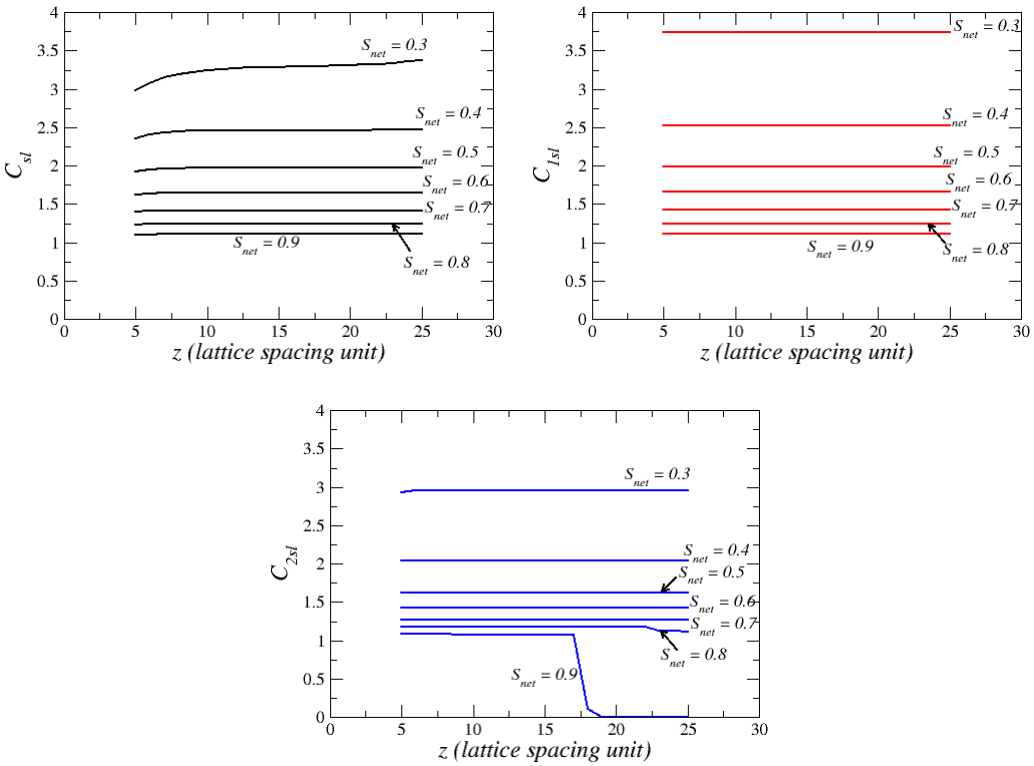

Figure 5.9: Profiles of C_{sl}, C_{1sl} and C_{2sl} in the network corresponding to S_{net} =0.9, 0.8, 0.7, 0.6, 0.5, 0.4, 0.3; z = 0 corresponds to the network top surface (Figure.5.2) whereas z = 30 to the network bottom limiting surface.

Interestingly, the concentration profiles are flat. This was of course expected for C_{1sl} since the concentration is uniform in the percolating liquid phase but somewhat less obvious as regards the non-percolating liquid phase slice averaged concentration, i.e. C_{2sl}.
This point is discussed further below and explained in the discussion section (section 5.7).
Also, the results shown in Figure.5.9 indicate that the concentration is greater in the percolating liquid phase than in the non-percolating liquid phase and thus greater than the average concentration in the liquid phase. This is better illustrated in Figure.5.10 showing the variations of C_{bulk} , C_{1bulk} and C_{2bulk} . As for the saturations S_{bulk}, S_{1bulk} and S_{2bulk}, C_{bulk} , C_{1bulk} and C_{2bulk} are the

averaged concentrations over the slice located at z = 16. C_{bulk} is computed as,

$$C_{bulk}(t) = \frac{\sum_{i=1}^{n} C_i(t).V_{isl}(t)}{\sum_{i=1}^{n} V_{isl}(t)} \tag{5.29}$$

Where i = 1 is for the percolating cluster and n is the number of liquid clusters present in the considered slice. Similarly, the average solution concentration in the non-percolating clusters is computed as

$$C_{2bulk}(t) = \frac{\sum_{i=2}^{n} C_i(t).V_{isl}(t)}{\sum_{i=2}^{n} V_{isl}(t)} \tag{5.30}$$

Note again that the concentration is uniform over the percolating cluster and therefore the slice concentration C_{1bulk} is equal to the concentration over the whole percolation cluster.

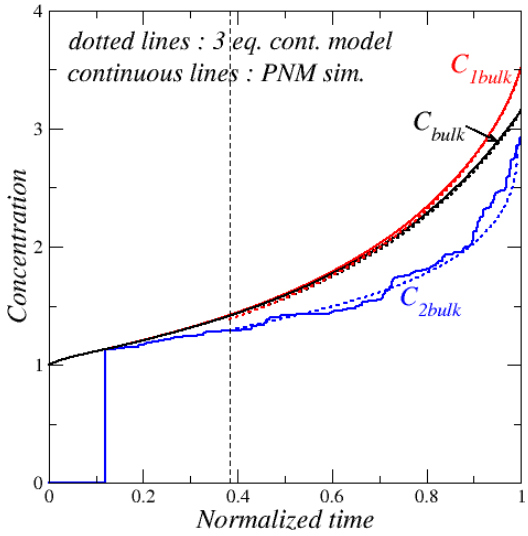

Figure 5.10: Variation of C_{bulk} ,C_{1bulk} and C_{2bulk} in the network as a function of time during the CRP. The reference time is the time at the end of the CRP defined as the time when S_{net} =0.31 The vertical dashed line indicates the beginning of the period of interest for the comparison with the three equation continuum model (see text)

Figure.5.10 clearly illustrates why it is important to distinguish the percolating and non-percolating liquid phases. Not making this distinction, as in the commonly used approach, i.e. [26, 28], leads to underestimate the concentration and thus for instance to overestimate the time corresponding to the onset of crystallization when C corresponds to a dissolved salt concentration [29]. Then the question arises as to whether the evolution depicted

in Figure.5.10 can be captured by an extended version of the three equation continuum model considering also the presence of the solute. This is studied in the section that follows.

5.6.2 Continuum approaches

Within the framework of the three equation continuum model, the solute transport equation in the percolating liquid phase is expressed as

$$\epsilon \frac{\partial S_1 C_1}{\partial t} = \nabla.(\epsilon S_1 D^*_{S_1} \nabla C_1) - \dot{m_{12S}} \tag{5.31}$$

Where $\dot{m_{12S}}$ (kg/m^3/s) is the solute mass exchange term between the percolating liquid phase and the non-percolating liquid phase. Eq.(5.31) is similar to the solute transport equation in the classical approach [26, 28]. The difference lies in the fact that the considered liquid phase is the percolating liquid phase and not the whole liquid phase. For the non-percolating liquid phase, the solute conservation equation is simply expressed as

$$\epsilon \frac{\partial S_2 C_2}{\partial t} = \dot{m_{12S}} \tag{5.32}$$

since the convective transport is assumed negligible in the isolated clusters. Integrating Eqs. (5.31) and (5.32) over the porous medium height leads to.

$$\epsilon.\ell_z.\frac{\partial S_1 C_1}{\partial t} = -\int_0^{\ell_z} \dot{m_{12S}}\ dz. \tag{5.33}$$

$$\epsilon.\ell_z.\frac{\partial S_2 C_2}{\partial t} = \int_0^{\ell_z} \dot{m_{12S}}\ dz \tag{5.34}$$

Since the profiles are approximately spatially uniform in the bulk (Figures.5.5 and 5.11), Eqs. (5.33) and (5.34) can be expressed as

$$\epsilon.\frac{\partial S_{1bulk} C_{1bulk}}{\partial t} = -\dot{m_{12S}} \tag{5.35}$$

$$\epsilon.\frac{\partial S_{2bulk} C_{2bulk}}{\partial t} = \dot{m_{12S}}. \tag{5.36}$$

The exchange term $\dot{m_{12S}}$ in Eqs.(5.35-5.36) is modelled using an expression similar to the one for $\dot{m_{12}}$ since the solute mass transfer between the percolating liquid phase and the non-percolating liquid phase is due to clusters separating from the main cluster. Furthermore, since the solute concentration in the main cluster is C_1 it is reasonable to consider that $\dot{m_{12S}}$ should be proportional to C_1 . This finally leads to express as,

$$-\dot{m_{12S}} = \eta.\epsilon.C_{1bulk}\left(\frac{S_{2bulk}-S_{irr}}{S_{irr}-S_{bulk}}\right)\frac{\partial S_{bulk}}{\partial t} \tag{5.37}$$

Eqs. (5.35) and (5.36) combined with Eq.(5.37) were solved using a method similar to the one used for solving Eqs.(5.22) and (5.23) with, as for the saturation problem, η =0.1 and S_{irr} = 0.3138. A first order finite difference scheme to express the derivatives with respect to time was used, i.e. expressions of the form $\frac{\partial S_{1bulk}C_{1bulk}}{\partial t} = \frac{(S_{1bulk}C_{1bulk})(t+\delta t)-(S_{1bulk}C_{1bulk})(t)}{\partial t}$. The method was explicit, i.e. the values of the saturations and the value of C_{1bulk} involved in the expression of the source term $\dot{m_{12S}}$ were taken at the previous time step. Then $S_{bulk}C_{bulk}$ was obtained from. $S_{bulk}.C_{bulk} = S_{1bulk}.C_{1bulk} + S_{2bulk}.C_{2bulk}$.

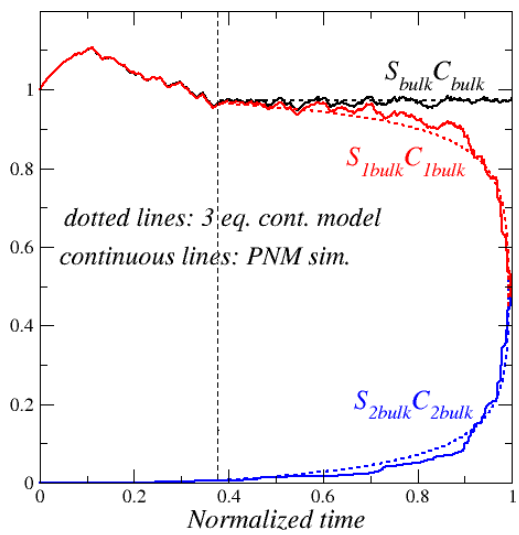

Figure 5.11: Variation of $S_{bulk}.C_{bulk}$, $S_{1bulk}.C_{1bulk}$ and $S_{2bulk}.C_{2bulk}$ in the network as a function of time during the CRP. The reference time is the time at the end of the CRP defined as the time when S_{net} =0.31 The vertical dashed line corresponds to the time when S_{net} = 0.7 (as explained in the text, only the times greater than the time corresponding to S_{net} = 0.7 are considered for the comparison between the continuum model and the PNM data).

This led to the results depicted in Figure.5.11. As can be seen, the three equation continuum model leads here again to a quite reasonably good agreement with the PNM data. As explained before, only the range of saturations not significantly affected by the initial finite size effect is considered for the comparison between the continuum model and the PNM data. This corresponds to the overall network saturations lower than approximately S_{net}

=0.7. The time corresponding to S_{net} =0.7 is indicated by a vertical dashed line in Figure.5.11. As expected the product $S_{bulk}.C_{bulk}$ is constant over the period of interest. This simply means that the total mass of solute in the bulk region is conserved. The total mass of solute in the percolating phase, i.e. $S_{1bulk}.C_{1bulk}$, decreases. This is because the percolating liquid phase loses mass as the result of the fragmentation process. The corresponding mass loss corresponds to the mass of solute gained by the non-percolating liquid phase, which therefore increases during the CRP. The latter corresponds to $S_{2bulk}.C_{2bulk}$ in Figure.5.11. From the computation of $S_{bulk}.C_{bulk}$, $S_{1bulk}.C_{1bulk}$ and $S_{2bulk}.C_{2bulk}$ depicted in Figure.5.11 and the computation of S_{1bulk} ,S_{1bulk} and S_{2bulk} depicted in Figure.5.7, the solute concentrations C_{bulk}, C_{1bulk} and C_{2bulk} were obtained as $C_{bulk} = \frac{S_{bulk}C_{bulk}}{S_{bulk}}$, $C_{1bulk} = \frac{S_{1bulk}C_{1bulk}}{S_{1bulk}}$, and $C_{2bulk} = \frac{S_{2bulk}C_{2bulk}}{S_{2bulk}}$. The corresponding results are compared to the PNM simulation data in Figure.5.10. As can be seen, the 3 equation continuum model predicts quite well the variations of the three considered solute concentrations. In particular, the important fact that the solute concentration is greater in the percolating liquid phase is well captured.

5.7 Discussions

The classical one equation continuum model [26, 28] predicts that the solute concentration is uniform over the liquid phase in the considered very low Peclet number limit during the CRP. This solute concentration is simply given by

$$C(t) = \frac{S_{net0}.C_0}{S_{net}(t)} \tag{5.38}$$

Where S_{net0} and C_0 are the initial saturation and solute concentration in the network respectively. C(t) corresponds to C_{bulk} in the results presented in the previous section.

The results presented in the previous section clearly show that the solute concentration predicted by this quite classical model in the very low Peclet number limit should not be understood as the solute concentration all over the liquid.

The liquid phase is actually fragmented and the solute concentration can vary from one liquid cluster to another. As a result, the solute concentration computed with the classical model must be interpreted as an average concentration over the various liquid clusters, more exactly as a weighted average concentration where the weights are the cluster volume fractions, i.e.

$$< C >= \frac{\sum_{i=1}^{i=n} V_i.C_i}{\sum_{i=1}^{i=n} V_i} = \sum_{i=1}^{i=n} \left(\frac{V_i}{\sum_{i=1}^{i=n} V_i} \right) C_i \tag{5.39}$$

where V_i is the volume of liquid cluster #i and C_i is the solute concentration in cluster #i, n is the number of liquid clusters at the considered time.
In other words, although diffusion is the dominant transport mechanism in the very low Peclet number limit, this does not mean that the solute concentration is spatially uniform in the liquid phase. To illustrate further this feature, the standard deviation of the solute concentration over the various clusters can be computed from the PNM results.
Since the percolating and the non − percolating liquid phases are distinguished with the three equation continuum model, the spatial variability of the solute concentration is illustrated considering the non-percolating liquid phase. The average solute concentration in the non-percolating liquid phase is computed as

$$< C >_2= \frac{\sum_{i=2}^{i=n} V_i.C_i}{\sum_{i=2}^{i=n} V_i} = \sum_{i=2}^{i=n} \left(\frac{V_i}{\sum_{i=2}^{i=n} V_i} \right) C_i \tag{5.40}$$

Noting that i =1 corresponds to the main cluster. Thus i in the range [2, n] corresponds to the isolated clusters (n-1 is thus the total number of isolated clusters). The standard deviation of the solute concentration over the non-percolating liquid phase is then computed as,

$$\sigma_{C_2} = \sqrt{\frac{\sum_{i=2}^{i=n} V_i(C_i - < C >_2)^2}{\sum_{i=2}^{i=n} V_i}} \tag{5.41}$$

The variation of σ_{C_2} over the CRP is shown in Figure.5.12.
As can be seen, the standard deviation relative to the mean increases during most of the CRP. The decrease toward the end of the CRP is due to the fact that the mean increases faster than the standard deviation because of the formation of many clusters of higher concentration toward the end of the CRP (Figure.5.4). As illustrated in the inset in Figure.5.12, the variation of the solute concentration over the non-percolating liquid phase is significant with about a factor 2 between the concentration in the clusters of lowest concentration and the clusters of highest concentrations.
The existence of the concentration spatial variability in the considered diffusion dominant regime is directly due to the fact that isolated clusters form from the main cluster all along the CRP (as illustrated in Figure.5.4).

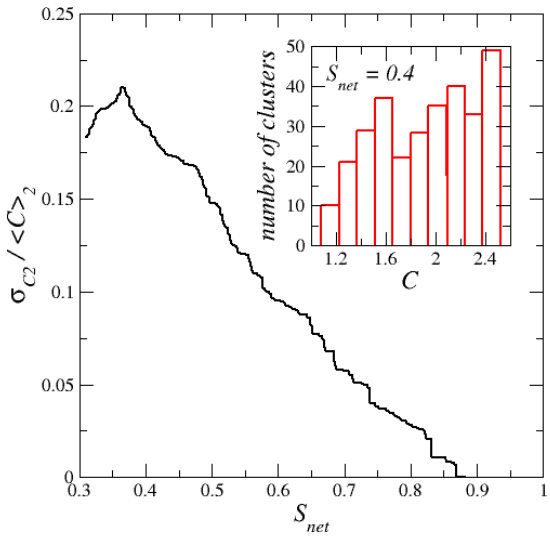

Figure 5.12: Variation of the standard deviation σ_{C_2} relative to the mean of the solute concentration distribution in the non-percolating liquid phase over the network bulk region during the CRP. The inset shows the distribution of the concentration in the isolated clusters for $S_{net} = 0.4$.

The concentration in an isolated cluster in the bulk region is the concentration in the main cluster at the time when the isolated cluster forms. Since the concentration in the main cluster increases during the CRP (Figure.5.10), the later an isolated cluster forms in the bulk region, the greater its concentration is. Based on the main cluster concentration variations depicted in Figure.5.10, it can be readily inferred that the concentration over the non-percolating phase varies at a given time in the range [C_0, C_1(t)]. However, this spatial variability due to the historicity of the isolated clusters formation from the main cluster does not imply a spatial variation along the network depth. As illustrated in Figure.5.9, the mean concentration profiles are flat. This is due to the fact that the probability of forming a new cluster from the main cluster in the bulk region does not depend of the position [9].
The fragmentation of the liquid phase in isolated clusters also leads to a somewhat counter-intuitive result after the CRP in the RFP (Receding Front Period). As described in [3], the percolating liquid phase disappears at the end of the CRP in the considered "asymptotic" regime purely controlled by capillary effects. This regime is described as asymptotic because it is rarely observed in the standard laboratory experiments due to the viscous effects. In most experiments, the liquid phase is actually percolating up to the receding front forming the lower edge of the dry region developing in the network

during the RFP. By contrast, in the considered asymptotic regime, the liquid phase is formed by isolated clusters only and the development of the dry zone results from the gradual evaporation of the isolated clusters [3]. This asymptotic regime is expected when evaporation is quite low and/or with sufficiently thin systems. In the considered very low Peclet number limit, the concentration profiles could be expected to be flat due to the dominant diffusion transport in the liquid phase. However, since the isolated clusters evaporation dynamics is not spatially uniform during the RFP, the concentration profiles are actually not flat. This is illustrated in Figure.5.13.

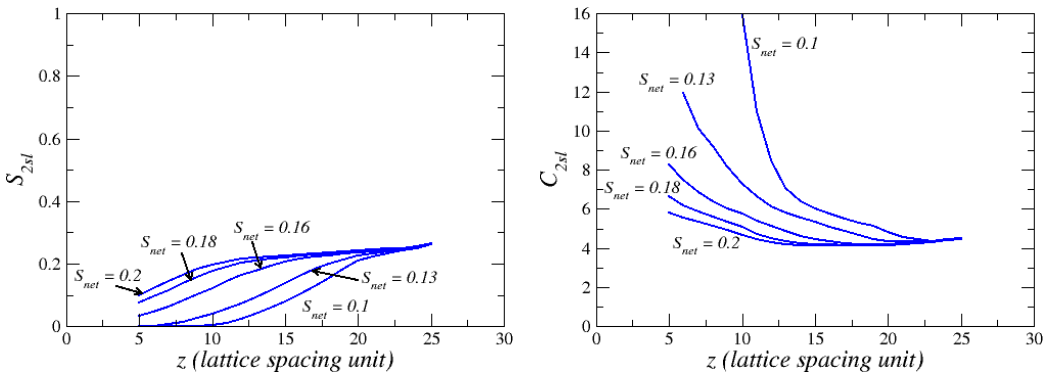

Figure 5.13: Evolution of saturation and concentration profiles after the CRP; z = 0 corresponds to the network top surface (Figure.5.2) whereas z = 30 to the network bottom limiting surface .

The evaporation rate at the boundary of the isolated clusters is significantly greater for the clusters in contact with the dry zone. In other words, the cluster evaporation rate rapidly decreases with the increasing depth in the network. Since the concentration increase is due to the clusters shrinking, the concentration increases faster in the region where the cluster evaporation rate is greater. This leads to the remarkably non-linear concentration variations depicted in Figure.5.13. Interestingly, the concentration profiles roughly tend to resemble the exponential like profiles typically resulting from the competition between advection and diffusion effects [26]. The mechanism leading to the strongly non-linear shape is of course completely different here and is due to the combination of the fragmentation of the liquid phase in isolated clusters and the screening of the evaporation at the boundary of the clusters located deeper in the network. One can refer to [30] for more details on the screening phenomenon. The screening phenomenon during the CRP is illustrated in Figure.5.8. A similar rapid decrease in the evaporation flux with the distance from the interface between the dry zone and the shrinking

liquid cluster zone exists during the RFP. Since it has been shown that the liquid films can have a strong impact in drying [18, 19, 31, 32], it must be clear that the results presented in this article as regards the solute distribution are for the situations where the impact of the films on the solute distribution is negligible. For instance, it has been shown [33] that the contact angle for an aqueous solution in the presence of a dissolved salt can be relatively high, on the order of 40° or more. With such values of the contact angle, the development of corner films is significantly hampered. By contrast, for significantly lower contact angles, when the liquid films can develop so as to maintain a hydraulic connection between the "isolated" clusters, some solute transport can occur through the films. This should reduce the concentration variation between clusters. In the case of a sufficiently low evaporation rate for the solute distribution to reach a quasi-steady state during drying, solute diffusion in the films might even lead to a uniform concentration distribution all over the liquid phase. As for the drying process in general, the consideration of liquid films within the framework of the three equation continuum model would deserve to be studied. Although the whole set of equations of the three equation continuum model was presented, only a rather simple situation, allowing solving the model quite easily without resorting to the determination of the various transport parameters of the model, was considered. In this respect, it would be interesting to extend the present work by developing a numerical procedure allowing solving the full set of equations. This would notably permit to simulate the full drying process and not only the CRP and to consider other regimes than the capillary regime and the very low Peclet number regime. Also, the edge regions, especially the top edge region in the considered drying configuration, were not studied on the ground that this is the bulk region which is of primary interest for the evaluating the continuum models. However, the top region can be of special interest for predicting or analyzing certain phenomena, such as the formation of salt efflorescence at the evaporative surface of porous media for instance, e.g. [20, 25, 29, 34, 35]. Thus, some works should be dedicated to the modelling of the transfers in the top edge region in the future.

5.8 Conclusions

A continuum model of drying in capillary porous media, referred to as the three equation continuum model, has been presented. Contrary to the commonly used continuum models of drying, the present model makes an explicit distinction between the percolating and non-percolating liquid phases. From the consideration of the frequently encountered capillary regime, it has been

shown that the model was able to predict the variations of the saturation in both the percolating and non-percolating liquid phases during the constant rate period (CRP). Then, the model was extended so as to predict the evolution of the concentration of a solute in both the percolating and non-percolating liquid phases. Comparisons with data obtained from pore network simulations were quite satisfactory. In particular, the continuum model consistently predicts that the solute concentration is higher in the percolating phase than in the non-percolating phase. However, only the very low Peclet number regime was considered. Nevertheless, the results presented in this article also clarify the meaning of the solute concentration predicted by the continuum models, which should be considered as an average concentration over the fragmented liquid phase. Counter-intuitively, it has been shown that the concentration is not necessarily uniform over the liquid phase in the considered very low Peclet number regime. As the result of the liquid fragmentation in numerous clusters, spatial fluctuations of the concentration are expected even in the very low Peclet number limit. In summary, the three equation continuum model allows significantly more accurate predictions of the solute distribution during drying. In the more general context of the macroscopic theory of biphasic flow in porous media, the present paper presents both an extension to drying, with and without the presence of a solute, of the model proposed in [5, 8] and an additional validation of this model, in particular as regards the formulation of the mass exchange term between the percolating and non-percolating liquid phases.

References

[1] L.Pel, K.A. Landman and E.F. Kaasschierter, Analytic solution for the non-linear drying problem, Int. J. of Heat and Mass Tr. 45 (15), 3173 (2002).

[2] Attari Moghaddam, A.; Prat, M.; Tsotsas, E.; Kharaghani, A. Evaporation in capillary porous media at the perfect piston-like invasion limit: Evidence of nonlocal equilibrium effects. Water Resour. Res., 2017, 53 (12), 10433-10449.

[3] Le Bray, Y.; Prat, M. Three-dimensional pore network simulation of drying in capillary porous media. Int. J. Heat Mass Transf., 1999, 42 (22), 4207-4224.

[4] F Ahmad, A Rahimi, E Tsotsas, M Prat, A Kharaghani, From micro-scale to macro-scale modeling of solute transport in drying capillary porous media, International Journal of Heat and Mass Transfer 165, 120722 (2021)

[5] R. Hilfer, Capillary pressure, hysteresis and residual saturation in porous media, Physica A 359, 119-128 (2006)

[6] R. Hilfer, Macroscopic capillarity without a constitutive capillary pressure function, Physica A 371, 209-225 (2006).

[7] R. Hilfer, Macroscopic capillarity and hysteresis for flow in porous media, Phys. Rev. E 73, 016307 (2006).

[8] F. Doster, P. A. Zegeling, and R. Hilfer, Numerical solutions of a generalized theory for macroscopic capillarity, Phys. Rev. E 81, 036307 (2010)

[9] Attari Moghaddam, A.; Kharaghani, A.; Tsotsas, E.; Prat, M. Kinematics in a slowly drying porous medium: Reconciliation of pore network simulations and continuum modeling. Phys. Fluids, 2017, 29 (2), 022102.

[10] F Ahmad, M Talbi, M Prat, E Tsotsas, A Kharaghani, Non-local equilibrium continuum modeling of partially saturated drying porous media: Comparison with pore network simulations, Chemical Engineering Science, 228, 115957 (2020)

[11] van Brakel, J. (1980). Mass transfer in convective drying. In Mujumdar, A. S. (ed.), Advances in Drying, pp. 217–267. Hemisphere, New York.

[12] Attari Moghaddam, A.; Kharaghani, A.; Tsotsas, E.; Prat, M. A pore network study of evaporation from the surface of a drying non-hygroscopic porous medium. AIChE J., 2018, 64 (4), 1435-1447.

[13] M.Talbi, M.Prat About Schlünder's model: A numerical study of evaporation from partially wet surfaces, Drying Technology, 37 (5), 513-524 (2019) (Chapter 3 of the present thesis)

[14] M.Prat. Percolation model of drying under isothermal conditions in porous media. Int. J. of Multiphase Flow. Vol.19,No.4, pp.691-704 (1993)

[15] Prat, M. Recent advances in pore-scale models for drying of porous media. Chem. Eng. J., 2002, 86 (1-2), 153-164,

[16] M.Prat, Pore network models of drying, contact angle and films flows, Chem. Eng. Technol., 34, No. 7, 1029–1038 (2011)

[17] Metzger, T.; Tsotsas, E.; Prat, M. Pore-network models: A powerful tool to study drying at the pore level and understand the influence of structure on drying kinetics. Modern drying technology: Computational tools at different scales, 2007, 1, 57-102.

[18] Prat, M. On the influence of pore shape, contact angle and film flows on drying of capillary porous media, Int. J. Heat Mass Transf., 2007, 50, 1455-1468,

[19] Chauvet, F.; Duru, P.; Geoffroy, S.; Prat, M. Three periods of drying of a single square capillary tube, Phys. Rev. Lett., 2009, 103, 124502.

[20] Gupta, S.; Huinink, H. P.; Prat, M.; Pel, L.; Kopinga, K. Paradoxical drying due to salt crystallization, Chem. Eng. Sci., 2014, 109, 204-211.

[21] Thiery, J.; Rodts, S.; Weitz, D. A.; Coussot, P. Drying regimes in homogeneous porous media from macro-to nanoscale. Phys. Rev. Fluids, 2017, 2, 074201.

[22] Chapter 4 of the present thesis .

[23] D Stauffer, and A. Aharony, Introduction to Percolation Theory, Taylor & Francis, London, (1992).

[24] Lu, X.; Kharaghani, A.; Tsotsas, E. Transport parameters of macroscopic continuum model determined from discrete pore network simulations of drying porous media. Chem. Eng. Sci., 2020, 223, 115723.Autres ref Magdeburg

[25] Diouf, B.; Geoffroy, S.; Chakra, A. A.; Prat, M. Locus of first crystals on the evaporative surface of a vertically textured porous medium. EPJ Appl. Phys., 2018, 81 (1), 1-14.

[26] Huinink, H. P.; Pel, L.; Michels, M. A. J. How ions distribute in a drying porous medium: A simple model. Phys. Fluids, 2002, 14 (4), 1389-1395.

[27] Guglielmini, L.; Gontcharov, A.; Aldykiewicz, A. J.; Stone, H. A. Drying of salt solutions in porous materials: Intermediate-time dynamics and efflorescence. Phys. Fluids, 2008, 20 (7), 1-7.

[28] Sghaier, N.; Prat, M.; Ben Nasrallah, S. On ions transport during drying in a porous medium. Transp. Porous Media, 2007, 67 (2), 243-274.

[29] Hidri, F.; Sghaier, N.; Eloukabi, H.; Prat, M.; Nasrallah, S. Ben. Porous medium coffee ring effect and other factors affecting the first crystallisation time of sodium chloride at the surface of a drying porous medium. Phys. Fluids, 2013, 25, 127101 (12).

[30] M.Prat. Isothermal drying of non-hygroscopic capillary-porous materials as an invasion percolation process. Int.J. of Multiphase Flow.Vol.21,No.5, pp.875-892 (1995)

[31] Yiotis, A. G., Boudouvis, A. G., Stubos, A. K., Tsimpanogiannis, I. N., & Yortsos, Y. C.. Effect of liquid films on the drying of porous media. AIChE Journal, 50, 2721–2731 (2004)

[32] A.G. Yiotis, D.Salin, E.S.Tajerand and Y.C. Yortsos, Drying in porous media with gravity-stabilized fronts: Experimental results, Physical Review E 86, 026310 (2012)

[33] Sghaier, N.; Prat, M.; Nasrallah, S. B. On the influence of sodium chloride concentration on equilibrium contact angle, Chem.Eng. J., 2006, 122, 47-53.

[34] Eloukabi, H.; Sghaier, N.; Nasrallah, S. B.; Prat, M. Experimental study of the effect of sodium chloride on drying of porous media: The crusty-patchy efflorescence transition, Int. J. Heat Mass Transf., 2013, 56, 80-93.

[35] Desarnaud, J., Derluyn, H., Molari, L., de Miranda,S. Cnudde, V., Shahidzadeh, N. Drying of salt contaminated porous media: Effect of primary and secondary nucleation, Journal of Applied Physics 118 (11) 114901 (2015)

Chapter 6

General Conclusion

Drying in porous media is a physical phenomenon involving transfer between a porous medium and the external environment. In this study, a numerical version of the drying process was studied: the PNM drying. PNMs are based on a simplified representation of the pore space, allowing using simplified solutions to the transport between pores. In this work we have performed drying PNM simulations in the case of the (quasi-)isothermal capillary regime and studied the continuum modelling of the PNM drying. A first issue in the PNM approach lies in the modelling of the transfer at the network surface open to external gas. A somewhat classical approach consists in setting computational nodes in the external boundary layer. An alternative would be to parametrize the evaporation flux (or the vapor flux if the pore is dried) from every surface pore. Such a type of parametrization was proposed by Schlünder but for the very simplified situation of a spatially periodic surface where all the pores have the same size and are filled with liquid. This allowed him to proposed an analytical formula linking the thickness of the boundary layer, the evaporation rate from each individual surface pore and the wetted fraction of the porous surface. The validity of Schlünder's formula was studied from comparisons with numerical simulations. It was shown that the results were dependent on the pore shape whereas a poor agreement was observed with numerical simulations in the case of very small wet surface fraction. Then it was shown that the direct application of Schlünder's formula leads to poor results when the pore size varies over the surface because the influence of neighbouring pores is not adequately taken into account. This led to introduce the concept of influence surface area. This greatly improves the comparison between Schünder's formula (modified so as to taken into account the influence surfaces) and the numerical simulations. It should be noted that only the case where all the surface pores are filled with liquid was considered in the corresponding Chapter (Chapter 3). In other words,

the vapor partial pressure was uniform and equal to the saturated vapor pressure at the entrance of all the pores at the surface. However, during the drying process, the vapor partial pressure varies from one pore to another as the result of the gradual invasion of the surface pores by the gas phase. It turns out that the Schlünder's formula is not adapted to the case of the vapor partial pressure heterogeneous distribution encountered in the PNM simulations. Although attractive at first glance, Schlünder's approach was therefore abandoned in the subsequent chapters.

The numerical PNM simulations show the existence of edge effects located in the interfacial zones, interface between the PNM and the external gas or between the PNM and the wall (upper and bottom zone of the PNM in the studied configuration). Both edge effects have been characterized and show to not depend on the size of the network (Chapter 4). Furthermore, the size of the edge effect zones was found to be smaller than the expected size of a REV. It was also shown that the upper edge effect zone was the place of the evaporation and the region where the non-local equilibrium effect is noticeable. The identification and characterization of the top edge effect region led to the development of a coupling condition between the internal transfer and the external transfer based on the concept of interfacial resistance. The interfacial resistance was studied in details over stage 1 evaporation (corresponding to the classical "constant" rate period (CRP)). It was shown that both the evolution of the interfacial resistance and the external mass transfer resistance must be taken into account because of the impact of the variability of the vapor partial pressure at the surface.

Chapter 5 was devoted to the development of a new continuum model based on the observation that the gradual fragmentation of the liquid phase during drying is a key feature. This led to separate the liquid phase into the percolating liquid phase, corresponding to the main liquid cluster spanning the network, and the non-percolating liquid phase. The resulting CM model was a three equation continuum model (CM) based on three mass conservation equations for the liquid percolating phase the non-percolating liquid phase and the vapor respectively. The source/ sink term coupling the liquid percolating and liquid non-percolating mass conservation equations was based on an earlier work by Hilfer and coll. on the theory of two-phase flows in porous media. This three equation CM model led to a quite good agreement with the PNM simulations over the considered period of drying (stage 1). The interest of this new model was further illustrated with the consideration of a solute in the liquid phase (in the very low Peclet number limit). This led to a five equation CM model with the two additional solute mass transfer

conservation equations. The sink / source term between the two solute mass conservation equations was a rather simple adaptation of the sink/source term developed for the percolating and non-percolating liquid mass conservation equations. The five equation CM led again to a quite good agreement with the PNM simulations. In particular, it was shown that the solute concentration was higher in the percolating cluster, an effect which, of course, cannot be captured by the commonly used 1 equation solute transport model. Therefore, the latter overestimates the crystallization onset time for example.

Although the present work shed new lights on the "drying problem", a completely satisfactory drying theory remains an open problem. In this work, we have mainly considered stage 1 evaporation. The work must therefore be extended so as to consider the full drying process. In particular, the stage 1/stage 2 (or CRP/FRP) transition, a key issue in the drying problem, must be studied. It is unclear whether the concept of interfacial resistance is still the best choice to model this transition as well as the full drying. Also, only the capillary regime was considered. The other regimes should be studied. For instance, the impact of the gravity or viscous forces, when non-negligible compared to capillary effects, on the top edge effect and therefore the interfacial resistance must be clarified. Another key aspect lies in the impact of liquid films. Liquid films were completely ignored in the present work. Several works have highlighted the impact of liquid films, especially when the liquid is perfectly wetting or when the contact angle is sufficiently small. Thus, the consideration of liquid films is also a necessary next step. Also, it is customary to distinguish the capillary porous media from the hygroscopic porous media. In this work, only the first type of porous media, i.e. capillary, was considered. Owing to the significance of hygroscopic porous media in the applications, it would be interesting to consider hygroscopic porous media as well.

A last point concerns the approach considered in this thesis based on PNM simulations. Although we have shown that the evaluation of continuum models was possible considering small networks, it is obvious that the consideration of larger networks would facilitate the comparison and make it more straightforwardly meaningful. In this respect, high performance computations remain a desirable objective.